



**FAULT RIDE-THROUGH CAPABILITY OF MULTI-POLE PERMANENT MAGNET
SYNCHRONOUS GENERATOR FOR WIND ENERGY CONVERSION SYSTEM**

by

CLEMENT NDJEWEL KENDECK

Thesis submitted in fulfilment of the requirements for the degree

Master of Engineering: Electrical Engineering

in the Faculty of Engineering

at the Cape Peninsula University of Technology

Supervisor: Dr AK Raji

Bellville

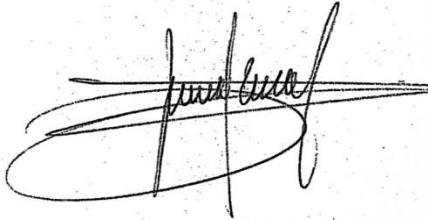
September 2019

CPUT copyright information

The dissertation/thesis may not be published either in part (in scholarly, scientific or technical journals), or as a whole (as a monograph), unless permission has been obtained from the University

DECLARATION

I, Clement Ndjewel Kendeck, declare that the contents of this dissertation/thesis represent my own unaided work, and that the dissertation/thesis has not previously been submitted for academic examination towards any qualification. Furthermore, it represents my own opinions and not necessarily those of the Cape Peninsula University of Technology.

A handwritten signature in black ink, appearing to read 'Clement Ndjewel Kendeck', written over a horizontal line.

08 September 2019

Signed

Date

ABSTRACT

Wind has become one of the renewable energy technologies with the fastest rate of growth. Consequently, global wind power generating capacity is also experiencing a tremendous increase. This tendency is expected to carry on as time goes by, with the continuously growing energy demand, the rise of fossil fuels costs combined to their scarcity, and most importantly pollution and climate change concerns. However, as the penetration level increases, instabilities in the power system are also more likely to occur, especially in the event of grid faults. It is therefore necessary that wind farms comply with grid code requirements in order to prevent power system from collapsing. One of these requirements is that wind generators should have fault ride-through (FRT) capability, that is the ability to not disconnect from the grid during a voltage dip. In other words, wind turbines must withstand grid faults up to certain levels and durations without completely cutting off their production. Moreover, a controlled amount of reactive power should be supplied to the grid in order to support voltage recovery at the connection point.

Variable speed wind turbines are more prone to achieve the FRT requirement because of the type of generators they use and their advanced power electronics controllers. In this category, the permanent magnet synchronous generator (PMSG) concept seems to be standing out because of its numerous advantages amongst which its capability to meet FRT requirements compared to other topologies. In this thesis, a 9 MW grid connected wind farm model is developed with the aim to achieve FRT according to the South African grid code specifications. The wind farm consists of six 1.5 MW direct-driven multi-pole PMSGs wind turbines connected to the grid through a fully rated, two-level back-to-back voltage source converter. The model is developed using the Simpowersystem component of MATLAB/Simulink. To reach the FRT objectives, the grid side controller is designed in such a way that the system can inject reactive current to the grid to support voltage recovery in the event of a grid low voltage. Additionally, a braking resistor circuit is designed as a protection measure for the power converter, ensuring by the way a safe continuous operation during grid disturbance.

ACKNOWLEDGEMENTS

I would like to thank my supervisor Dr AK Raji for his guidance, patience, and encouragements throughout this journey. I would not have made it this far without his endless support.

I would also like to thank the management of Cape Peninsula University of Technology for the material and financial support they have provided through University Research Funds and bursaries grants.

I would also like to express my sincere gratitude to my lovely parents, brothers and sisters for their continuous involvement in making my life a success.

To my friends and colleagues, I am also grateful for their moral support and encouragements.

Lastly but not least, I would like to thank God for giving me all the strength and resources necessary to successfully complete this degree.

DEDICATION

To my lovely parents

TABLE OF CONTENTS

DECLARATION	ii
ABSTRACT	iii
ACKNOWLEDGEMENTS	iv
DEDICATION	v
TABLE OF CONTENTS	vi
LIST OF ABBREVIATIONS	ix
LIST OF FIGURES	xi
LIST OF TABLES	xv
1 INTRODUCTION	1
1.1 Background to the research problem	1
1.2 Wind energy worldwide.....	2
1.3 Wind energy in South Africa	3
1.4 Statement of the research problem.....	4
1.5 Rationale and motivations of the research	5
1.6 Research aim and methodology	5
1.7 Delineations of the research	5
1.8 Thesis organisation.....	6
2 WIND TURBINE CONFIGURATIONS	7
2.1 Components of wind turbines	7
2.2 Wind turbine aerodynamics and characteristics	9
2.2.1 Power in the wind	9
2.2.2 Turbine power.....	9
2.2.3 Power coefficient and tip speed ratio	10
2.2.4 Power curve.....	10
2.3 Wind turbine aerodynamic controls.....	12
2.3.1 Passive stall.....	12
2.3.2 Active stall	12
2.3.3 Pitch control.....	13
2.4 Wind turbine topologies	13

2.4.1	Wind turbines' rotor configurations.....	13
2.4.2	Wind turbines' generators	14
2.4.3	Wind turbines rotational speed configurations.....	15
2.5	PMSG in variable speed wind turbines	19
2.5.1	Classification of PMSGs according to their flux orientation	20
2.5.2	Classification of PMSGs according to the magnet mounting.....	20
2.5.3	Classification of PMSGs according to the rotor position.....	23
2.5.4	Maximum power point tracking	23
2.6	Power converters topologies for PMSG wind turbines	26
2.6.1	Thyristor grid-side inverter	26
2.6.2	Hard-switched grid-side inverter	27
2.6.3	Multilevel converters.....	27
2.6.4	Matrix converters	28
2.6.5	Z-source converters.....	29
2.7	Power converter control.....	28
2.8	Summary of the chapter:.....	30
3	GRID CODE REQUIREMENTS AND LVRT SOLUTIONS.....	31
3.1	Grid code requirements for wind farms	31
3.1.1	Frequency and voltage operating range.....	33
3.1.2	Active power control	34
3.1.3	Reactive power and voltage control	35
3.1.4	Low Voltage Ride Through capability.....	35
3.1.5	South African grid code requirements for Renewable Power Plants	39
3.2	LVRT methods for PMSG WTs.....	40
3.2.1	Modified control-based techniques	40
3.2.2	Additional devices-based techniques.....	42
4	WIND TURBINE SYSTEM MODELING	46
4.1	Wind turbine model.....	46
4.2	Drive train model	47
4.3	Modelling of the PMSG.....	48

4.3.1	Reference frame theory	51
4.3.2	Dynamic model.....	52
4.3.3	Steady state model.....	53
4.3.4	Equivalent circuit of the PMSG	53
4.4	Modelling of the back-to-back voltage source converter	54
4.4.1	Generator side converter control.....	57
4.4.2	Grid side converter control.....	57
4.4.3	Space vector modulation (SVM)	62
5	SIMULATION RESULTS AND DISCUSSIONS.....	69
5.1	Power system configuration.....	69
5.2	Wind farm model aggregation.....	70
5.3	Simulation results under normal operating conditions	70
5.4	Simulation results under faulty conditions	77
5.4.1	Fault compensation	77
5.4.2	Case studies for simulations under grid faults.....	81
6	CONCLUSIONS AND RECOMMENDATIONS	103
	REFERENCES	105
	APPENDICES	111
6.1	Appendix A: System parameters.....	111
6.2	Appendix B: System simulation model.....	112

LIST OF ABBREVIATIONS

AC	Alternating Current
AFPM	Axial Flux Permanent Magnet
BPA	Blade Pitch Angle
CHB	Cascaded H-Bridge
DC	Direct Current
DFIG	Doubly Fed Induction Generator
DPC	Direct Power Control
DTC	Direct Torque Control
DVR	Dynamic Voltage Restorer
EESG	Electrically Excited Synchronous Generator
ESS	Energy Storage System
FACTS	Flexible AC Transmission System
FC	Flying Capacitor
FOC	Field Oriented Control
FRT	Fault Ride-Through
GSC	Grid Side Converter
GWEC	Global Wind Energy Council
HAWT	Horizontal Axis Wind Turbine
HCC	Hysteresis Current Control
IEA	International Energy Agency
IEEE	Institute of Electrical and Electronics Engineers
IGBT	Insulated Gate Bipolar Transistor
IRP	Integrated Resource Plan
IT	Information Technology
LAB	Lead Acid Battery
LVRT	Low Voltage Ride-Through
MC	Matrix Converter
MERS	Magnetic Energy Recovery Switch
MPP	Maximum Power Point
MPPT	Maximum Power Point Tracking
MSC	Machine Side Converter
NERSA	National Energy Regulator of South Africa
NPC	Neutral Point Clamping
OPC	Optimum Power Control
OTC	Optimum Torque Control
PCC	Point of Common Coupling

PEC	Power Electronics Converter
PI	Proportional Integral
PLL	Phase Locked Loop
PM	Permanent Magnet
PMSG	Permanent Magnet Synchronous Generator
PMSM	Permanent Magnet Synchronous Machine
POC	Point of Connection
PWM	Pulse Width Modulation
RFPM	Radial Flux Permanent Magnet
RPP	Renewable Power Plant
RSA	Republic of South Africa
SA	South Africa
SCIG	Squirrel Cage Induction Generator
SCR	Silicon Controlled Rectifier
SSB	Sodium Sulfur Battery
SSSC	Static Synchronous Series Compensator
STATCOM	Static Compensator
SVC	Static Var Compensator
SVM	Space Vector Modulation
SVPWM	Space Vector Pulse Width Modulation
TCSC	Thyristor Controlled Series Capacitor
TFFPM	Transversal Flux Permanent Magnet
THD	Total Harmonic Distortion
THM	Top Head Mass
TSR	Tip Speed Ratio
UPFC	Unity Power Factor Control
UK	United Kingdom
US	United States
VAWT	Vertical Axis Wind Turbine
VOC	Voltage Oriented Control
VSC	Voltage Source Converter
VSI	Voltage Source Inverter
WECS	Wind Energy Conversion System
WPP	Wind Power Plant
WRIG	Wound Rotor Induction Generator
WT	Wind turbine
WTS	Wind turbine System

LIST OF FIGURES

Figure 1.1: Global annual installed wind capacity (GWEC, 2015)	2
Figure 1.2: Global cumulative installed wind capacity (GWEC, 2015)	3
Figure 1.3: Historic Eskom electricity price increases (Writer, 2015)	4
Figure 2.1: Components of a wind turbine system	7
Figure 2.2: Power curve for a wind turbine	11
Figure 2.3: Power curve for a passive stall-controlled wind turbine	11
Figure 2.4: Power curve for an active stall and pitch-controlled wind turbine.....	12
Figure 2.5: Wind turbine rotor configurations	14
Figure 2.6: Classification of different wind turbine generators	15
Figure 2.7: Classification of different wind turbine concepts	16
Figure 2.8: Fixed speed concept.....	17
Figure 2.9: Limited variable speed concept.....	17
Figure 2.10: Variable speed concept with partial scale converter	17
Figure 2.11: Variable speed with full scale converter	18
Figure 2.12: Variable speed with direct grid connection	18
Figure 2.13: Cross sectional view in axial direction of axial flux (left) and radial flux (right) PMSG	22
Figure 2.14: Surface mounted (left) and inset (right) magnet rotors for PMSG	22
Figure 2.15: Inner (left) and outer (right) rotor PMSG	22
Figure 2.16: Typical MPPT curve for a power versus rotational speed turbine characteristics	23
Figure 2.17: PSF method applied to a PMSG based WECS	24
Figure 2.18: Optimal TSR method applied to a PMSG based WECS	24
Figure 2.19: OTC method applied to a PMSG based WECS.....	25
Figure 2.20: P & O method applied to a PMSG based WECS.....	25
Figure 2.21: Examples of PECs used with PMSG based WECS.....	28
Figure 3.1: Voltage and frequency operating ranges as defined by German power system operator (Mohseni & Islam, 2012)	32
Figure 3.2: Frequency operating limits in some of the European countries	32
Figure 3.3: Active power regulation strategies (de Alegria, et al., 2007)	33
Figure 3.4: Power-frequency response curve by Danish grid code (Mohseni & Islam, 2012).....	36
Figure 3.5: Reactive power and power factor requirement as enforced by Danish grid code (Mohseni & Islam, 2012)	36
Figure 3.6: Reactive power support requirement as defined by German grid code (Mohseni & Islam, 2012).....	37
Figure 3.7: German LVRT requirement (Mohseni & Islam, 2012).....	37

Figure 3.8: South African LVRT curve (Mchunu & Khoza, 2013).....	38
Figure 3.9: Requirement for reactive power support during grid fault according to the South African grid code (Mchunu & Khoza, 2013).....	38
Figure 3.10: LVRT enhancement techniques	41
Figure 3.11: Block diagram of a typical BPA controller.....	41
Figure 3.12: Braking chopper configuration.....	43
Figure 3.13: Energy storage system connected to the DC-link.....	43
Figure 3.14: Typical structure of a STATCOM.....	43
Figure 3.15: Typical configuration of a dynamic voltage restorer.....	44
Figure 3.16: Typical configuration of a unified power flow controller.....	44
Figure 4.1: PMSG based wind turbine system	47
Figure 4.2: Power coefficient as a function of tip speed ratio (Perelmuter, 2013)	47
Figure 4.3: Drive train schematic modelling	48
Figure 4.4: Representation of a 2-pole, 3-phase, star connected PMSG.....	49
Figure 4.5: Phasor diagram of a PMSG	50
Figure 4.6: Simplified equivalent circuits of PMSG	53
Figure 4.7: Machine side rectifier	54
Figure 4.8: Grid side inverter.....	54
Figure 4.9: Power flow in the WTS.....	55
Figure 4.10: Direction of power flowing through the inverter.....	56
Figure 4.11: Phasor diagram of the field-oriented control.....	56
Figure 4.12: Generator side converter control	58
Figure 4.13: Grid side converter control	59
Figure 4.14: Two-level voltage source converter topology	61
Figure 4.15: Space vector diagram of the two-level inverter.....	62
Figure 4.16: Space vector diagram of the grid side inverter	65
Figure 4.17: Seven-segment switching sequence for reference vector located in sector I	67
Figure 5.1: Single line diagram of the electric power system under study	69
Figure 5.2: Wind speed profile	71
Figure 5.3: Generator speed	71
Figure 5.4: Turbine mechanical torque.....	71
Figure 5.5: Wind turbine's power coefficient.....	72
Figure 5.6: Wind turbine's tip speed ratio	72
Figure 5.7: Three phase stator voltages.....	72
Figure 5.8: Three phase stator currents	73
Figure 5.9: Stator active power	73
Figure 5.10: d and q-axis stator currents with references.....	74
Figure 5.11: Three-phase grid voltages.....	74

Figure 5.12: Three phase grid currents	74
Figure 5.13: DC-link voltage.....	75
Figure 5.14: Current through DC-link	75
Figure 5.15: DC-link power	75
Figure 5.16: d and q-axis grid currents with references.....	76
Figure 5.17: Grid active power	76
Figure 5.18: Reactive power to the grid	76
Figure 5.19: Grid frequency	77
Figure 5.20: Block diagram of the pitch angle controller.....	78
Figure 5.21: DC-link protection scheme	79
Figure 5.22: Grid reactive power support scheme.....	80
Figure 5.23: Voltage profile during fault at bus 3 for case 1.....	81
Figure 5.24: Voltage profile at PCC during grid fault for case 1.....	82
Figure 5.25: Grid active power output during grid fault for case 1.....	82
Figure 5.26: DC-link voltage during grid fault for case 1.....	83
Figure 5.27: Grid reactive power output during grid fault for case 1	83
Figure 5.28: Voltage profile during fault at bus 3 for case 2.....	84
Figure 5.29: Voltage profile at PCC during grid fault for case 2.....	84
Figure 5.30: Grid active power output during grid fault for case 2.....	85
Figure 5.31: DC-link voltage during grid fault for case 2.....	86
Figure 5.32: Grid reactive power output during grid fault for case 2	86
Figure 5.33: Voltage profile during fault at bus 3 for case 3.....	87
Figure 5.34: Voltage profile at PCC during grid fault for case 3.....	87
Figure 5.35: Grid active power output during grid fault for case 3.....	88
Figure 5.36: DC-link voltage during grid fault for case 3.....	88
Figure 5.37: Grid reactive power output during grid fault for case 3	89
Figure 5.38: Voltage profile during fault at bus 3 for case 4.....	89
Figure 5.39: Voltage profile at PCC during grid fault for case 4.....	90
Figure 5.40: Grid active power output during grid fault for case 4.....	90
Figure 5.41: DC-link voltage during grid fault for case 4.....	91
Figure 5.42: Grid reactive power output during grid fault for case 4	91
Figure 5.43: Voltage profile during fault at bus 3 for case 5.....	92
Figure 5.44: Voltage profile at PCC during grid fault for case 5.....	92
Figure 5.45: Grid active power output during grid fault for case 5.....	93
Figure 5.46: DC-link voltage during grid fault for case 5.....	93
Figure 5.47: Grid reactive power output during grid fault for case 5	94
Figure 5.48: Voltage profile during fault at bus 3 for case 6.....	94
Figure 5.49: Voltage profile at PCC during grid fault for case 6.....	95

Figure 5.50: Grid active power output during grid fault for case 6.....	95
Figure 5.51: DC-link voltage during grid fault for case 6.....	96
Figure 5.52: Grid reactive power output during grid fault for case 6	96
Figure 5.53: Voltage profile during fault at bus 3 for case 7.....	97
Figure 5.54: Voltage profile at PCC during grid fault for case 7.....	97
Figure 5.55: Grid active power output during grid fault for case 7.....	98
Figure 5.56: DC-link voltage during grid fault for case 7.....	98
Figure 5.57: Grid reactive power output during grid fault for case 7	99
Figure 5.58: Voltage profile during fault at bus 1 for case 8.....	99
Figure 5.59: Voltage profile at PCC during grid fault for case 8.....	100
Figure 5.60: Grid active power output during grid fault for case 8.....	100
Figure 5.61: DC-link voltage during grid fault for case 8.....	101
Figure 5.62: Grid reactive power output during grid fault for case 8	101
Figure B.6.1: Electric power system model	113
Figure B.6.2: Complete model of the PMSG wind energy conversion system	114
Figure B.6.3: Simulation model of the generator side converter	115
Figure B.6.4: Simulation model of the grid side converter	116

LIST OF TABLES

Table 2.1: Comparison of different wind turbine concepts	21
Table 3.1: Classification of RPPs according their rated power (Mchunu & Khoza, 2013)	39
Table 4.1: Switching states and output voltages of the inverter	63
Table 4.2: Space vectors, switching states, and vectors definition	64
Table 4.3: Relationship between reference vector location and dwell times	66
Table 4.4: Seven segment switching sequence	67
Table A.1: Individual wind turbine parameters	111
Table A.2: Generator parameters.....	111
Table A.3: DC-link parameters.....	111

CHAPTER ONE

INTRODUCTION

1.1 Background to the research problem

There is no secret about the importance of electricity in the modern industrialized world. Electricity is needed for lighting, telecommunications, IT, cooking, transportation, or even for medical purposes, just to name but a few. In fact, contemporary society tends to depend completely upon electricity at such an extent that it will be difficult to even imagine life without electricity (Breeze, 2005).

One of the largest industries in the world is certainly the industry of power generation. Its environmental impact is just as much important, with pollution and climate change associated to the burning of fossil fuels, which constitute without any doubt the most used energy sources for electricity generation in the world (Breeze, 2005).

The use of nuclear energy for electricity generation could eventually help contain and even reduce at long term the global carbon emission. However, there are concerns about not only the disposal of radioactive waste, but also the safety of nuclear reactors. A very fresh and concrete example is the Fukushima nuclear disaster which took place on March 11, 2011 (Basrur & Koh, 2012).

On the other hand, with demographic growth and social and economic development, the global energy supply will continue to rise in order to satisfy global energy demand. The International Energy Agency (IEA, 2012) predicts a 1.7 billion increase in world's population between 2010 and 2035, and consequently about 37% increase in global energy demand over the same period.

Taking all these issues into consideration, it is clear that the power generation industry can no longer simply rely on traditional means of electricity generation to achieve clean, reliable and sustainable energy supply. Therefore, the need to consider alternative energy supply technologies is imperious.

Renewable energy sources, due to their abundance and cleanliness, seem to be able to provide both the environmental and energy security that fossil fuels cannot guaranty (Tong, 2010). However, cost issues still make many governments reluctant to engage towards renewables, although majority of people, including researchers, find them very attractive and full of benefits (Craddock, 2008).

Over the past decade, the research industry has paid a particular attention to wind energy among all other renewable energy sources. This interest has resulted in the fast emergence of various wind generators and power electronics converters technologies, leading to a major boost in terms of the global wind power production capacity.

However, transient stability and power quality issues are important challenges that come with this increasing penetration level of wind power in the power system (Ali, 2012). As such, wind turbines are nowadays expected to behave like conventional power plants and should therefore meet certain connection requirements for safe and reliable grid connection. Some of these requirements include frequency and voltage control, as well as fault ride-through (FRT) capability (Patel, 2006).

1.2 Wind energy worldwide

Wind energy has shown a considerable increase in terms of installed capacity in the past two to three decades as shown in Figure 1.1 and Figure 1.2. This is particularly true for Asia which by end of 2014 took over the first place with 142 GW cumulative installed capacity at the expense of Europe and its 134 GW. China, among any other country has experienced the most significant increase especially in the past five years where the capacity has basically doubled. The country has a huge share in the Asian region with a total 114.6 GW capacity. China is followed from a distance by India and its 22.4GW. In Europe, the cumulative installed capacity is about 134 GW, although the 2014 contribution was almost insignificant in certain leading countries such as Spain (28MW). However, the country is still ranked second (23 GW), behind Germany (39 GW). America is still led by the US and its overall 65.8 GW. Canada has an impressive 2014 year with its highest installed capacity in a year of about 1.87 GW. Africa is still at an early stage, North African Morocco (787 MW) and Egypt (610 MW) having the larger share of the total installed capacity for the continent. South Africa however has taken the third position with its 570 MW (Ren21, 2015).

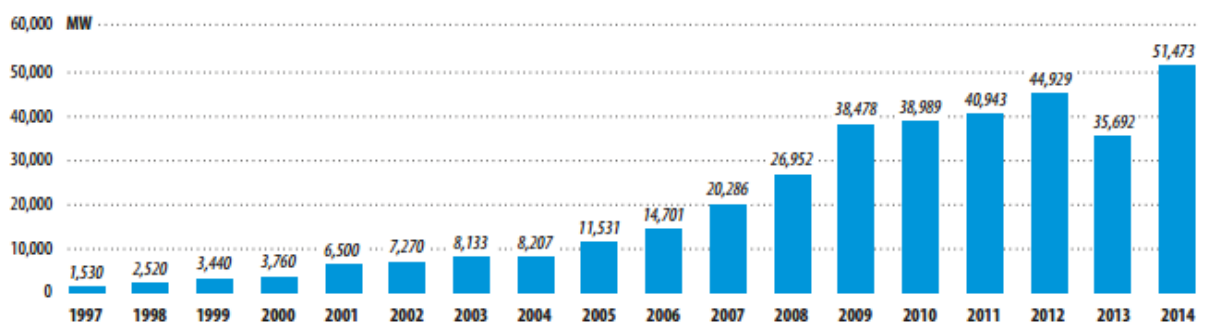


Figure 1.1: Global annual installed wind capacity (GWEC, 2015)

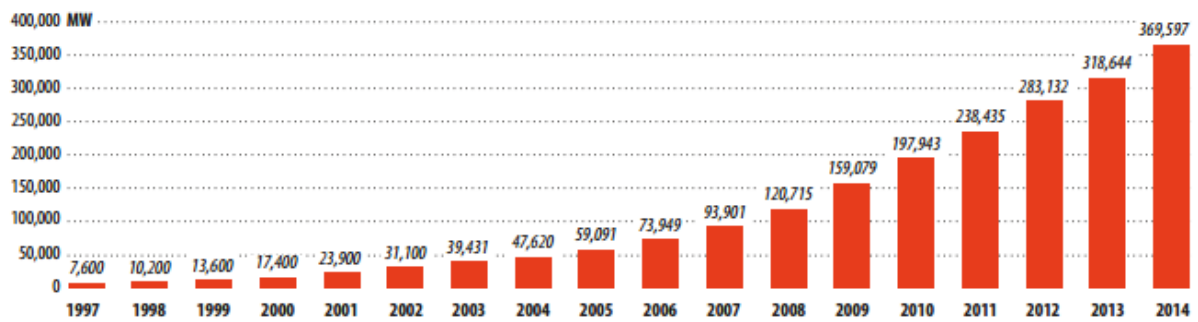


Figure 1.2: Global cumulative installed wind capacity (GWEC, 2015)

1.3 Wind energy in South Africa

In 2014, South Africa had finally taken a serious option into the wind industry with its 560 MW capacity installed over the year. This obviously represents a tremendous step forward considering that it took about a decade for the country to see its first 10 MW installed.

For many years, South Africa has completely relied on fossil fuels for electricity generation, 88% of the power produced coming from coal. This is completely understandable provided the country hosts one of the largest coal deposits in the world. However, the price of electricity keeps increasing as illustrated in Figure 1.3, and the population is still suffering from the consequences of multiple power blackouts (GWEC, 2015).

As part of a solution to the country's energy crisis, the South African government has decided to shift towards renewable energies, essentially through its REIPPPP (Renewable Energy Independent Power Producer Procurement Program). This program was established in 2011 with the aim of promoting the rapid expansion of renewable energy in the South African electricity market, without risks of excessive losses due to overpricing in case of a single power producer. This would be done by allocating different projects to different independent power producers over five round bids. Since then, over 5 GW have already been allocated in four rounds, of which about 1.5 MW is already supplying to the national grid (Greencape, 2015).

As far as wind energy is concerned, 2660 MW have already been allocated with 660 MW remaining for the last round. Wind energy has the highest allocation so far, followed by solar energy. The year 2014 saw the first results from the REIPPPP with some of the first bid wind farms coming into operation (Greencape, 2015). Currently operating large wind farms in South Africa include Sere (100 MW), Cookhouse (138.6 MW), Jeffreys Bay (138 MW) Nobelsfontein (73.8 MW) and more (Writer, 2015).

The integration of wind energy through the REIPPPP has so far been successful and shows promising future. For this reason, the Integrated Resource Plan (IRP) has planned for an

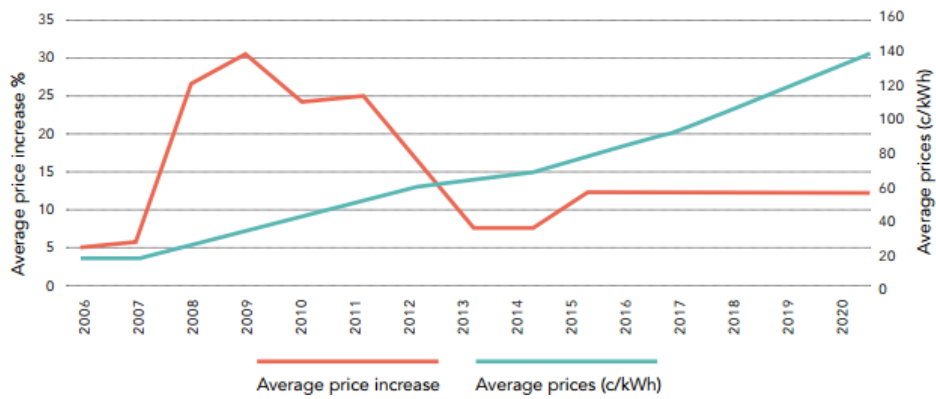


Figure 1.3: Historic Eskom electricity price increases (Writer, 2015)

additional 8.4 GW installed wind power capacity by the year 2030 and calls for more bid rounds (Greencape, 2015). This plan clearly shows that the wind industry in South Africa is entering a different phase.

1.4 Statement of the research problem

In the past, a grid fault such as short circuit or any other serious disturbance would require wind generation interruption. By simply tripping off the faulty line, the wind turbine was easily isolated from the rest of the network to prevent it from damages (Patel, 2006; Sourkounis & Tourou, 2013). Today, with the high installed wind turbine capacity, disconnection is no longer an option, especially for short duration grid faults. In fact, suddenly disconnecting wind power plants from the power system could lead to severe voltage dips and even power system breakdown, especially with a massive wind penetration levels (Chen, et al., 2009; Sourkounis & Tourou, 2013).

Reducing the output power of the turbines during grid faults could minimize the risks of power system breakdown. This method however proves to be economically costly for wind farm operators. Moreover, constant backup is required from conventional power plants whenever a grid fault occurs. This high dependence of wind farms on other conventional generation power plants during grid faults represents a clear obstacle to wind integration in the power system (Marrone, 2014).

This situation has constrained many countries, especially those having high installed wind power capacity such as USA, Germany or Denmark to review their grid code requirements. As such, recent grid codes require that WPPs have the ability to maintain their connection to the network under certain levels and durations of grid voltage drops (Chen, et al., 2009; Sourkounis & Tourou, 2013; Mittal, et al., 2009). Otherwise, WPPs should have fault ride-through (FRT) capability.

It is therefore important to investigate, through computer simulations and/or hardware experiments, how FRT can be achieved in accordance to grid code specifications, especially with evolving wind generator technologies such as PMSG.

1.5 Rationale and motivations of the research

South Africa is aware of its tremendous wind resource. Even though the country's wind generation is still at a growing phase, SA intends to become one of the countries with most activities in the sector of wind development in the near future. This rapid growth should obviously accommodate with the latest and also most efficient technologies in order to ensure safe and reliable energy supply.

Wind industry is experiencing many changes, especially regarding drive-train technologies (Wenske, 2011). As such, direct driven wind turbines equipped with PMSGs are becoming more attracting and their market share is also increasing, due to their multiple advantages over other drive-train topologies (Wenske, 2011; Sanchez, et al., 2012; Gupta, et al., 2012).

With the increasing penetration of PMSG in the world's wind market, a massive investigation into the compliance of this type of generator with different grid codes requirements is necessary. South Africa is an emerging wind power country and therefore such study needs to be carried through in order to facilitate wind integration. According to Sourkounis & Tourou (2013), FRT and more specifically low voltage ride through (LVRT), is the most important grid code requirement for wind farms. This explains the choice of this topic for the research.

1.6 Research aim and methodology

The aim of this research is to achieve FRT capability with a multiple-pole PMSG grid connected WECS according to South African grid code requirements. In order to achieve this goal, the following tasks must be completed:

- Modelling and Analysis of the PMSG based wind turbine system
- Implementation of the electric power system benchmark
- Design of the control system to achieve FRT of multi-pole PMSG
- Implementation of LVRT control on wind turbine system for different grid faults
- Analysis and interpretation of simulated and experimental results

1.7 Delineations of the research

In this research, the LVRT capability of a multi-pole PMSG is investigated according to South African grid code requirements. Simulation studies are carried through with emphasis on the case of symmetrical faults which are the most severe types.

1.8 Thesis organisation

This thesis is organised in seven chapters. Chapter one, the introduction gives an overview of the evolution of wind energy at global and national levels. The importance of this research as well as its aim and contributions are well defined. Research methods and thesis organisation are discussed. The second chapter is a review of different wind turbine configurations. The chapter firstly describes different components available in typical wind turbine systems. Then, different rotor, generator, drive-train, and power converter topologies are discussed and compared. Aerodynamic and electrical control strategies are also discussed. In the third chapter, grid code requirements and LVRT solutions are discussed. The E-on, Danish and South African grid codes are elaborated. The LVRT requirement is well explained and common LVRT enhancement methods are discussed and compared. The fourth chapter presents a detailed modelling of the wind turbine system as well as power system benchmark used. Chapter five shows the implementation of the LVRT strategies used in this thesis. Simulation results are presented, analysed and interpreted in chapter six. Conclusions are drawn in the chapter seven. Recommendation for further improvement of the research or inspection of other aspects are also given at the end of this chapter.

CHAPTER TWO

WIND TURBINE CONFIGURATIONS

Introduction

This chapter is an overview of the different wind turbine concepts available and currently used in the market. In fact, with recent advances in science and technology, many turbine topologies have evolved over the years, each one trying to overcome the previous shortfalls. This has led to significant improvements in terms of wind energy harvesting, structural strength, energy efficiency (mechanical and electrical), and overall reliability of wind turbines, to guarantee safe and reliable supply at lower cost.

The wind turbine topology used in this thesis was chosen based on certain criteria after comparing the other topologies. In this chapter, a review of some of the most common wind turbine concepts is presented. Firstly, the basic components of a wind turbine are presented with their functions explained. Then follows an explanation of the aerodynamic operating principles, and finally a comparison of the different wind turbine concepts according to their rotor, generator, and power electronics concepts.

2.1 Components of wind turbines

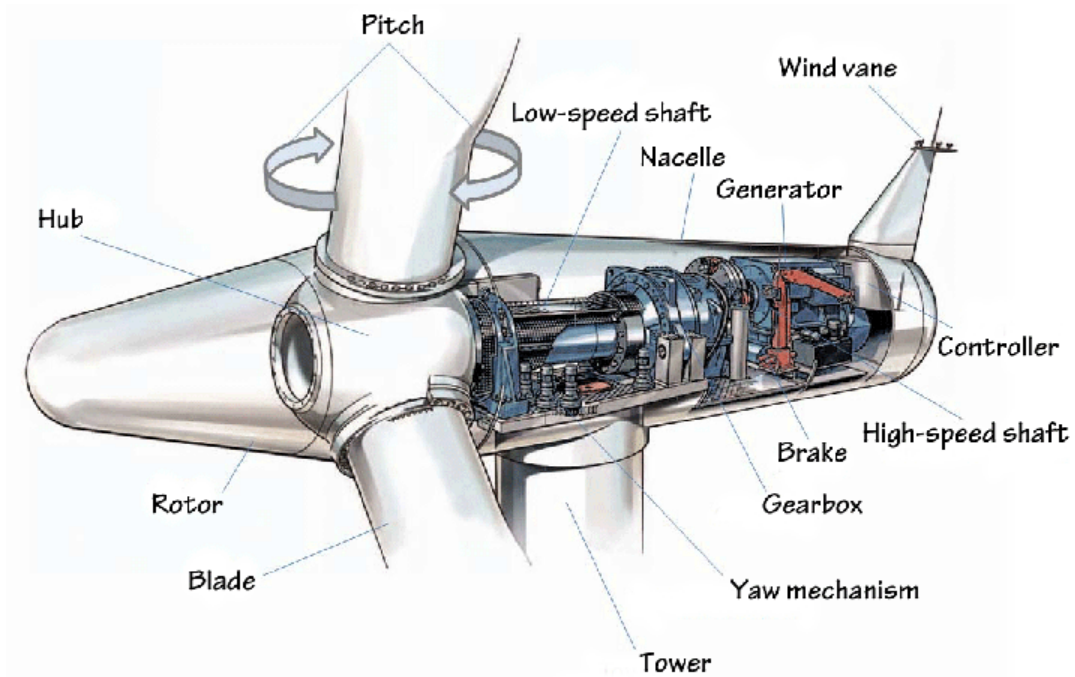


Figure 2.1: Components of a wind turbine system

The major components that constitute a wind turbine are represented in Figure 2.1. They can be grouped into five main sections namely the rotor, the drive train, the frame, the yaw system and the tower. Some of the components are discussed below (Manwell, et al., 2009; Wu, et al., 2011; Hansen, 2008).

The rotor

The rotor is the part responsible for the extraction of wind power to be converted into rotational movement in order for the turbine to generate electrical power. The turbine blades, the hub, and the aerodynamic control surfaces essentially constitute the rotor of a wind turbine.

The blades

The blades create the torque needed for the wind turbine to produce useful electrical power from the wind blow. The blades must be designed in such a way that their shape and material facilitate not only maximum extraction of wind energy, but also sufficiently withstand physical stress caused by strong winds and excessive loads.

The hub

The hub is the part that links the turbine's shaft to the blades and transmits the torque produced to the drive train.

The drive-train

The drive-train includes all rotating components, the main shaft, gearbox, brakes, and generator.

The brakes

Brakes are used to block the rotor from rotating, to allow maintenance on the wind turbine or in case of emergency whenever there is a fault on the turbine itself or even in the power system.

The main shaft

Also called low speed shaft, the main shaft transfers the rotational force from the blades to the remainder of the drive train.

The gearbox

This component multiplies the low speed from the main shaft to match the generator's high speed shaft (mostly 1500rpm and 1800rpm). Due to its weight, price, and need for constant maintenance the gearbox is becoming less desirable in modern wind turbines.

The generator

The generator is the electrical machine that converts the mechanical rotational power from the main shaft into electrical power to be supplied to load.

The yaw system

The yaw system has the mission to ensure that the turbine faces the wind, allowing maximum energy to be extracted.

The nacelle

The nacelle is the frame that contains the shaft, the gearbox, the generator, and many other parts.

The tower

The tower is the structure that supports all the nacelle components in altitude, allowing the blades to freely sweep the wind over their diameter without risks of crashing on the ground.

Anemometers (wind sensors)

Wind sensors measure the speed as well as the direction of the wind necessary for blade orientation at different.

2.2 Wind turbine aerodynamics and characteristics

2.2.1 Power in the wind

The energy available in the wind can be expressed as (Wagner & Mathur, 2009)

$$E_{wind} = \frac{1}{2}mV^2 \quad \text{Equation 2.1}$$

where m represents a certain mass of air flowing at wind speed V . this mass of air is proportional to the air density ρ , the area swept by the blades A , and the wind speed V over a specific period of time t , and can further be expressed as:

$$m = \rho AVt \quad \text{Equation 2.2}$$

Equation 2.2 can be substituted in into Equation 2.1 and the following expression for the energy in the wind is obtained:

$$E_{wind} = \frac{1}{2}\rho AV^3t \quad \text{Equation 2.3}$$

Since

$$P_{wind} = \frac{E_{wind}}{t} \quad \text{Equation 2.4}$$

The power available in the wind can thus be given as:

$$P_{wind} = \frac{1}{2}\rho AV^3 \quad \text{Equation 2.5}$$

2.2.2 Turbine power

As it can be seen in Equation 2.5 above, the wind power is proportional to the air density, the wind speed, and the area of the wind turbine rotor. However, not all the power in wind is used by the wind turbine. According to the Betz limit, only a fraction (approximately 59.3%) of

the wind power can be extracted by the wind turbine and is known as Power Coefficient (C_p). Therefore, the maximum power extracted from the wind is given as (Ackermann, 2005):

$$P_{turbine} = \frac{1}{2} \rho A V^3 C_p \quad \text{Equation 2.6}$$

2.2.3 Power coefficient and tip speed ratio

Equation 2.6 above can be rewritten as:

$$P_{turbine} = P_{wind} \times C_p \quad \text{Equation 2.7}$$

Making C_p the subject of the formula, the power coefficient can be expressed as:

$$C_p = \frac{P_{turbine}}{P_{wind}} \quad \text{Equation 2.8}$$

From the previous expression, the power coefficient can be defined as the ratio of the power extracted by the turbine blades to the available power in the wind. The power coefficient can also be seen as the efficiency of the rotor blades (Wagner & Mathur, 2009).

The tip speed ratio is the ratio of the rotor's speed at the tip of the blade and the wind speed and is expressed as:

$$\lambda = \frac{r\omega}{V} \quad \text{Equation 2.9}$$

where r is the radius of the turbine's rotor blade, and ω the rotating speed of the blade.

The power coefficient being a function of λ and β , the turbine power can also be written as:

$$P_{turbine} = \frac{1}{2} \rho A V^3 C_p(\lambda, \beta) \quad \text{Equation 2.10}$$

2.2.4 Power curve

The power curve is an important characteristic of wind turbines. The power curve shows the expected output power produced by a turbine at different wind speeds. Figure 2.2 below represents a typical power curve for a wind turbine. As illustrated, there are three wind speed limits that determine the shape of the power curve: the cut-in speed, the cut-out speed, and the rated speed. The cut-in speed is the minimum wind speed at which the turbine starts producing power and usually ranges between 2 to 5 m/s. At wind speeds below this value, not sufficient torque is produced to cause effective rotation of the turbine; no output power is thus produced. The rated speed represents the wind speed at which rated power will be produced by the wind turbine and ranges between 12 and 15 m/s. At wind speeds above rated value, the output power is usually maintained constant using aerodynamic control mechanisms. The cut-out speed on the other hand is the value above which the turbine may

start experiencing turbulences which could lead to damage. This value usually revolves around 25 m/s. As shown figure 2.2, passed the cut-out speed, the wind turbine will automatically stop its operation and enter a park mode (Wagner & Mathur, 2009; Wu, et al., 2011).

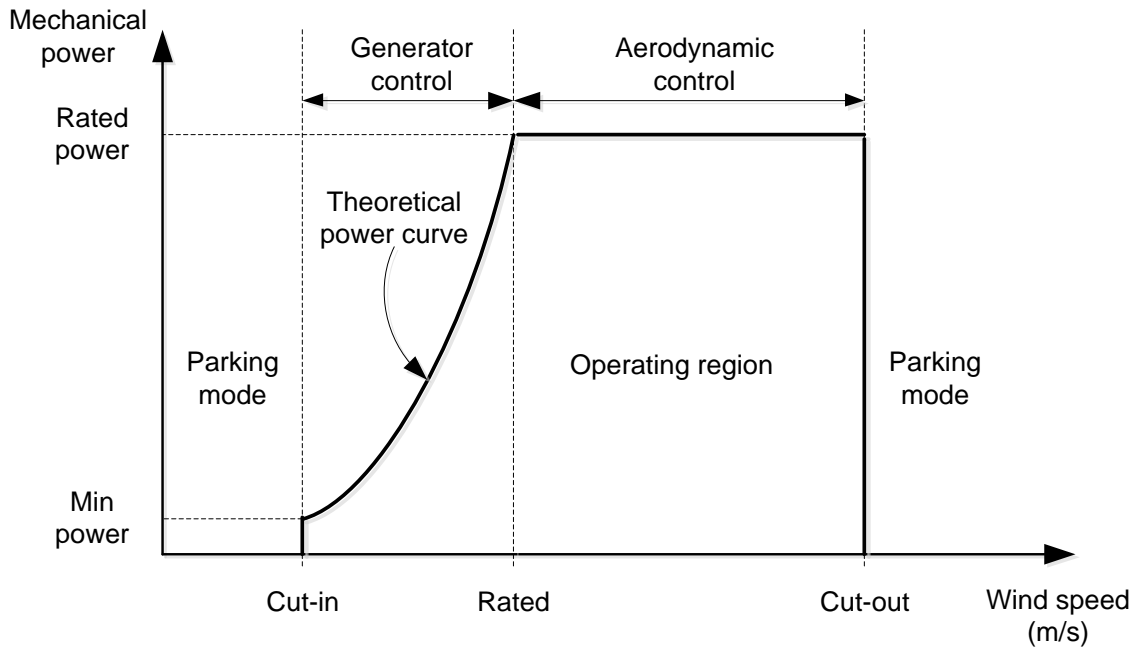


Figure 2.2: Power curve for a wind turbine

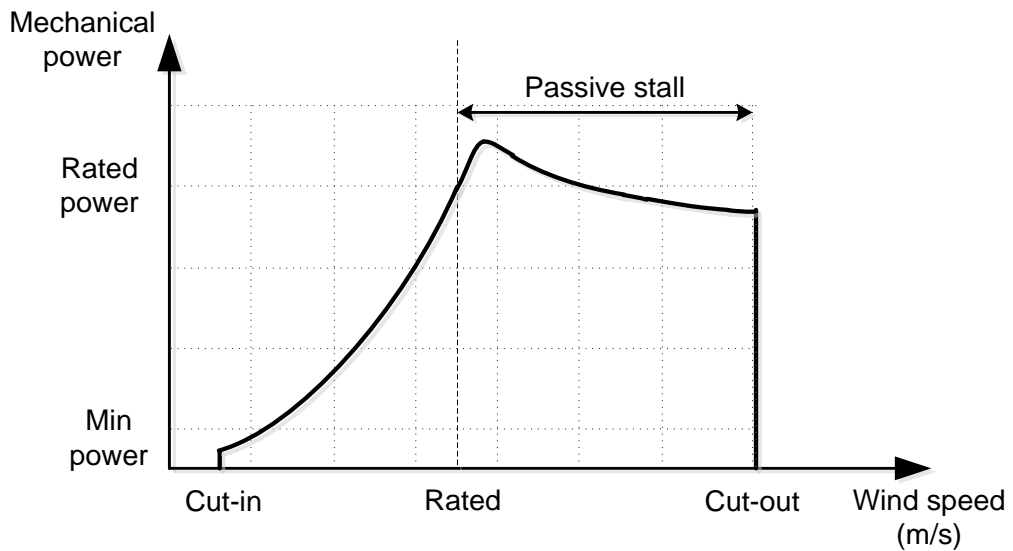


Figure 2.3: Power curve for a passive stall-controlled wind turbine

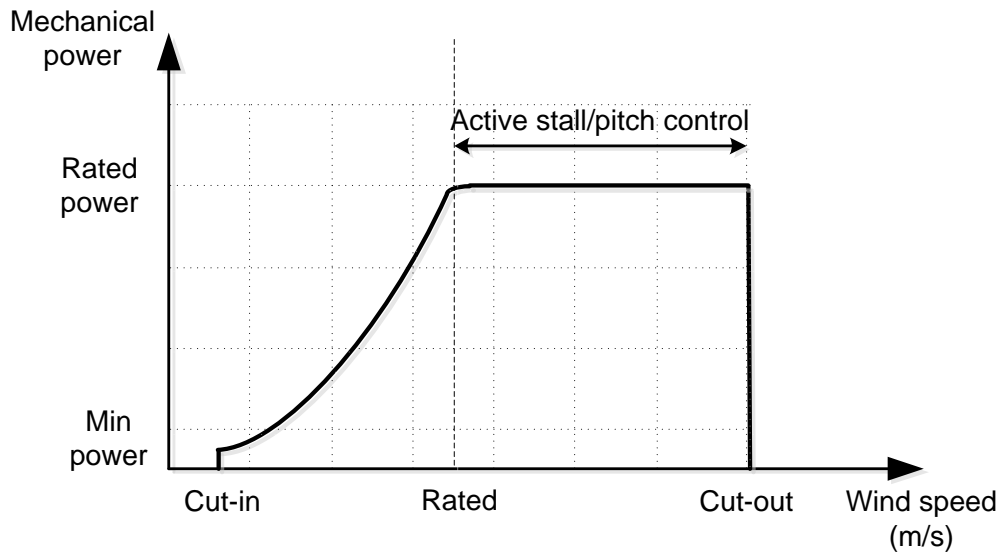


Figure 2.4: Power curve for an active stall and pitch-controlled wind turbine

2.3 Wind turbine aerodynamic controls

The aerodynamic control of wind turbines is important in order to maximize the amount of power to be extracted from the wind, without exposing the turbine to extreme wind conditions that could affect its operation and eventually cause damage or destruction. There are three common methods namely passive stall, active stall, and pitch control.

2.3.1 Passive stall

Passive stall is the simplest and easiest wind turbine aerodynamic control. The amount of energy extracted during high wind speeds conditions is reduced by stalling of the blades, without change of their geometry. The turbine blades are fixed on the hub such that they can only slightly twist around their longitudinal axis. The main difficulty in passive stall control remains the blade design which requires very precise aerodynamic properties of the blades to ensure more effective stall effect (Wagner & Mathur, 2009; Earnest, 2015; Munteanu, et al., 2008).

2.3.2 Active stall

In Active stall control, the blades are turned into the direction of the wind to stall. As opposed to passive stall, the blades can completely rotate around their longitudinal axis. The principal advantage over pitch control is that active stall only requires small pitch rate changes to maintain rated power output. Another advantage is the reduced strain on the generator during high wind conditions (Wagner & Mathur, 2009; Earnest, 2015; Munteanu, et al., 2008).

2.3.3 Pitch control

In pitch control the blades are deviated out of the direction of the wind to reduce the power captured, eventually slowing down the turbine whenever the wind speed goes beyond its rated value. Pitch control is similar to active stall only that the blades are turned into the wind direction in active stall. Moreover, the pitch system has to act quickly, in order to limit power excursions, due to their large range of pitch angles for rated power output control. However, the pitch control presents numerous advantages over stall control such as increased energy capture, ease in aerodynamic braking, and overload reduction when the turbine is shut down (Wagner & Mathur, 2009; Earnest, 2015; Munteanu, et al., 2008).

2.4 Wind turbine topologies

Generally, WTs classifications are made according to the rotor configurations, the generator technologies, and the turbine's rotational speed (Ackermann, 2005; Hau, 2013).

2.4.1 Wind turbines' rotor configurations

Modern wind turbines have rotors with a horizontal axis of rotation, or with a vertical axis rotation as presented in Figure 2.5. Both configurations present advantages and disadvantages depending on their location, the wind speed, the range of power, the positioning of the components, and also blade design.

VAWTs have their rotor shafts oriented vertically, that way energy from the wind is easily extracted regardless of its direction. Components such as the gearbox and the generator can be easily accessed for maintenance due to their relatively low positioning. However, since stronger winds are found in altitude, these types of turbines do not necessarily extract high amounts of energy. Moreover, VAWTs are not easily pitch controlled during high wind speeds.

HAWTs have their rotational axis oriented horizontally. They are usually made of three blades, but they can be equipped with one, two, and even more than three blades. Also, depending on the direction of the wind they can be upwind or downwind. The fact that the turbine blades can sweep a much wider area, and that they are positioned relatively high, eases the extraction of more wind energy compared to VAWTs. HAWTs are the most popular and are mostly used in medium to high power applications. Hence, only these types of wind turbines will be discussed throughout.



Figure 2.5: Wind turbine rotor configurations

2.4.2 Wind turbines' generators

The generator is one of the most important components in a wind turbine and can play a major role in its overall operation, as well as reliability and efficiency. Generators for wind turbines can be of DC, synchronous or asynchronous AC type (Cao, et al., 2012). DC generator technologies are not commonly used for wind turbines except in applications such as battery charging whereby the load and the turbine are at a very short distance from each other. AC generators on the other hand are being used in most wind turbines

Induction generators are widely used in wind power generation especially in large modern wind farms. They are cheap and mechanically robust and simple. The two common types are the wound rotor induction generator (WRIG) and the squirrel cage induction generator (SCIG). The limiting factors however of these types of generators are among others their low efficiency, reliability, and their ability to draw reactive power from the grid (Cao, et al., 2012).

Synchronous generators on the other hand have the advantage that they do not consume reactive power, but they are more expensive and mechanically complex than induction generators. For wind turbine application, the WRSG and the PMSG are mostly used. Yet, the PMSG is progressively improving its share in the market due to numerous advantages (Cao, et al., 2012).

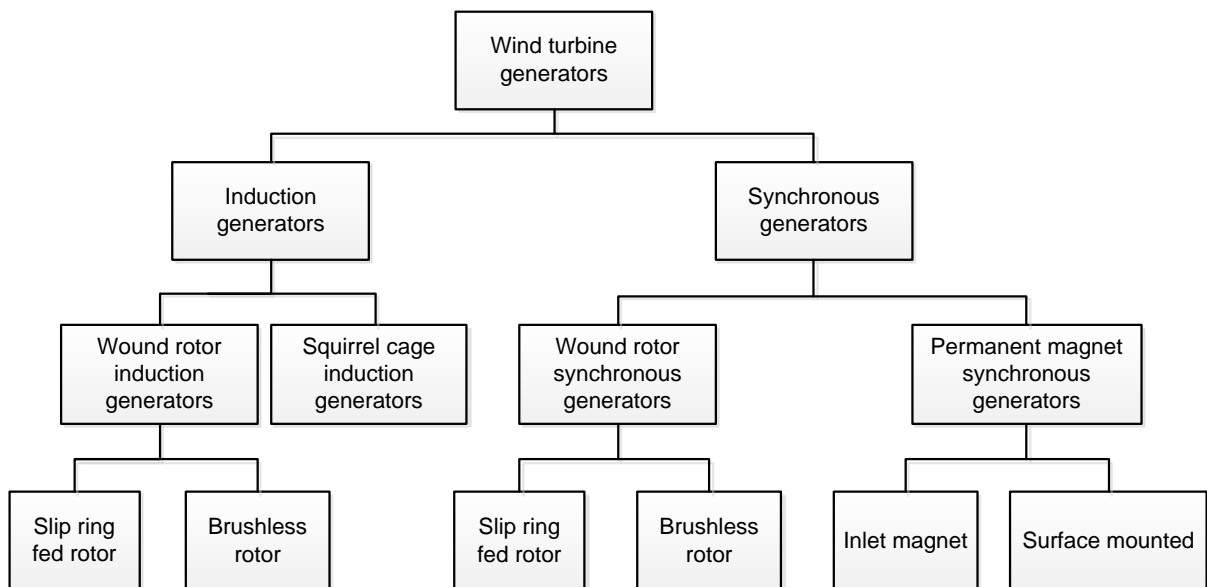


Figure 2.6: Classification of different wind turbine generators

2.4.3 Wind turbines rotational speed configurations

As far as the rotational speed is concerned WT's can operate at fixed speed, limited variable speed, and variable speed, with respect to the type of power converter employed. A classification of different concepts is given in Figure 2.7 and a summary of their comparison is given in Table 2.1.

Variable speed concepts are more attracting due to their ability to deliver maximum power over a wide range of wind speeds, as opposed to the fixed speed and limited variable speed concepts in which maximum efficiency is achieved only at a particular wind speed. The PECs in variable speed concepts also allow smooth grid connection as well as reactive power compensation (Blaabjerg, et al., 2009)

The doubly-fed induction generator (DFIG) is still the most widely used technology at this time, but recent reports show that type 4 will soon overcome the type 3 provided the advantages such as the possibility for a direct-drive, and easiness to achieve grid connection requirements compared to the DFIG (Blaabjerg, et al., 2009).

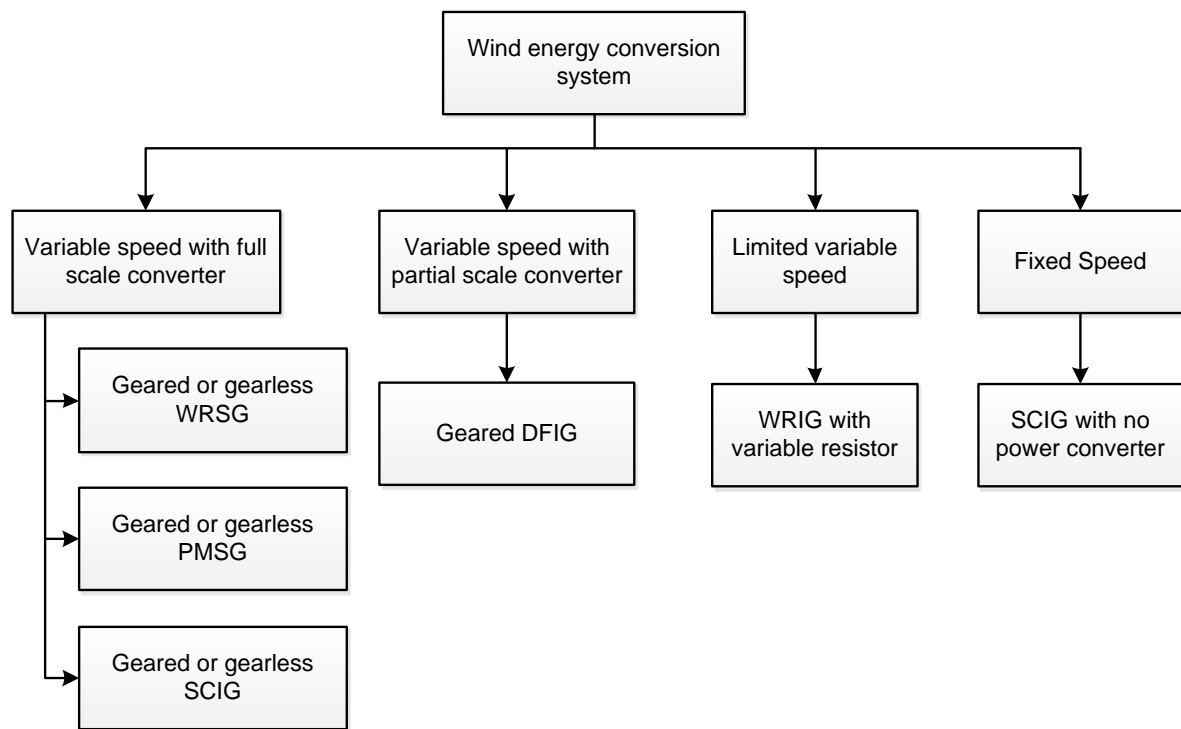


Figure 2.7: Classification of different wind turbine concepts

2.4.3.1 Fixed speed concept (type 1)

Type 1 emerged in the 1980's, and was developed by the Danish, hence the other appellation "Danish concept". This concept is made of a SCIG directly attached through a transformer to the power grid. Capacitor banks are used for reactive power compensation. A soft-starter is also used to limit the excessive generator current at start-up. The main advantage of this configuration is its simplicity and robustness. However, since the rotational speed is constant, a major drawback is that under turbulent wind conditions, the rotor can be easily exposed to heavy mechanical stresses (Camm, et al., 2009; Li & Chen, 2008; Blaabjerg, et al., 2009; Polinder, et al., 2007; Bisoyi, et al., 2013).

2.4.3.2 Limited variable speed concept (type 2)

In this concept, the generator type is a WRIG having its stator windings directly linked to the grid, while its rotor windings are connected in series with a variable resistor. With this arrangement, the WT's speed can vary over a certain range (usually up to 10% more than the synchronous speed) determined by the rating of the external resistor. However, there is still the need to incorporate the soft-starter as well as the capacitor bank, as for type 1 (Camm, et al., 2009; Li & Chen, 2008; Blaabjerg, et al., 2009; Polinder, et al., 2007; Bisoyi, et al., 2013).

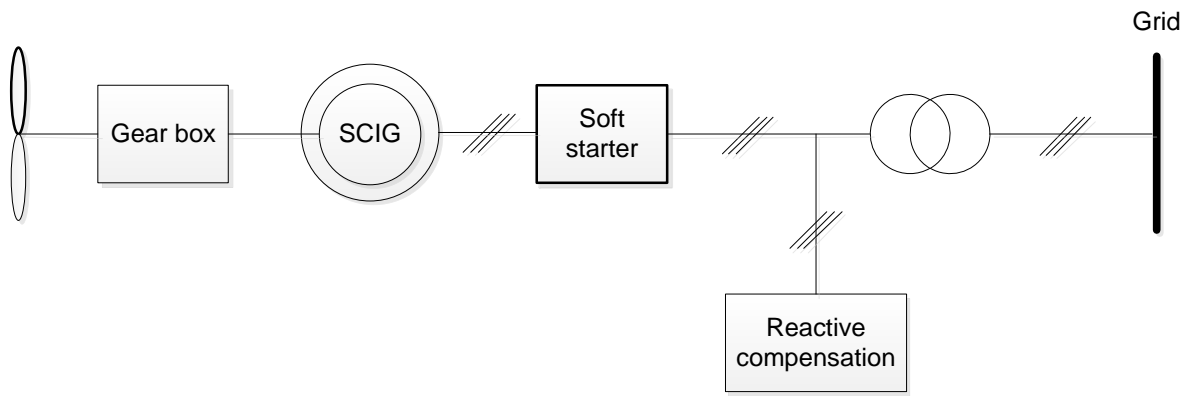


Figure 2.8: Fixed speed concept

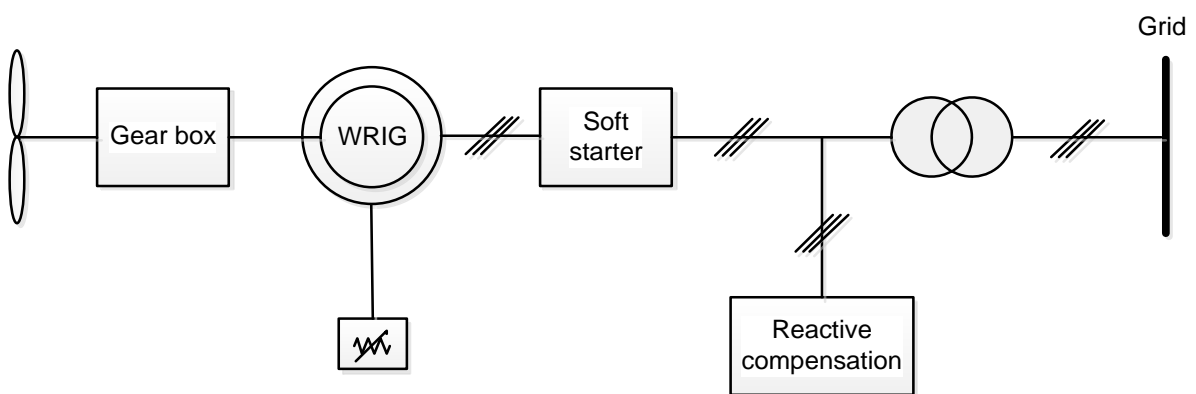


Figure 2.9: Limited variable speed concept

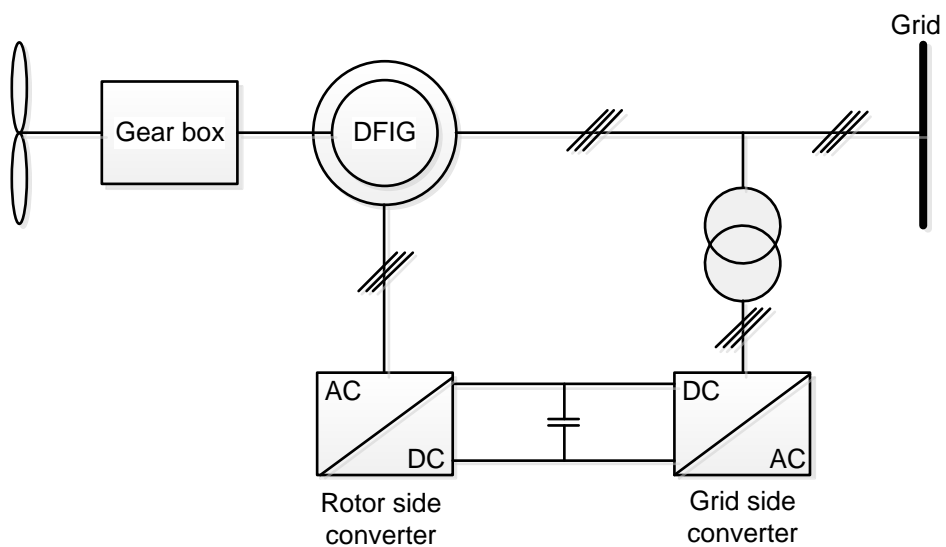


Figure 2.10: Variable speed concept with partial scale converter

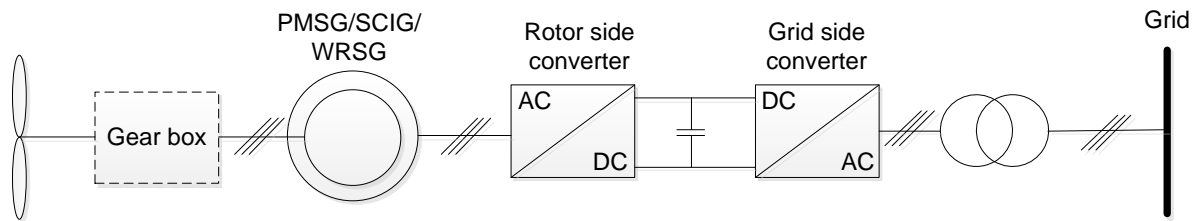


Figure 2.11: Variable speed with full scale converter

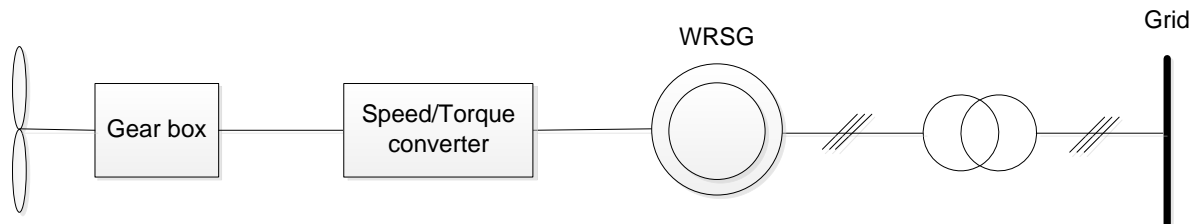


Figure 2.12: Variable speed with direct grid connection

2.4.3.3 Variable speed with partial scale converter concept (type 3)

For the type 3 concept, the speed can vary over a more expanded range compared to the previous type (around 30% of the rated speed in this case). The stator windings are once again connected to the grid with the help of a power transformer. However, this time around, the generator's speed is controlled by a partially rated frequency converter. The converter also manages the generator in-rush current as well as grid reactive power control issues, and thus the soft starter and additional capacitor bank are no longer in need. Meanwhile, there are still some disadvantages associated to the DFIG concept such as its limited wind power harnessing range, and the use of a gearbox (Camm, et al., 2009; Li & Chen, 2008; Blaabjerg, et al., 2009; Polinder, et al., 2007; Bisoyi, et al., 2013).

2.4.3.4 Variable speed with full scale power converter concept (type 4)

In the type 4 concept, the stator windings are connected to the grid through a full-scale power electronics converter. Maximum power can be achieved over the complete operating wind speed range. Additionally, connection to the grid is smoother, and reactive power requirements are more easily achievable compared to the DFIG. However, the principal advantage of the type 4 concept resides on the possibility for a direct connection between the turbine and the generator shafts, without the need for a gearbox. This possibility requires that the generator operate at low speed to match the turbine rotational speed. Therefore, direct-driven wind generators are designed with a relatively large number of poles. Since most mechanical problems are associated with the gearbox, its elimination from the drive

train will considerably reduce chances of mechanical breakdown, and consequently reduce the need for constant maintenance. Moreover, mechanical losses occurring in the gear transmission are eliminated, and the overall efficiency of the WECS can be very much improved. The principal disadvantage of this topology is the cost of the converter as well as its switching losses (Camm, et al., 2009; Li & Chen, 2008; Blaabjerg, et al., 2009; Polinder, et al., 2007).

2.4.3.5 Direct grid connected variable speed (Type 5)

The type 5 is a rather old concept in which the turbine rotor is connected to the generator through a mechanical speed converter which converts the variable turbine speed into a fixed generator speed. The WRSG is directly connected to the grid in the absence of PEC. The advantage of this configuration is cheaper and efficient since power electronics switching losses are inexistent. Although the type 5 presents numerous advantages, this technology is not popular in the wind turbine manufacturing industry due to the lack of experience and expertise, as well as other issues regarding mechanical converters (Nasiri, et al., 2015).

2.5 PMSG in variable speed wind turbines

For many years, PMSGs have been more used in small-scale WPPs and very little in large plants since there would be a need to use massive permanent magnets (PM). Although PMSGs present enormous advantages, factors such as scarcity of the permanent magnet material and their high cost, the problem of demagnetization at high temperatures, and challenges faced during the manufacturing of PM machines have also contributed in slowing the integration of these types of generators in the wind industry (Mittal, et al., 2010; Kilk, 2007). However, recent advances in power electronics technologies and the development of PM material have promoted their expansion into the market of large-scale power plants (de Freitas, et al., 2011).

PMSGs are the state-of-the-art of direct-driven wind turbines for many reasons. They have a smaller diameter, hence reduced weight and THM (Top Head Mass). They can be easily designed with a large number of poles, eliminating the need for a transmission gearbox. Moreover, PMSGs do not have slip rings, brushes or field windings, since their field excitation is produced from PMs, unlike with the SCIG or the EESG in which field excitation is produced from an external DC source. Henceforth, the number of mechanical items, the overall weight, as well as mechanical and electrical losses are considerably reduced, leading to an overall improvement of the efficiency and the reliability of the system (Earnest & Wizelius, 2011). There are different PMSG configurations available for wind turbines, each one of them presenting a number of advantages and disadvantages, depending on their

applications. As such, PMSGs are usually classified according to their flux orientation, magnet mounting, and rotor position (Madani, 2011).

2.5.1 Classification of PMSGs according to their flux orientation

PMSGs can be designed such that the flux path is radial or axial as illustrated in Figure 2.13. In a radial flux permanent magnet (RFPM) machine, permanent magnets are positioned radially, allowing a radial flux orientation, as opposed to the axial flux permanent magnet (AFPM) machine where the flux direction is towards the rotational axis. RFPM machines are simple to design and their manufacturing technology is well established in the industry which makes them less costly compared to AFPM machines. RFPM machines also present design flexibility in stator diameter and length to achieve high power ratings. AFPM machines on the other hand present advantages such as simple winding, reduced cogging torque, shorter stator length. However, they have large number of magnets due to their larger diameter and their air gap cannot be easily maintained (Bang, et al., 2008; Madani, 2011).

Flux orientation can also be longitudinal or transversal. TFPM (Transversal flux permanent magnet) machines are more popular and discussed in literature. In those machines, the flux is perpendicular to the direction of rotation. Their principal disadvantage is their high flux leakages which is usually compensated by reducing the number of poles of the machine, hence reducing the machine's torque density. TFPM are also mechanically less robust due to their increased number of mechanical parts (Bang, et al., 2008; Madani, 2011).

2.5.2 Classification of PMSGs according to the magnet mounting

Permanent magnets are usually mounted on the surface of the rotor. This arrangement is also called surface mounted permanent magnet (SMPM) machines and is illustrated in Figure 2.14. Flux orientation is usually radial. SMPM machines are mostly utilised in large scale direct-drive wind turbine applications. They are easy to manufacture due to their fairly simple geometry (Madani, 2011).

Permanent magnets can also be mounted on the inner of the rotor allowing the presence of rotor core material in between poles also known as iron interpoles, as opposed to the surface mounted configuration in which poles are simply separated by an airgap. These machines present a higher torque density and flux leakage compared to SMPM and are mostly used in geared wind turbines applications (Madani, 2011).

Table 2.1: Comparison of different wind turbine concepts

Turbine type	Type 1	Type 2	Type 3	Type 4		Type 5
Generator	SCIG	WRIG	DFIG	SCIG	PMSG/WRSG	WRSG
Power converter	None	Diode+chopper	AC/DC+DC/AC or AC/AC	AC/DC+DC/AC or AC/AC	AC/DC+DC/AC or AC/AC or AC/DC+DC/DC+DC/AC	None
Converter capacity	0 %	10 %	30 %	100 %	100 %	100 %
Speed range	+ - 1 %	+ - 10 %	+ - 30%	0 – 100%	0 – 100%	0 – 100%
Soft starter	Required	Required	Not required	Not required	Not required	Not required
Gear box	3-stage	3-stage	3-stage	3-stage	3/2/1/0-stage	2-stage
Aerodynamic power control	Pitch, stall, active stall	Pitch	Pitch	Pitch	Pitch	Pitch
MPPT operation	Not possible	Limited	Achievable	Achievable	Achievable	Achievable
External reactive compensation	Needed	Needed	Not needed	Not needed	Not needed	Not needed
FRT compliance	External hardware	External hardware	Power converter	Power converter	Power converter	Power converter
Technology status	Outdated	Outdated	Highly mature	Emerging	Mature	Old concept
Current market penetration	Few/No installations	Few/No installations	Greater than 50 % share	Few installations	2 nd highest share	Few installations
Example commercial WT	Vestas V82, 1.65 MW	Suzlon S88-2.1 MW	Repower 6M, 6.0 MW	Siemens SWT-3.6, 3.6 MW	Enercon E126, 7.5 MW	DeWind D82, 2.2 MW

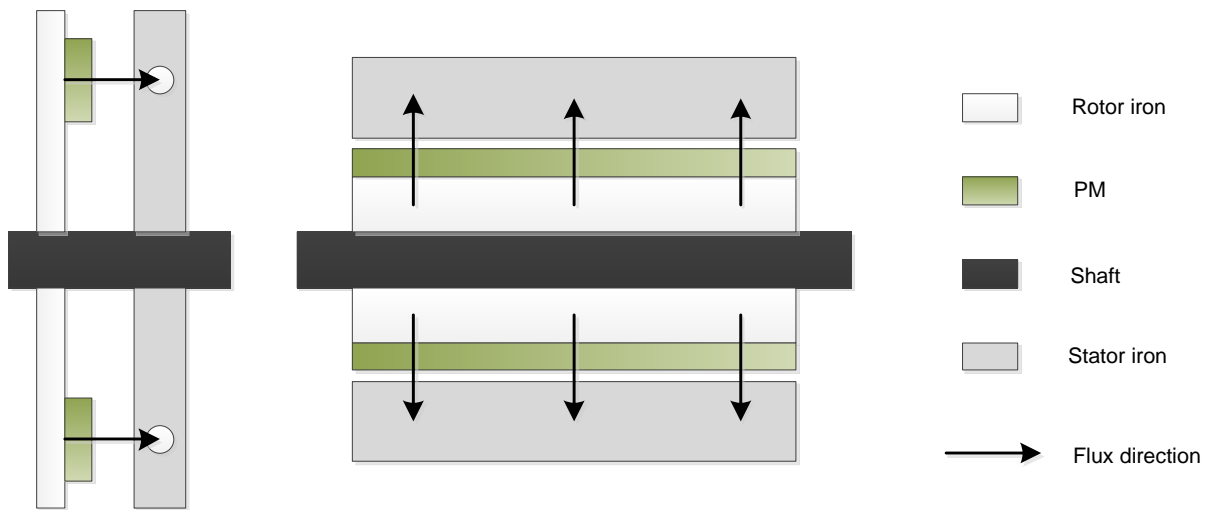


Figure 2.13: Cross sectional view in axial direction of axial flux (left) and radial flux (right) PMSG

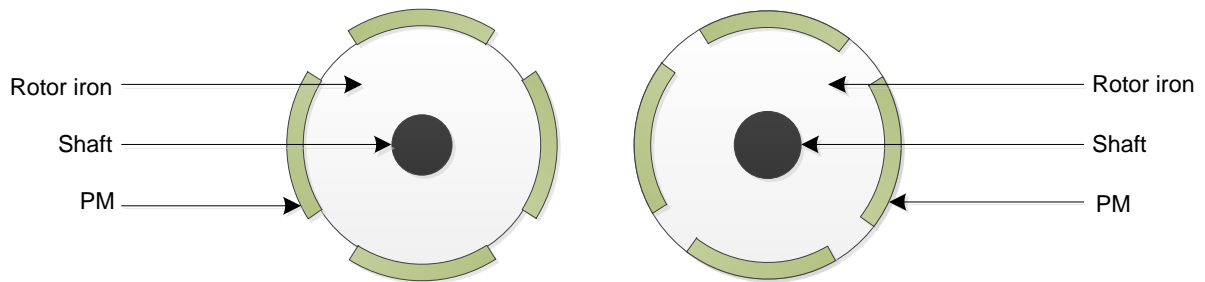


Figure 2.14: Surface mounted (left) and inset (right) magnet rotors for PMSG

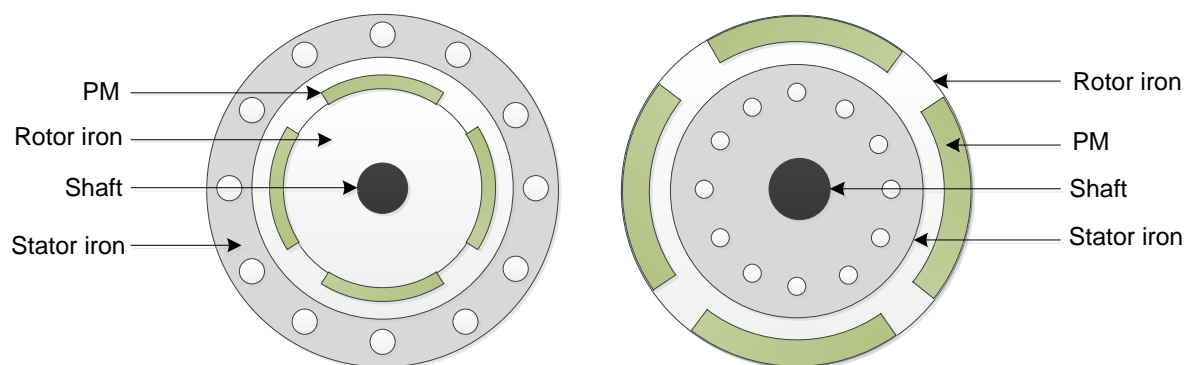


Figure 2.15: Inner (left) and outer (right) rotor PMSG

Finally, PM can be mounted inside the rotor and this configuration is known as buried magnets or interior permanent magnets (IPM). Since the magnets are inside the rotor, magnetization is easier, therefore not so strong PM material may also be used. This topology is not suitable for low speed direct-drive applications. The manufacturing process of burying PM inside the rotor is quite complex and also the shaft material needs to be non-ferromagnetic to avoid large flux penetration into the shaft (Madani, 2011).

2.5.3 Classification of PMSGs according to the rotor position

The rotor can surround the stator in outer rotor machines or be surrounded by the stator in the case of inner rotor machines, as shown in

Figure 2.14. Inner rotor machines are more present in the market, while outer rotor machines are mostly used with small HAWTs.

2.5.4 Maximum power point tracking

Variable speed wind turbines can adjust the generator speed to extract maximum power from the wind at different wind speeds. As shown in Figure 2.16, for each wind speed, there is a corresponding turbine speed at which the turbine power is at its maximum. The MPPT technique therefore consists on achieving maximum power extraction for each wind speed within a certain wind speed range in order to improve turbine efficiency. Several MPPT methods for PMSG based WECSs are discussed and compared by literature (Rekioua, 2014; Abdullah, et al., 2012; Heydari & Smedley, 2015; Wu, et al., 2011). Some of the most common are discussed below.

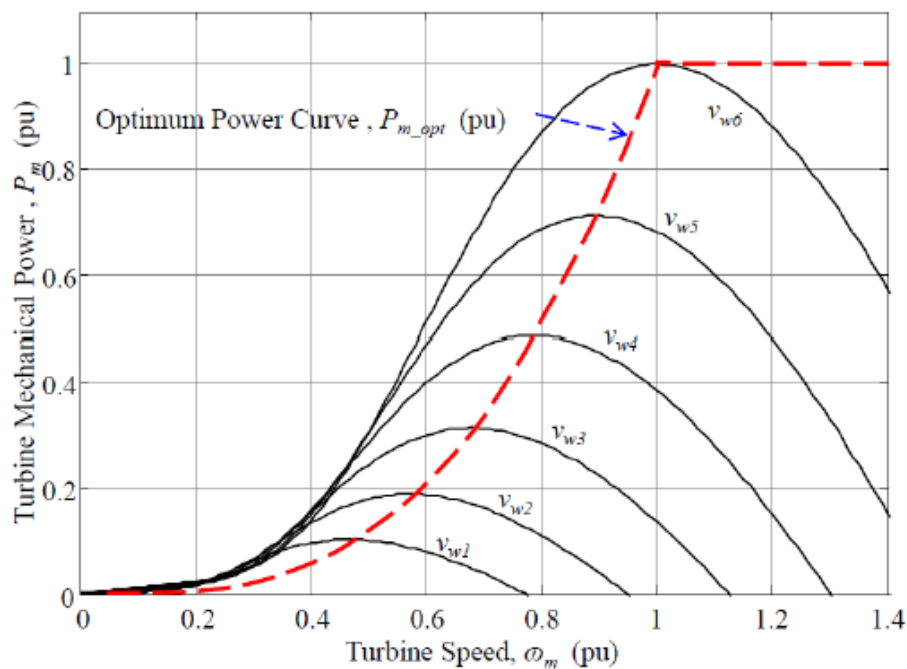


Figure 2.16: Typical MPPT curve for a power versus rotational speed turbine characteristics

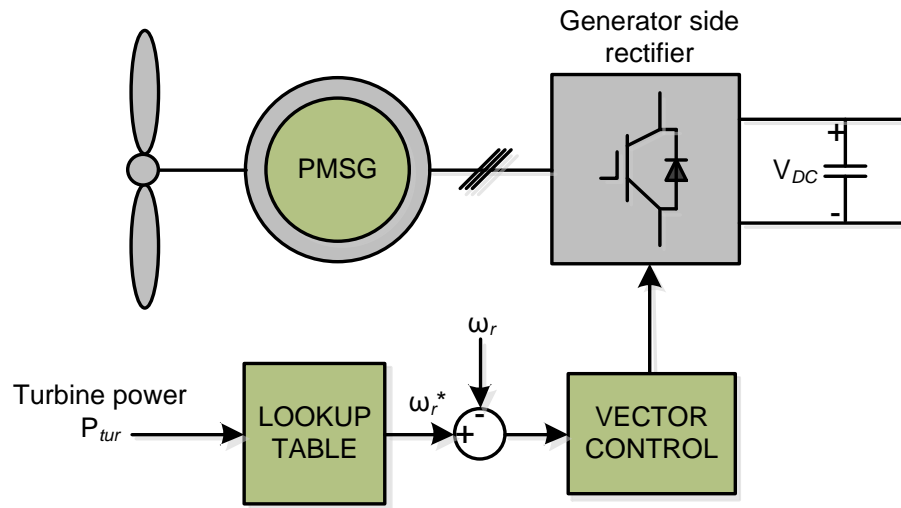


Figure 2.17: PSF method applied to a PMSG based WECS

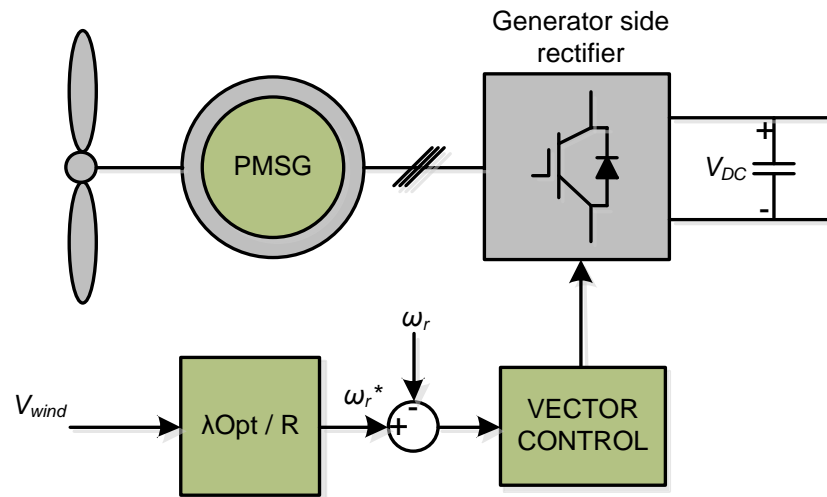


Figure 2.18: Optimal TSR method applied to a PMSG based WECS

2.5.4.1 Power signal feedback

This method uses a power versus wind speed curve to generate the reference turbine power which is compared to the actual power at measured wind speed. The error signal is compensated, and the actual power value will eventually equal the reference power at steady state. The power signal feedback method is illustrated in Figure 2.17. To express the maximum power-wind speed relationship, the following equation is used (Rekioua, 2014):

$$P_{m-\max} = -0.3 + 1.08V - 0.125V^2 + 0.842V^3 \quad \text{Equation 2.11}$$

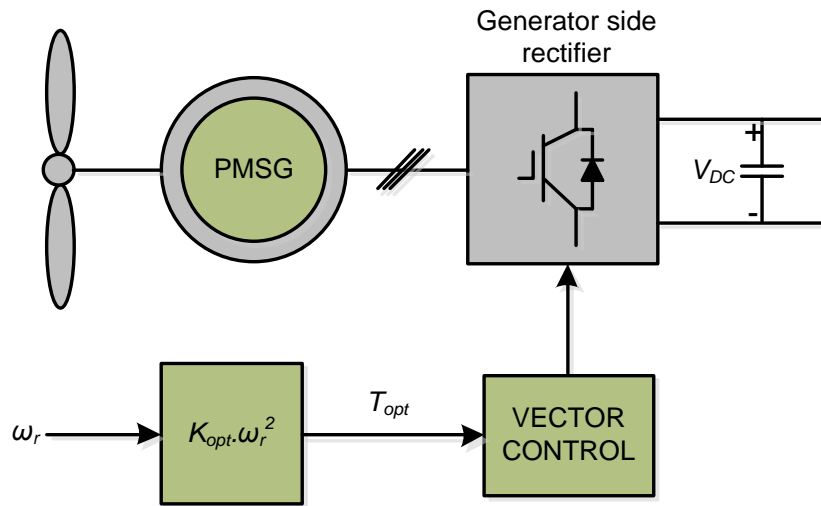


Figure 2.19: OTC method applied to a PMSG based WECS

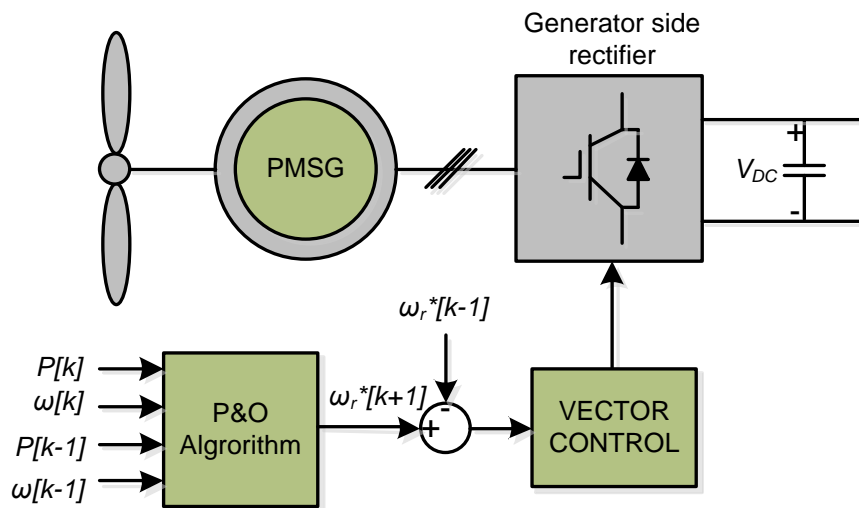


Figure 2.20: P & O method applied to a PMSG based WECS

2.5.4.2 Optimal tip speed ratio

From equation 2.10, it can be seen that the turbine power is a function of the tip speed ratio (TSR) λ , and the pitch angle β . Equation 2.9 also shows that the value of λ depends on the turbine speed ω and the wind speed V . Therefore, MPPT can be achieved by keeping the TSR at its optimal value such that the turbine speed and power are maximum at different wind speeds. This task can be completed in two different ways:

- Reference turbine speed is computed using measured wind speed and the optimal TSR. This reference speed is then compared to the actual speed which is then corrected, and the turbine operates at its MPP.
- The reference TSR is compared with its actual value, and the error signal is used to generate the reference turbine power.

The optimal tip speed ratio is illustrated in Figure 2.18.

2.5.4.3 Optimal torque control

In OTC reference torque is generated using the torque-speed quadratic relationship from the turbine power curve. OTC is illustrated in Figure 2.19. The maximum power coefficient C_{pmax} and the optimal TSR λ_{opt} must be known. The relationship between the torque and the speed can be expressed as (Heydari & Smedley, 2015):

$$T_{e-ref} = k_{opt} \omega_{opt}^2 \quad \text{Equation 2.12}$$

where

$$k_{opt} = \frac{0.5 \rho \pi r^5 C_{pmax}}{\lambda_{opt}^3} \quad \text{Equation 2.13}$$

2.5.4.4 Perturbation and observation (P & O) or Hill-climb searching (HCS)

As opposed to the other MPPT techniques mentioned above, The P & O is one method that does not require any information about the turbine power curve or the wind speed. Instead, an algorithm based on the principle of Hill-climb is used to determine and track the maximum operating point of the turbine's power curve as shown in Figure 2.20. A change in output power is first detected after a speed perturbation, then depending on the variation on the output power, the next speed perturbation is programmed. The P & O method is further elaborated in literature (Heydari & Smedley, 2015).

2.6 Power converters topologies for PMSG wind turbines

PECs play an important role in the performance of modern WTSs (Blaabjerg, et al., 2009). The PECs can be grid connected or standalone as used in most remote areas without grid interconnection (Prerna & Jagdeesh Kumar, 2013), unidirectional or bidirectional depending on the power flow (Khater & Omar, 2013), two-level or multilevel (Blaabjerg, et al., 2009). Power converters for WECS are widely discussed by many references (Yamarasu, et al., 2015; Wu, et al., 2011).

2.6.1 Thyristor grid-side inverter

The grid-side inverter uses thyristors to control the inverter's firing angle. This way the turbine speed is regulated through the DC link voltage, allowing maximum energy to be captured. The main advantage of this configuration is that it has a low cost for a high-power rating. However, there is a need for reactive power compensation, as well as total harmonic distortion reduction. Therefore, an active compensator filter is used, with a voltage source converter (VSC) as shown in Figure 2.21a. The Pulse width modulated (PWM) control is

driven by the error signal from the actual and the reference compensator current (Bisoyi, et al., 2013; Baroudi, et al., 2005).

2.6.2 Hard-switched grid-side inverter

2.6.2.1 The back-to-back PWM VSI

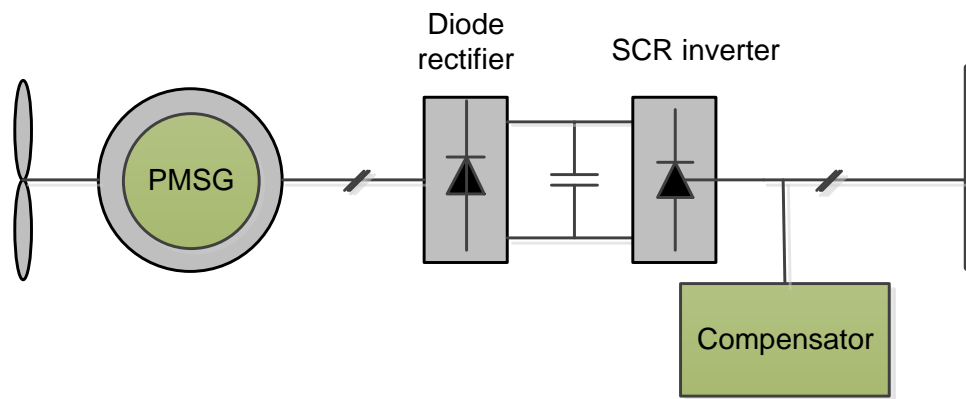
The back-to-back PWM VSI is the most common converter type using PMSG. This configuration consists of two VSI (one on the generator side, the other on the grid side) facing each other with an intermediate DC link (Khater & Omar, 2013). Each VSI is connected to a DC side and a 3 phase AC side as shown in Figure 2.21b and is composed of six semiconductor switches. The VSI also allows for bidirectional flow of power from machine side to grid side and vice versa. The machine-side converter generally controls the active power flow, while the grid-side converter controls the reactive power. A major advantage is that power factor is increased on the generator side with the aid of PWM modulation techniques, improving also the efficiency (de Freitas, et al., 2011). The main drawbacks of this configuration are the increased switching losses and harmonics (Prerna & Jagdeesh Kumar, 2013).

2.6.2.2 Generator Side Uncontrolled Rectifier with Boost Converter

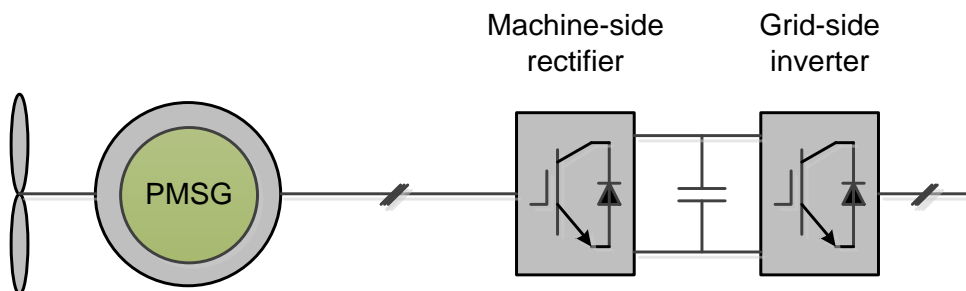
This topology comes as a substitute to the widely used diode rectifier with DC link capacitor and is shown in Figure 2.21c, which produces a lot of ripples at the output of the inverter. The main difference is that the short duration bulky DC link is replaced by a boost converter which is responsible for MPPT, thereby eliminating the need for an anemometer (Jamil, et al., 2012). The other advantage of this topology is that the controller adapts to changes in generator parameters (Jamil, et al., 2012; Prerna & Jagdeesh Kumar, 2013). However, the use of an additional switching stage implies an increase in cost as well as switching losses, and consequently an efficiency drop.

2.6.3 Multilevel converters

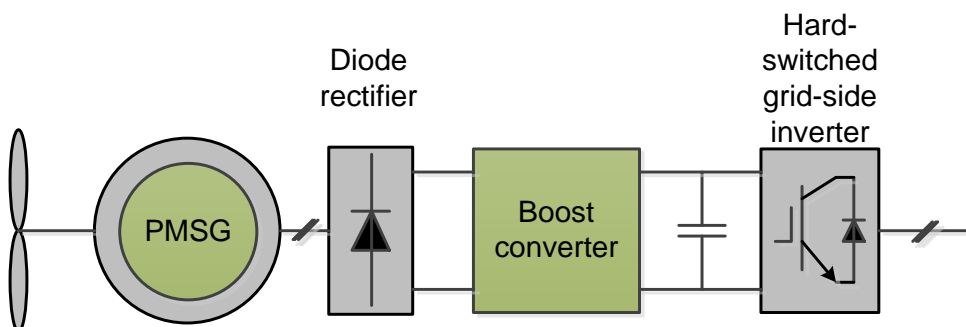
Multilevel converters are suitable for the integration of high-power wind generators, generally in the MW range (Debnath & Saeedifard, 2013). The converters have more than two voltage levels, reducing THD at the output compared to traditional back-to-back PWM converter. Switching losses are also reduced by approximately 25% (Kim & Lu, 2010). These converters are designed to handle high power/voltage levels using low rating devices (Debnath & Saeedifard, 2013). However, major drawbacks include the voltage imbalance caused by the DC link capacitor, uneven current distribution through the switches, increased cost due to the increased number of switches, and the complexity of the control (Kim & Lu, 2010).



a) PEC with SCR inverter



b) PEC using back-to-back hard switch configuration



c) Typical PEC using diode rectifier and intermediate boost converter

Figure 2.21: Examples of PECs used with PMSG based WECS

There are many multilevel converter topologies at this day (Kim & Lu, 2010), the most common being the neutral point clamped (NPC), the cascaded half-bridge (CHB), and the flying capacitors (FC). Of them all, the NPC is still the most appreciated and widely used (Kim & Lu, 2010).

2.6.4 Matrix converters

The matrix converter (MC) is a particular design that eliminates the DC stage from the traditional AC-DC-AC conversion process, to the profit of a direct AC-AC conversion. This arrangement has the advantage that the bulky DC link capacitors and/or inductors are inexistent, and so are the associated lifetime, size, and cost issues. The output voltage

magnitude, frequency, phase angle, as well as the input power factor are controlled independently, due to the large number of control levels that the MC provides. However, the main disadvantages of the MC are its complex control due to commutation problems, the scarcity of monolithic bi-directional switches, the lack of decoupling between the two AC sides of the converter, and the low voltage gain (Pandu Ranga & Vijaya, 2013; Yang & Li, 2009).

2.6.5 Z-source converters

Also called impedance source converters, z-source converters have been designed to overcome operating range limitations of both voltage source converters and current source converters. They use an X shaped impedance network to connect machine and grid side converters. They are widely discussed in literature (Peng, 2002; Vilathgamuwa, et al., 2008; Florescu, et al., 2010).

2.7 Power converter control

The control system, just as much as the hardware, plays an important role in the overall performance of a wind turbine system. The controller is designed for the wind turbine to reach specific objectives that can be summarized as follows (Soriano, et al., 2013):

- Extract maximum power from the wind
- Ensure maximum output power for different wind speeds
- Deliver quality power according to network provider standards
- Comply with grid interconnection requirements
- Reduce stress on mechanical components during turbulences

According to many references (Busca, et al., 2010; Quang & Dittrich, 2008; Allagui, et al., 2014; Jash, et al., 2013), vector control is the most popular and most widely used method for the control of PEC in a WTS. Comparisons of different vector control techniques were done by different authors with emphasis on the FOC (Field Oriented Control) and DTC (Direct Torque Control) on the generator side (Busca, et al., 2010; Allagui, et al., 2014; Huang, 2013), and VOC (Voltage Oriented Control) and DPC (Direct Power Control) on the grid side (Huang, 2013; Allagui, et al., 2014).

The FOC technique seems to be more attracting than the DTC for direct-drive applications since it presents a good performance at relatively low speeds, offers quick speed and torque responses, as well as reduced torque ripples and minimal power-tracking error. On the other hand, DTC is easier to implement than FOC and offers fast transient response, but presents drawbacks such as difficulties in torque control, increased ripples and noise level, which are even more pronounced at very low speeds. On the grid side, both strategies present similar

results and they both meet grid code requirements. However, VOC presents lower THD and higher efficiency while DPC provides a better dynamic response.

As far as modulation techniques are concerned, space vector modulation (SVM) techniques are mostly employed (Freire, 2013). Other techniques use a carrier signal that is compared to a reference modulation signal, or hysteresis current control (Wu, et al., 2011; Zeng & Chang, 2005). Comparisons of some of these techniques shows that SVM applied with pulse width modulation present a better steady state performance under normal operations or during grid faults, while HCC presents better results for faults on the generator side (Freire, 2013). When SVM is used with DTC, the results are similar to the FOC technique (Busca, et al., 2010).

2.8 Summary of the chapter:

In this section, an overview of already available and most common wind turbine technologies was presented. The fundamentals of a wind energy conversion system were first discussed, including the different components of a wind turbine, as well as its aerodynamics principles and the different maximum power extraction methods. The different generator, power electronics converters, and drive train topologies of the main wind turbine concepts from fixed speed to variable speed were also discussed and compared. The direct driven PMSG full scale variable speed topology was proven to be a better option compared to other concepts due to many reasons such as an increased generator efficiency, the absence of gearbox, and more flexible controllability due to the bidirectional nature of the converters. Finally, the different PECs and control techniques were also discussed and compared.

CHAPTER THREE

GRID CODE REQUIREMENTS AND LVRT SOLUTIONS

Introduction

Grid codes are important to ensure a safe and reliable transmission of electric power within the interconnected network. They represent a guideline defined by each transmission system operator (TSO) to which each power producer must adhere in order to be connected to the grid. In South Africa, electric power is generated from various sources including coal, gas, water, and renewables. In this chapter, a review the grid code requirements for wind power plants connected to the electric power network is presented and the case of South Africa is analysed in more details. Low voltage ride-through being the core of this research, a review of the different LVRT solutions for a PMSG based wind energy conversion system is also presented.

3.1 Grid code requirements for wind farms

Grid power quality and network stability are major challenges issued from the massive integration of large-scale high-power wind turbines into the grid. As such, wind turbine operators have developed new grid code requirements that WTSs and WPPs need to satisfy when connected to the network. These important requirements are usually classified into four categories namely active power control, reactive power and voltage control, frequency and voltage operating range, and fault ride-through capability with following objectives: (Sourkounis & Tourou, 2013)

- Control the active power supplied to the grid during frequency and voltage disturbances
- Define appropriate ranges of frequency and voltage and ensure WPPs operation within the specified limits
- Contribute to the grid power balance by injecting or absorbing reactive power.
- Support voltage recovery at connection point after fault occurrence
- Maintain smooth connection to the network in the event of small duration voltage dips

Because transmission systems differ due to different standards, most grid code requirements also present different tolerance, limitation and operating values. Grid code requirements of many countries are reviewed and compared in literature (Tsili, et al., 2009; Mohseni & Islam, 2011).

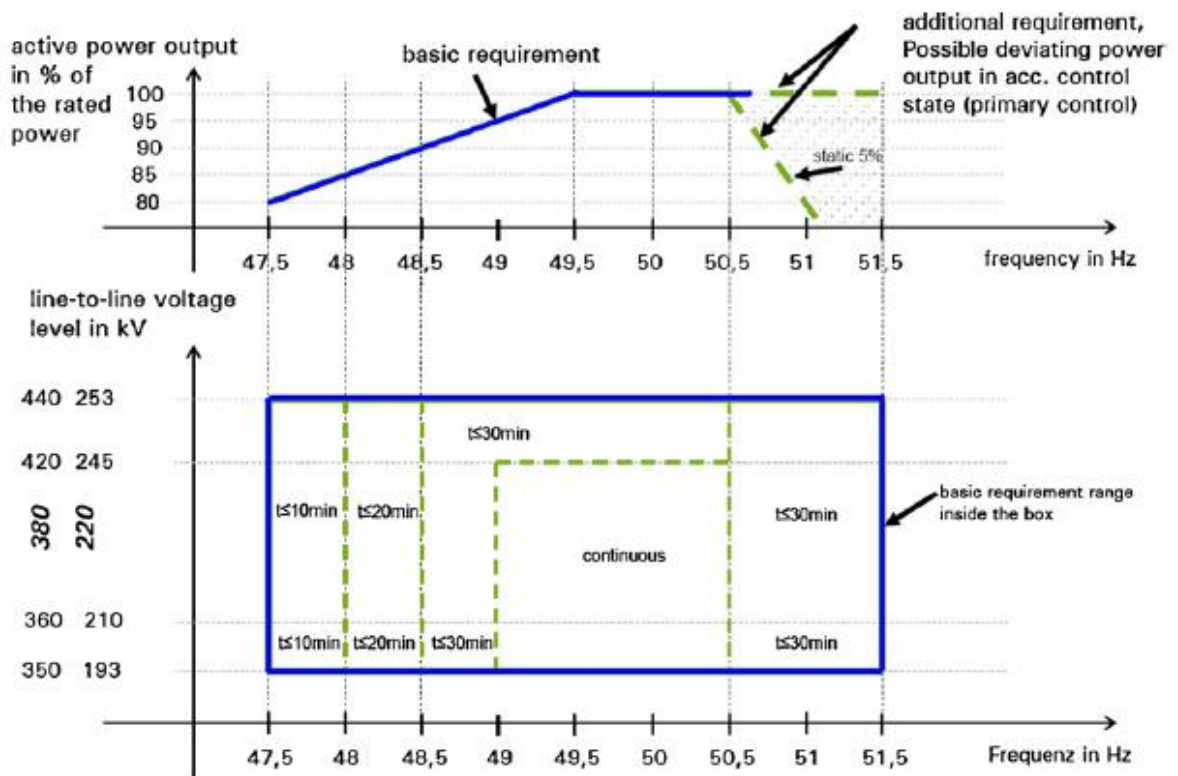
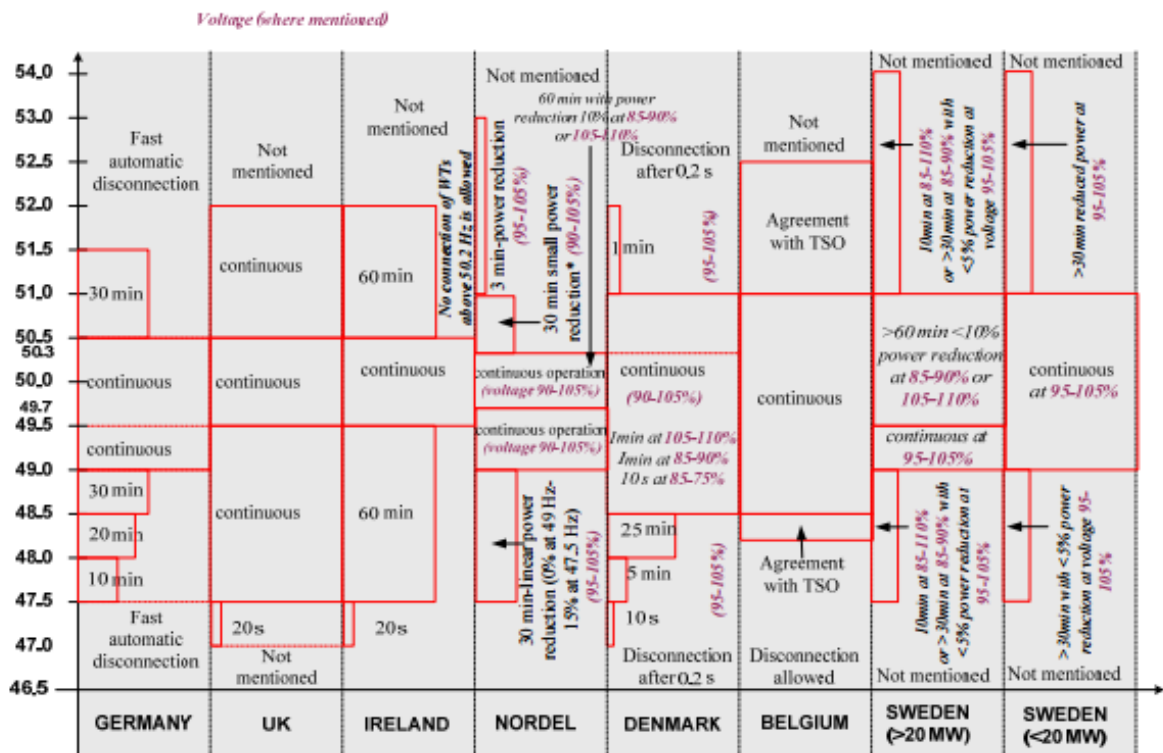
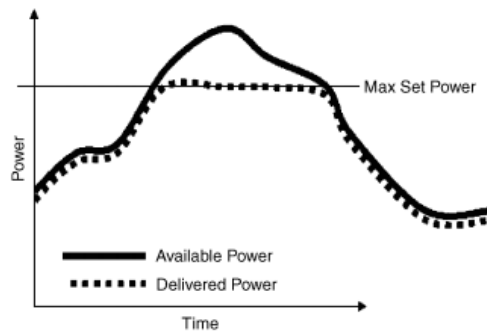


Figure 3.1: Voltage and frequency operating ranges as defined by German power system operator (Mohseni & Islam, 2012)

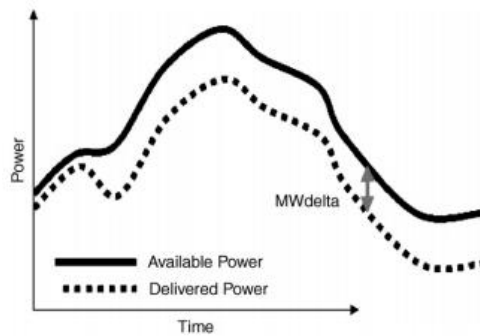


* the total duration of these operating conditions must not exceed 10 hours/year

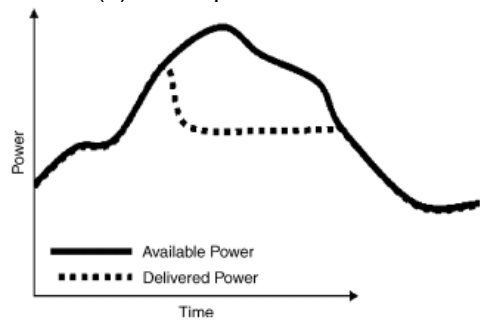
Figure 3.2: Frequency operating limits in some of the European countries



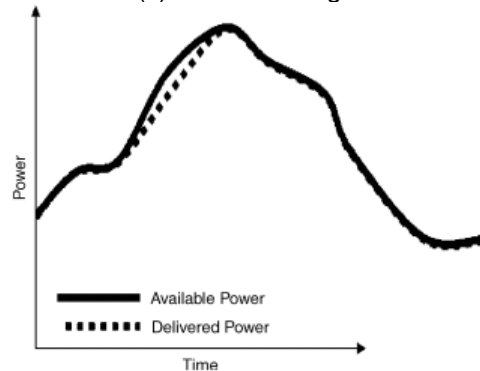
(a) Absolute power constraint



(b) Delta production constraint



(c) Balanced regulation



(d) Power gradient constraint

Figure 3.3: Active power regulation strategies (de Alegria, et al., 2007)

3.1.1 Frequency and voltage operating range

Many grid codes have voltage and frequency variation ranges or limits within which wind farms are expected to carry on a smooth and continuous operation even during small disturbances (Sourkounis & Tourou, 2013; Tsili, et al., 2009). Past these limits specified by system operators, system stability is no longer guaranteed, and wind farms and the rest of

the power system may be endangered. In this case, disconnection of WPPs seems to be the most appropriate option.

A graphical representation of voltage and frequency operating ranges as defined by general grid codes is illustrated in Figure 3.1. Generally, WPPs operate continuously at frequencies equal to or very close to the nominal value and do only operate for minor time durations when frequencies exceed certain values as illustrated in Figure 3.2.

3.1.2 Active power control

Large positive or negative differences between actual and nominal frequency values usually indicate a power system imbalance. Frequency changes could be caused either by a fault on the network, or by acute wind speed variations. In response to these instabilities and to reinstate close to nominal frequency, grid codes require that WPPs have the capability to provide network frequency supports through the control of their generated active power.

WPPs should be capable of reducing or regulating their output power to a predefined magnitude, whenever requested from the system operator. This may be achieved by minimizing the extracted wind power using a pitch angle control on the turbine blades in as explained earlier in section 2.3.3 (Sourkounis & Tourou, 2013; Tsili, et al., 2009). Figure 3.1 shows a typical curve of output power variation in response to frequency changes. The curve shows that the output power will gradually decrease as the frequency increases above nominal value. It is important to note that the output power delivered is slightly lower than the maximum achievable level. This is to allow the output power to increase up to its maximum value, such that the frequency can be sustained when its value falls below nominal value (de Alegria, et al., 2007).

It is also important that active power be reduced or restored at a satisfactory rate when a voltage dip occurs or is cleared, to avoid generator over-speeding or power surges which could result in damage of wind generator and power system disturbances. Active power production is managed using different strategies in order to fulfil all of the above-mentioned frequency and voltage requirements. Some of the most common are listed below and presented in Figure 3.1 (Mohseni & Islam, 2012):

- The active power can be controlled so that its value can never exceed a pre-set maximum value regardless of whether more wind power is available or not. This regulation mode is known as active power constraint. Generally, when wind power production is greater than the demand, wind turbine operators usually lose money since they are required to pay for excess production.

- The power output is maintained at a slightly lower level to allow frequency control as explained above and achieve delta production constraint.
- The active power supplied to the grid is controlled such that it can be quickly reduced on fault occurrence or increased at fault clearance to ensure balanced power production and consumption. This control is therefore named balanced regulation.
- The power gradient constraint is used to regulate the rate at which WPP power is supplied to the grid to the level of conventional power plants by setting a maximum gradient that cannot be exceeded.

3.1.3 Reactive power and voltage control

The purpose of the reactive power and voltage control requirement is to ensure that system operation under required limits is properly achieved, reducing risks of network instabilities. Wind farms should have reactive power control capability for the purpose of supporting the voltage at the PCC (point of common coupling), as well as the reactive power demand from the grid (Sourkounis & Tourou, 2013). This means that WPPs should be able to supply lagging or leading reactive power depending on whether power is supplied to or absorbed from the PCC, while keeping the power factor within an acceptable range as illustrated in Figure 3.6. In some grid codes, the network operator should set a particular reference value for the reactive power at the wind farm connection point (Tsili, et al., 2009). Figure 3.6 shows the graphs of the requirement of reactive power variation with respect to changes in voltage for the case of Germany (Mohseni & Islam, 2012; de Alegria, et al., 2007).

3.1.4 Low Voltage Ride Through capability

New grid codes specifications require that wind farms be able to survive voltage faults up to a certain percentage of the nominal voltage, and for a precise time interval, while remaining coupled to the power system. In addition, active and reactive power should quickly ramp back to nominal value after fault clearance. This requirement is essential for a smooth and continuous supply from the power system by avoiding possible disconnection which could lead to further losses of generation capacity, and eventual collapse of the network (Sourkounis & Tourou, 2013; Tsili, et al., 2009).

The LVRT requirement is expressed using a voltage vs time characteristic curve which delineates the region under which the wind turbine should safely operate in the event of a grid fault (Leao, et al., 2010). An example of such curve is shown in Figure 3.6. Wind turbines should remain connected as long as the voltage at point of common coupling (PCC) is above delineated region, otherwise disconnection is allowed.

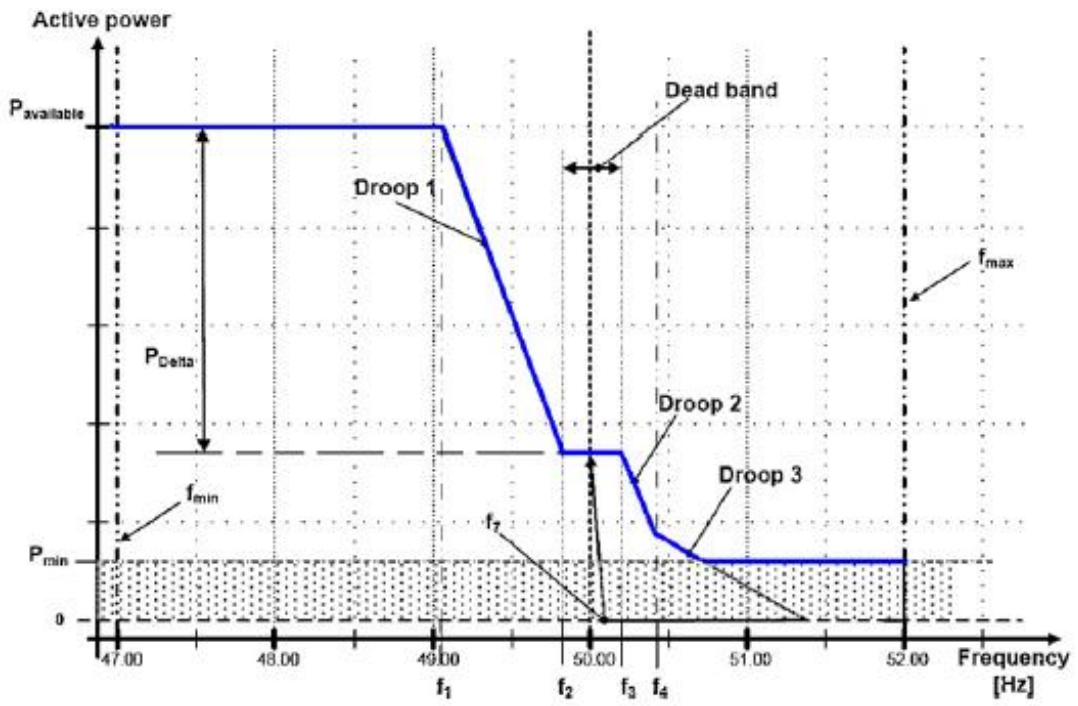


Figure 3.4: Power-frequency response curve by Danish grid code (Mohseni & Islam, 2012)

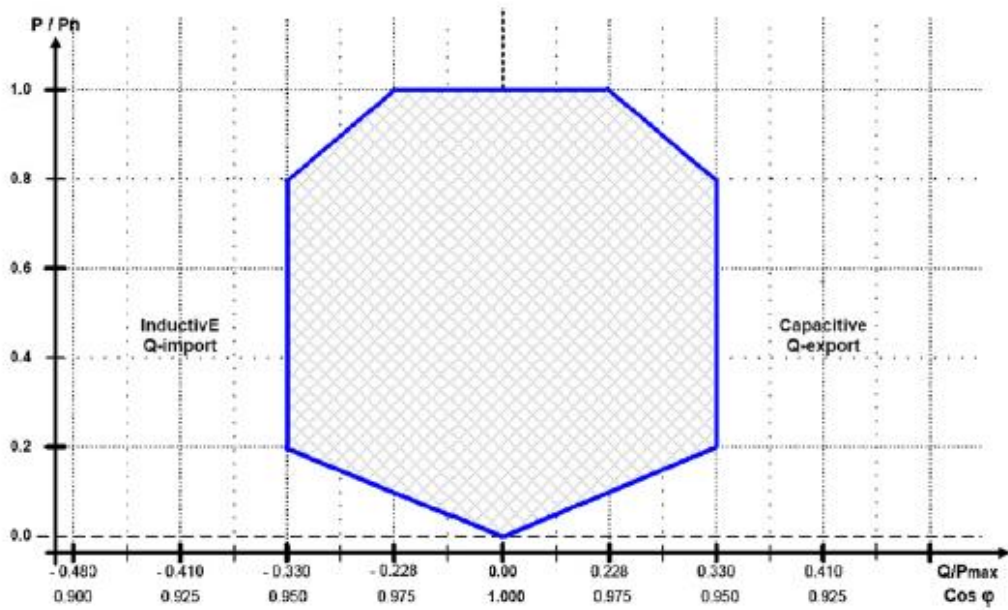


Figure 3.5: Reactive power and power factor requirement as enforced by Danish grid code (Mohseni & Islam, 2012)

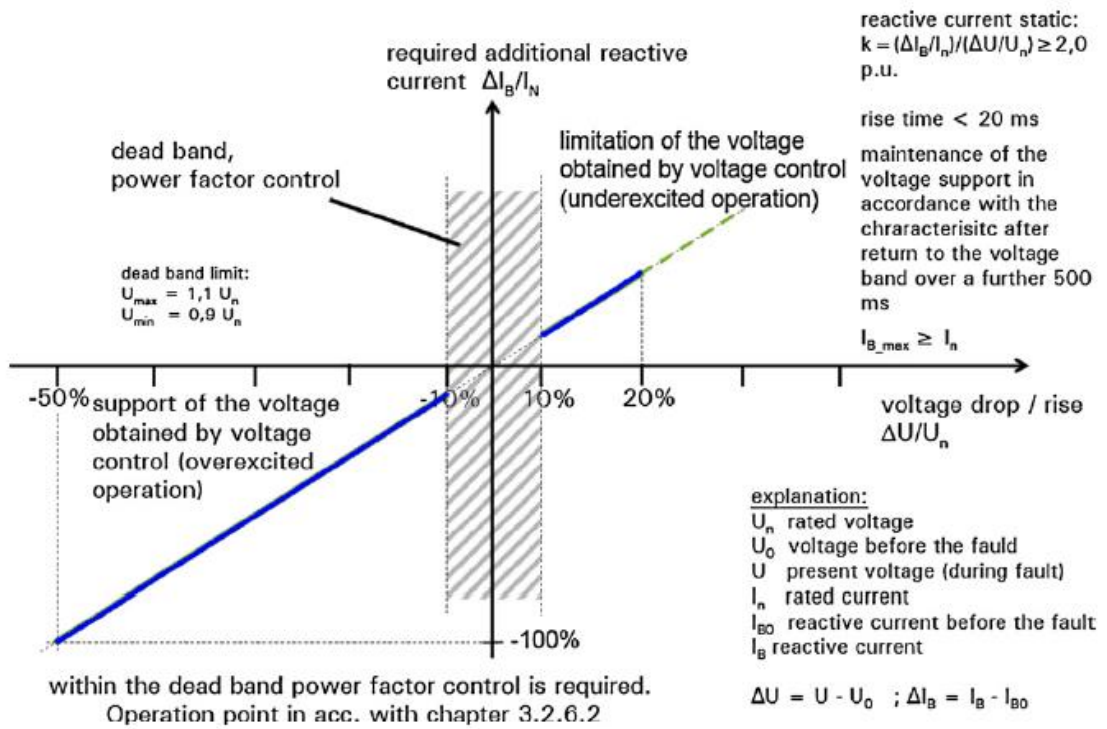


Figure 3.6: Reactive power support requirement as defined by German grid code (Mohseni & Islam, 2012)

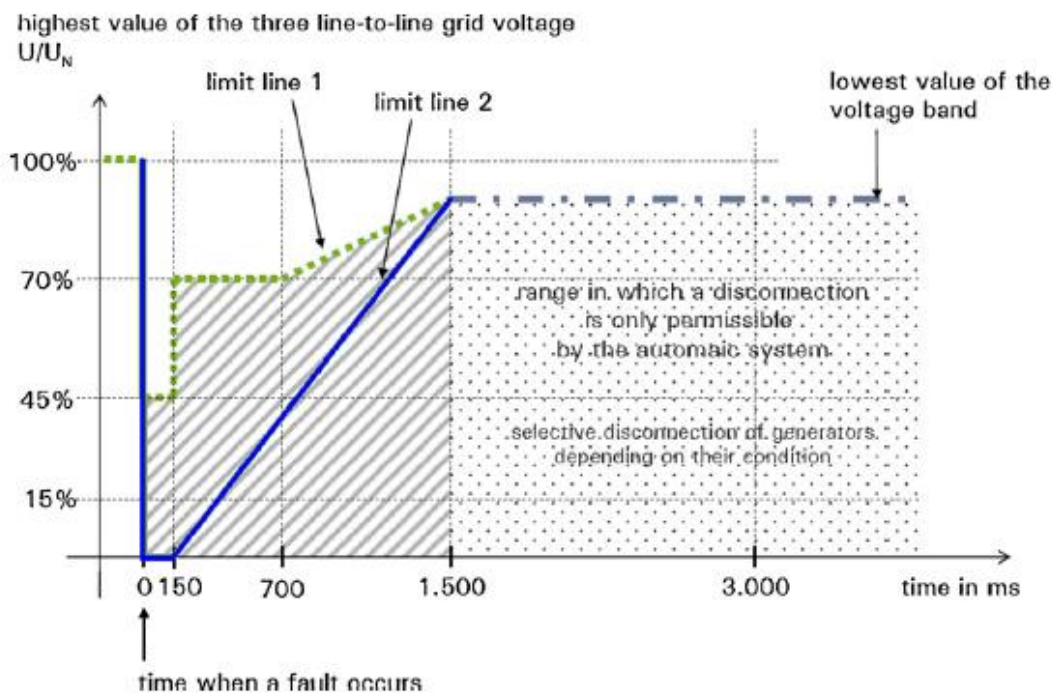


Figure 3.7: German LVRT requirement (Mohseni & Islam, 2012)

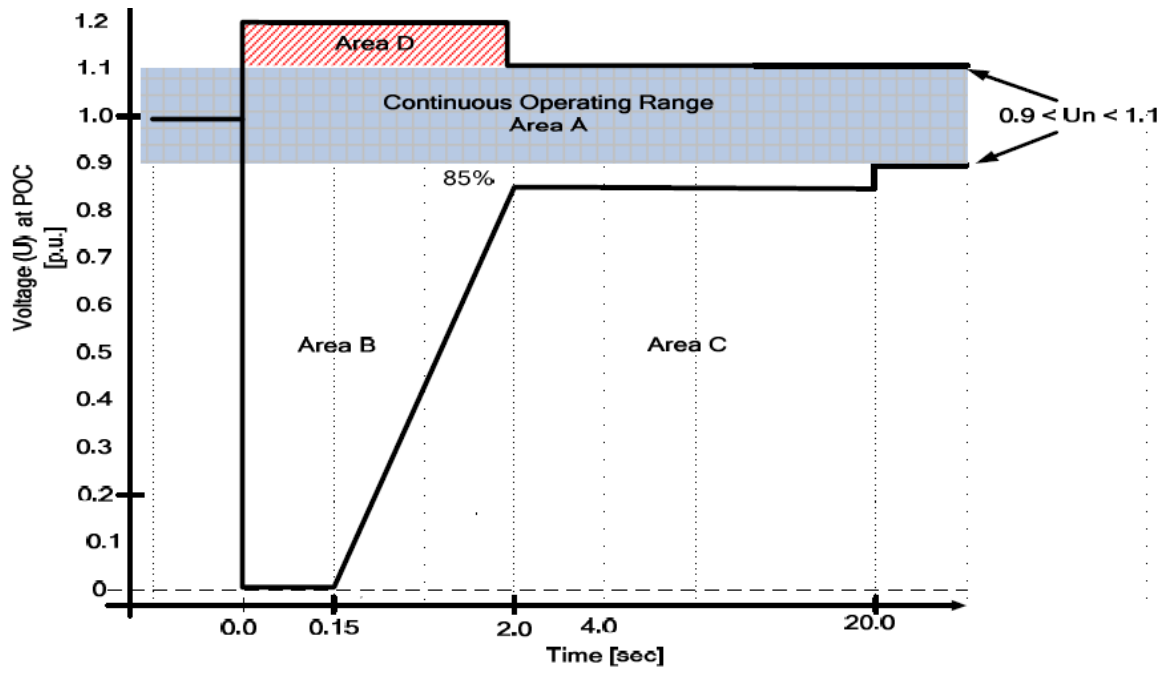


Figure 3.8: South African LVRT curve (Mchunu & Khoza, 2013)

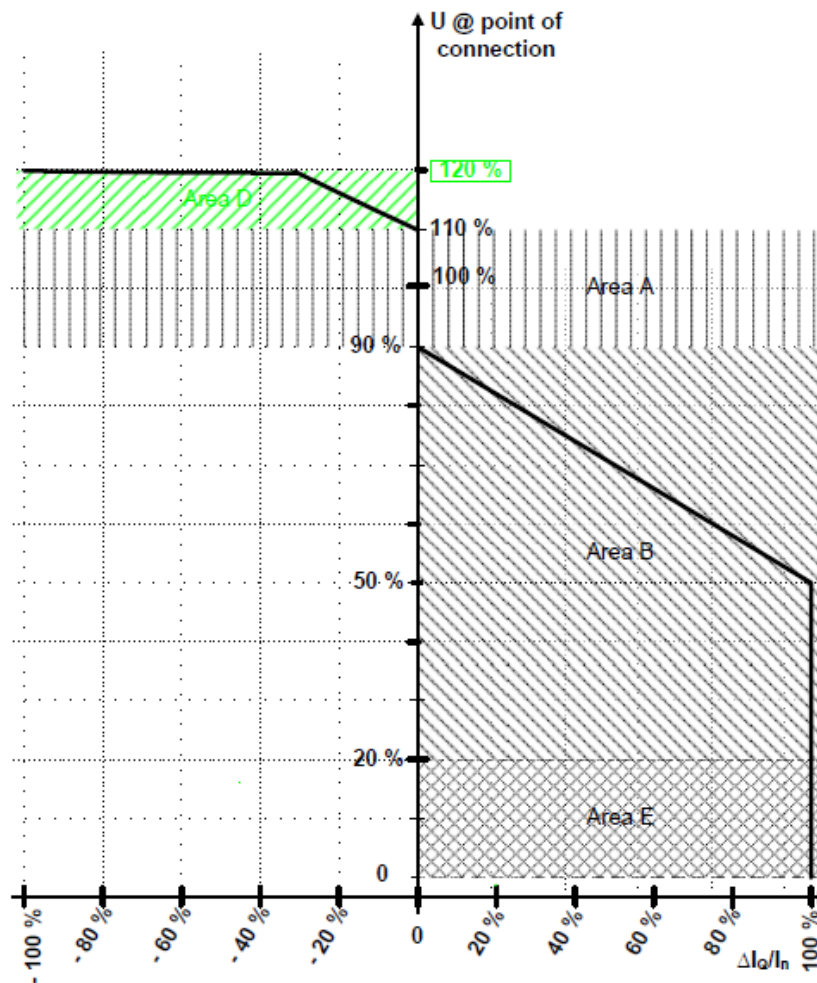


Figure 3.9: Requirement for reactive power support during grid fault according to the South African grid code (Mchunu & Khoza, 2013)

Table 3.1: Classification of RPPs according their rated power (Mchunu & Khoza, 2013)

Sub-categories	Rated power range (kVA)
A1	$0 < A1 \leq 13.8 \text{ kVA}$
A2	$13.8 \text{ kVA} < A2 < 100 \text{ kVA}$
A3	$100 \text{ kVA} \leq A3 < 1\text{MVA}$
B	$1 \text{ MVA} \leq B < 20 \text{ MVA}$
C	$\geq 20 \text{ MVA}$

For a wind turbine to successfully achieve the FRT, grid code requirements as well as wind turbine requirements should be met whenever a fault occurs in the grid. Therefore, on the grid side, wind turbines should be able to remain connected according to the FRT curve, supply reactive power to the grid, and recover active power. On the generator side, excess current and voltage on the stator or rotor, torque ripples, changes in turbine's speed, overvoltage on the dc-link should be avoided (Hu, et al., 2010).

3.1.5 South African grid code requirements for Renewable Power Plants

The South African grid code for renewable power plants (RPPs) was established by the National Energy Regulator of South Africa (NERSA) aiming for reliability, safety and security of the interconnected power system. This code ensures that RPPs connected or still to be connected to the power network meet specific technical and design requirements (Mchunu & Khoza, 2013). These requirements are defined according to different categories from A to C, depending on the power rating of the RPP as specified in Table 3.1.

With the South African grid code for RPPs, the same requirements listed earlier are also applicable. RPPs should be capable of operating within a certain limit of frequencies and voltages as well as contributing to network stability under faulty circumstances. The South African grid code requirements are presented by Mchunu & Khoza (2013). However, only the LVRT requirement is covered.

During voltage sags arising from symmetrical or unsymmetrical faults, RPPs should remain connected to the grid as shown in Figure 3.8. The FRT curve is divided into 4 sections each representing different operating regions for the RPPs.

- Area A: continuous operating region where the RPP should maintain normal production. This region is comprised between 0.9 and 1.1 pu, approximately $\pm 10\%$ of the rated voltage at the POC.
- Area B: faulty region for which the RPP is required to remain stable and connected to the network. In this operating mode, active power must be maintained for voltage drops up to 85% of rated value, otherwise reduction is required proportionally to the voltage

drop. The reduced active power is expected to recover within 1 second to at least 90% of pre-fault value. Voltage drops up to zero should be tolerated for maximum fault clearance duration of 150 millisecond. Moreover, the RPP should contribute to voltage stabilization by injecting reactive power as illustrated in Figure 3.9.

- Area C: the RPP may be disconnected from the network.
- Area D: the nominal voltage at POC can reach peaks of up to 120% without disconnection of the RPP for duration not exceeding 2 seconds. This area is only applicable to RPPs of category C.

3.2 LVRT methods for PMSG WTs

In a full-scale variable speed WT, the generator side and the grid side are decoupled by the PEC. During a fault at the PCC, the terminal voltage is considerably reduced, which implies that the active power supplied to the grid is also reduced. On the other side, the generator keeps on supplying power since not directly connected to the grid. This excess power is stored in the dc-link and will later lead to dc-link over-voltage and voltage oscillation which could affect steady state operation of the generator and cause damages to the converter and the WTS (Dong, et al., 2012). In order to avoid this situation, a number of techniques have been proposed by different references.

Nasiri et al (2015) present a review and comparison of some of the most popular LVRT techniques used with PMSG WECSs. The paper classifies these techniques into two categories depending on whether additional devices are used or not in order to achieve LVRT as presented in figure 3.10. In the second case, the LVRT is achieved by simply modifying control strategy, without the need for external action. These techniques are referred to as “modified control-based methods”. Some of the most used LVRT techniques are discussed below.

3.2.1 Modified control-based techniques

3.2.1.1 Change of control strategy

The control of the DC-link voltage is achieved by the MSC, while the active and reactive power control task is done by the GSC, as opposed to the traditional control in which the GSC is responsible for DC-link voltage control and active power is controlled on the machine side. In this method, the DC-link voltage regulation is accomplished by decreasing the generator stator current and thus the power flow to the DC-link. The excess energy is converted to rotational energy, increasing the turbine’s rotational speed which is directly pitch controlled if the speed exceeds the rated value. An external damping controller is also used in this system (Hansen & Michalke, 2009).

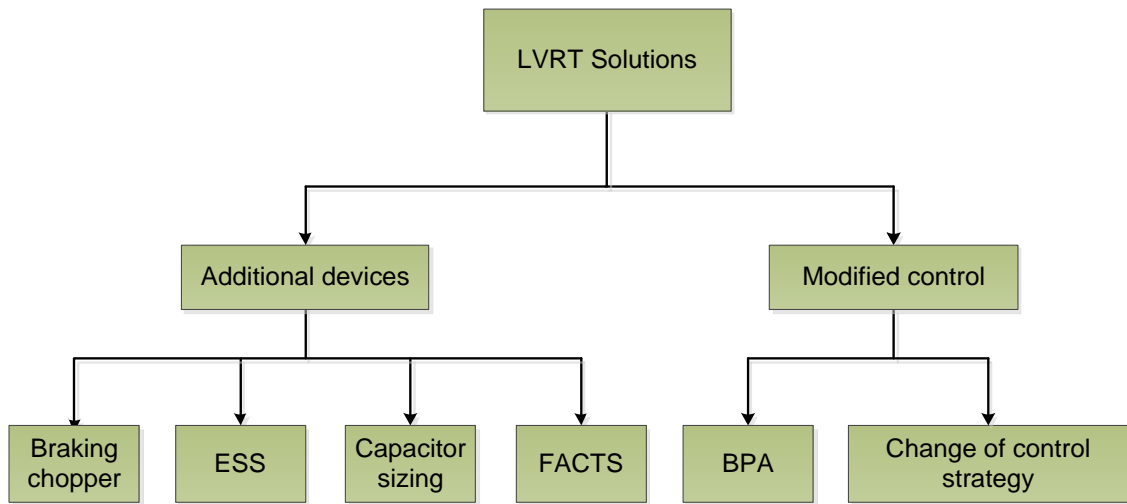


Figure 3.10: LVRT enhancement techniques

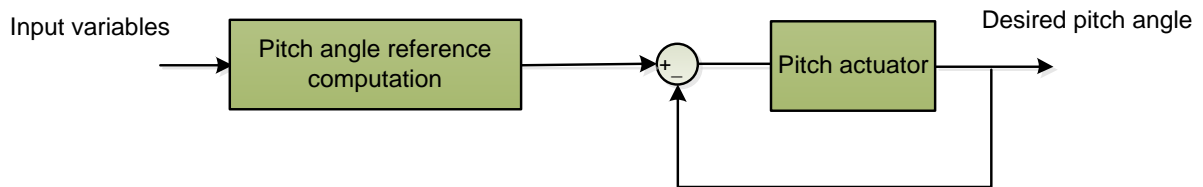


Figure 3.11: Block diagram of a typical BPA controller

3.2.1.2 Blade pitch angle (BPA) control

Apart from being used for maximum wind energy extraction at low wind speeds or for minimum extraction at more than rated wind speeds, BPA control is also used for LVRT (Conroy & Watson, 2007; Yang, et al., 2009). In this case, the aim of the pitch controller is to reduce the energy captured by the turbine blades during a grid fault, by pitching out of the direction of the wind. This technique is simple and cheap but offers a slow response due to its mechanical nature. Therefore, the BPA control is usually used in addition to other fast LVRT techniques to improve the system's response.

BPA control techniques are usually closed loop systems where the actual measured pitch angle is compared to a reference value which can be controlled either from wind speed, generator speed or torque, and power measurements (Ben Smida & Sakly, 2015) as illustrated in figure 1. In Conroy & Watson (2007), during a grid fault condition, the controller switches from the normal operating mode to an emergency mode and the reference pitch angle is specified by its emergency value. For Nasiri, et al., (2015), the control in figure 3.11 above is used when wind speeds exceed nominal value, while grid voltage differences are used to generate the reference pitch angle in the event of a fault (Nasiri, et al., 2015).

3.2.2 Additional devices-based techniques

3.2.2.1 Capacitor sizing

Storing the excess energy from the generator into another capacitor of larger size is an alternative way of decreasing the energy to be absorbed by the dc-link capacitor during a voltage dip. Since the required capacitor power increases with the duration of the voltage dip, longer voltage dips will imply larger capacitor sizes. Capacitor sizing is therefore an inappropriate method and is usually not used (Conroy & Watson, 2007).

3.2.2.2 Braking resistor (DC chopper)

A DC chopper circuit which consists of a braking resistor controlled by a switch is connected in parallel with the DC-link capacitor as shown in Figure 3.12. Whenever the dc-link voltage exceeds a predefined value, the switch is activated and the excess energy is dissipated through the resistor (Rosyadi, et al., 2011). This method can also be combined to the pitch control technique for a more effective result especially for longer voltage dips, reducing the rating of the protective resistor and thus the overall cost (Ibrahim, et al., 2012).

Qiu, et al., (2011) and Kesraoui, et al., (2010) used a bypass chopper with the diode rectifier configuration to dissipate the excess power. The error signal from the DC-link voltage reference and measured values is sent through a PI regulator to control the duty cycle of the switch. For Shuju, et al., (2008) the generated power, the grid power and the DC-link voltage measurements are used to determine the state of the switch and to calculate its duty cycle. For Yan, et al., (2011), a signal is sent to the controller at the occurrence of a grid fault, and the IGBT switch is directly triggered and remains on until fault clearance. Heng, et al., (2008) used a D flip-flop to generate the switching command to the switch. A predefined threshold value is compared to the actual DC-link value using a comparator circuit. The input to the flip-flop is the output from the comparator.

3.2.2.3 Energy storage system

An Energy storage system (ESS) is also used to store the excess energy from the generator or to supply power to the grid if necessary (Nguyen & Lee, 2010). This method also improves power quality on the grid by charging or discharging the fluctuating power component that derives from changes in wind speed. Lead acid batteries (LAB), sodium sulphur batteries (SSB), and vanadium redox flow batteries are mostly used due to their lifespan, their storage capacity, low cost and quick dynamic response. However, an additional dc-dc converter is required in order to regulate the excess voltage to the battery rating (Ibrahim, et al., 2012; Nasiri, et al., 2015). A typical WECS equipped with an ESS is shown in Figure 3.12.

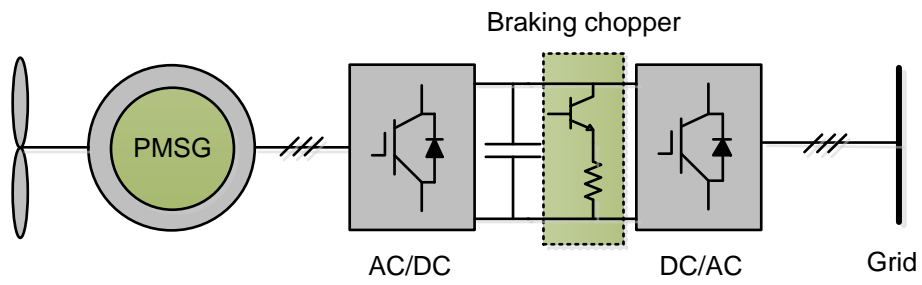


Figure 3.12: Braking chopper configuration

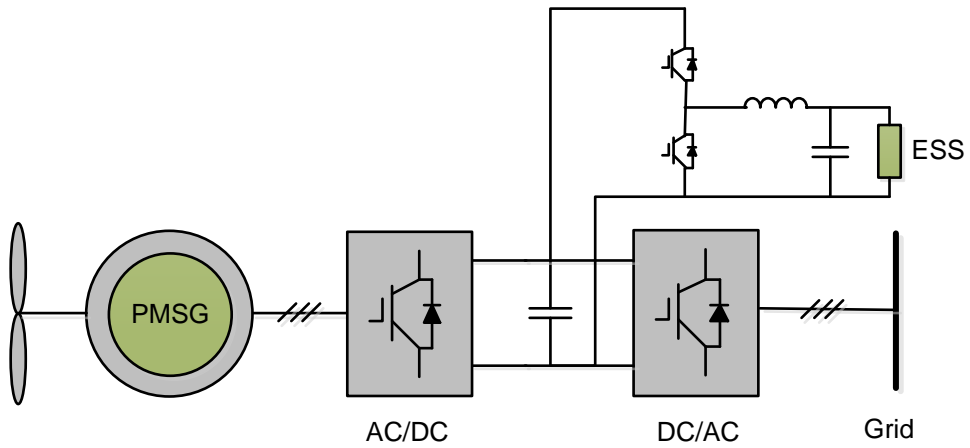


Figure 3.13: Energy storage system connected to the DC-link

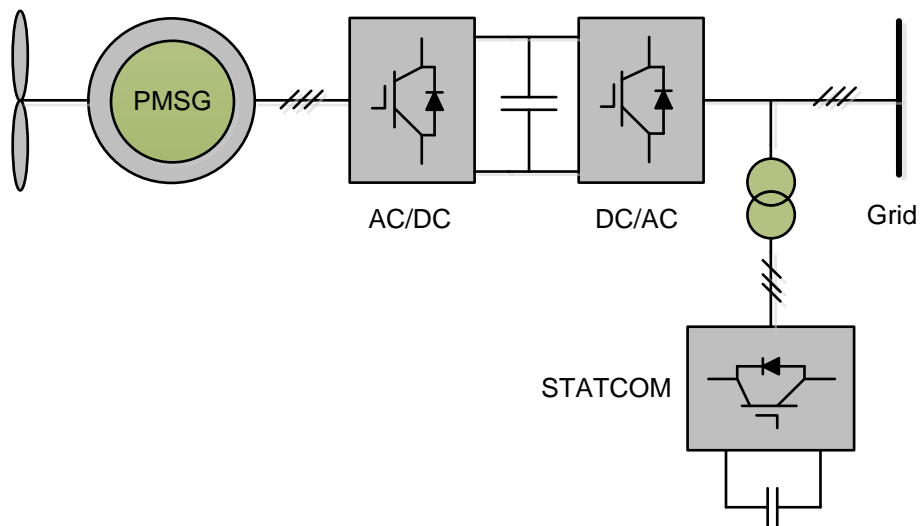


Figure 3.14: Typical structure of a STATCOM

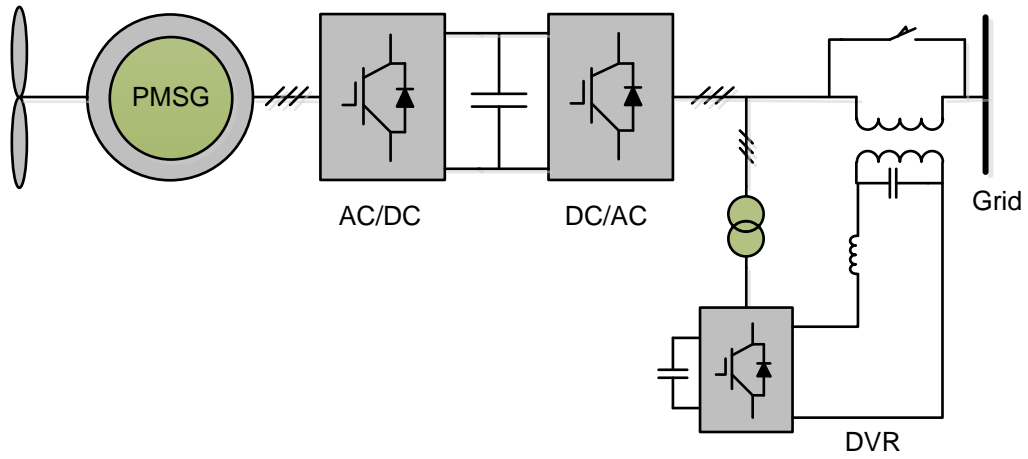


Figure 3.15: Typical configuration of a dynamic voltage restorer

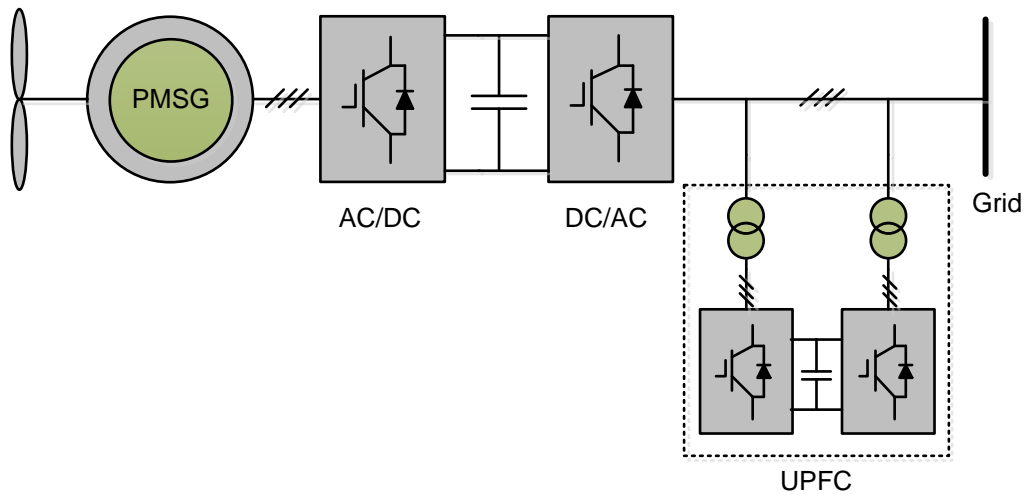


Figure 3.16: Typical configuration of a unified power flow controller

3.2.2.4 The use of FACTS devices

Facts (Flexible AC transmission systems) devices have the advantage that they can supply reactive power to the grid. They can be connected in parallel (shunt connection), series (series connection), or in a combination of series and parallel (Hybrid connection) with the common coupling point. In shunt connection, the amount of reactive power injected on the grid depends on the reactive power demand from the grid during a grid fault, as well as the reactive power transfer capability from the wind farm. The two main shunt compensation devices are the Static Synchronous Compensator (STATCOM) and the Static VAR compensator (SVC). Although these techniques are mostly used with DFIGs, they can also be used with PMSG based wind turbines (Chowdhury, et al., 2012; Nguyen & Lee, 2013). The basic configurations of STATCOM is shown in Figure 3.12.

Series connection devices inject capacitive voltage at the PCC to increase the reactive power supply from the grid. These devices include the thyristor-controlled series capacitor

(TCSC), Static Synchronous Series Compensator (SSSC), the Dynamic Voltage Restorer (DVR), the Magnetic Energy Recovery Switch (MERS), and more (Wenming, et al., 2011; Ibrahim, et al., 2012). The configuration of a DVR is shown in Figure 3.12.

As for the hybrid connection, the Unified power flow controller (UPFC) is the state-of-the-art of this technology. UPFCs have the advantage that they can inject capacitive voltage for voltage recovery from the series connection, as well as reactive power for grid support from the shunt connection (Raphael & Massoud, 2011). The UPFC is typically a back-to-back connection of STATCOM and SSSC as illustrated in Figure 3.12.

Summary of the chapter

This chapter presented an overview of the existing grid code requirements to be met for WPPs to be connected to transmission and distribution networks in some developed countries. Frequency and voltage range, active power control, reactive power and voltage control, and FRT capability were depicted as the most commonly used by many grid operators. These requirements were detailed and explained thoroughly. The case of FRT and particularly the LVRT of the South African grid code was more deeply examined.

An overview of LVRT enhancement solutions was also presented in this chapter. These solutions were categorised into two depending on whether additional components were needed or not. The advantages and disadvantages were presented, and the solutions were compared.

CHAPTER FOUR

WIND TURBINE SYSTEM MODELING

Introduction

Before carrying out any simulation studies on the WECS, a detailed model of the different components that constitute the system needs to be implemented. This chapter discusses the mathematical modeling of the full scale variable speed WECS including all controllers. The WECS consists of a direct-driven PMSG wind turbine connected to the grid through a back-to-back converter. The advantages and drawbacks of this configuration are already presented in section 2.4. A WECS equipped with PMSG and full scale power converter is represented in

Figure 1.1. As illustrated, the WTS is composed of a mechanical part which converts the energy from the wind into mechanical rotational energy through the turbine blades and the drive train, as well as an electrical part (PMSG, PEC, filters, transformers) which converts the mechanical energy from the drive train to quality electrical power to be fed into the grid (Kasem Alaboudy, et al., 2013).

To accurately emulate the dynamic behaviour of the wind turbine and its impacts when connected to a power system, different key components such as the turbine and mechanical shaft dynamics, generator electrical and mechanical characteristics, power converter controls, protection settings and measurements of critical variables, need to be taken into consideration in the mathematical model for time domain simulations (Vittal & Ayyanar, 2013).

4.1 Wind turbine model

The power extracted by the turbine was expressed in Equation 2.10 of chapter 2. The power coefficient $C_p(\lambda, \beta)$ was modelled using the following equation (Heir, 2014):

$$C_p(\lambda, \beta) = 0.5176(116/\lambda_i - 0.4\beta - 5)e^{-21/\lambda_i} + 0.0068\lambda \quad \text{Equation 4.1}$$

with

$$\frac{1}{\lambda_i} = \frac{1}{\lambda + 0.08\beta} - \frac{0.035}{\beta^3 + 1} \quad \text{Equation 4.2}$$

Figure 4.2 represents typical $C_p(\lambda, \beta)$ characteristics for different pitch angles and tip speed ratios. It can be observed that maximum power coefficient occurs at pitch angle $\beta=0$ degrees. This value also corresponds to the nominal tip speed ratio.

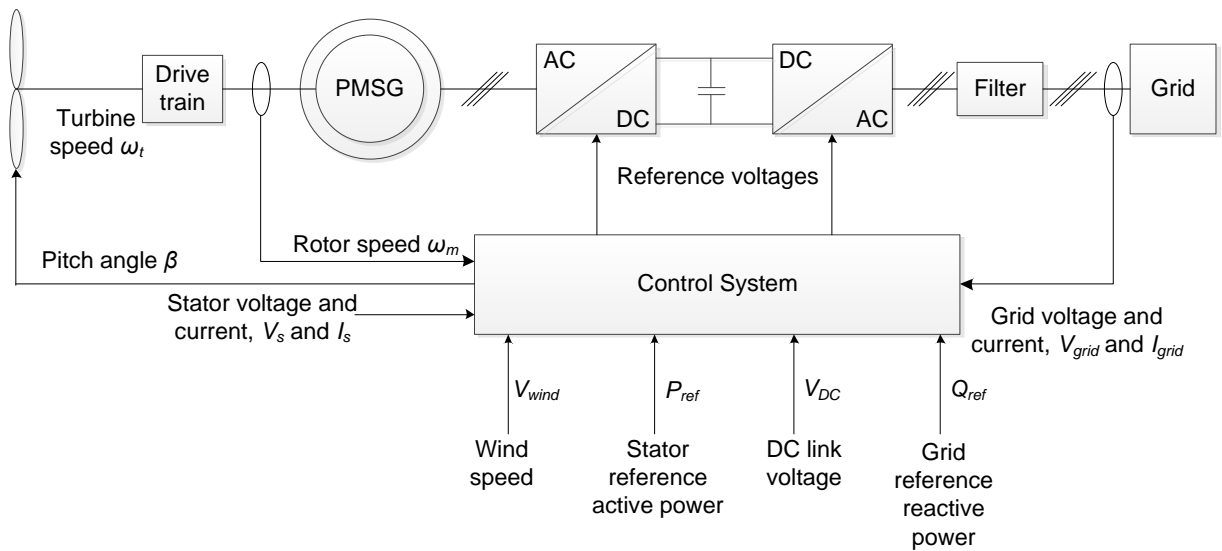


Figure 4.1: PMSG based wind turbine system

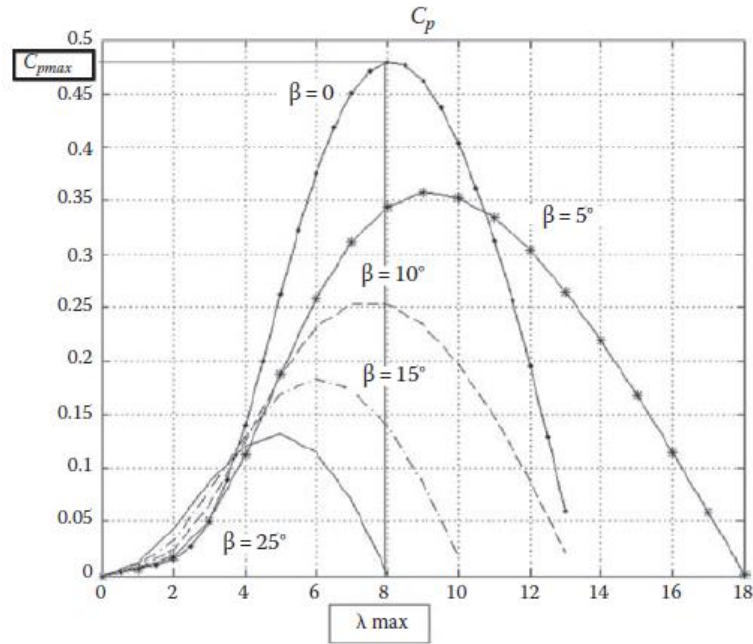


Figure 4.2: Power coefficient as a function of tip speed ratio (Perelmuter, 2013)

4.2 Drive train model

Different mechanical parts constitute the drive train of a wind turbine. These parts include the rotor, the shaft, the gearbox, and generator. The complexity of the drive train usually depends on the objectives and requirements of the study. Therefore, a one-mass, two-mass, or three-mass model may be used as the number of parameters to be considered increases.

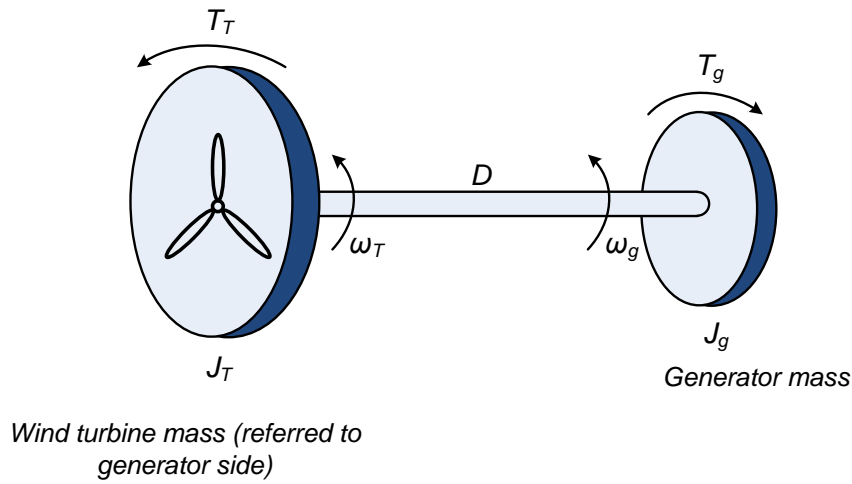


Figure 4.3: Drive train schematic modelling

Hence, a one-mass model might be enough when interactions between the wind farms and the grid are analysed (Rolan, et al., 2009; Melicio, et al., 2010).

Yet, even though generator speed dynamics have little influence on the grid side since the converters are totally decoupled and controlled independently, it is still advisable to consider a two-mass model representation for a variable speed wind turbine connected to the grid. In this approach, the drive-train connecting the generator and the turbine are represented by two mass spring system as illustrated in Figure 4.3. The system can further be lumped into one mass as expressed in Equation 4.3 below.

$$J_{eq} \frac{d}{dt} \omega_g = T_T - T_g - D \quad \text{Equation 4.3}$$

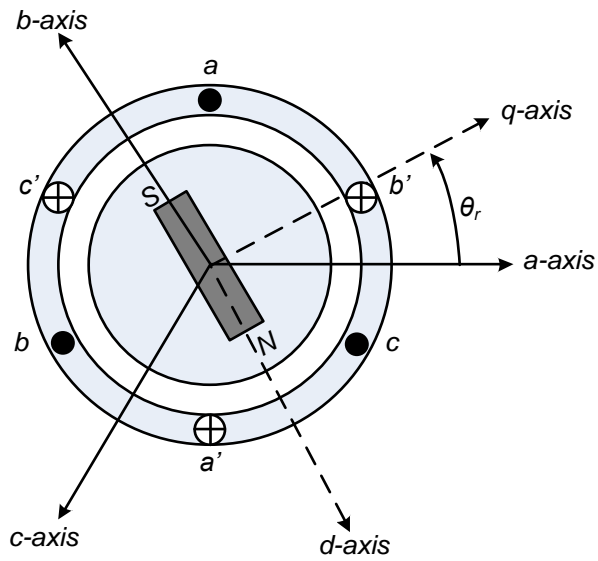
where J_{eq} is the combined inertia of the turbine and the generator in kg.m^2 , ω_g is the turbine rotational speed in rad/s , T_T and T_g are the turbine and generator torque respectively in Nm , and D is the friction coefficient in Nm/rad .

4.3 Modelling of the PMSG

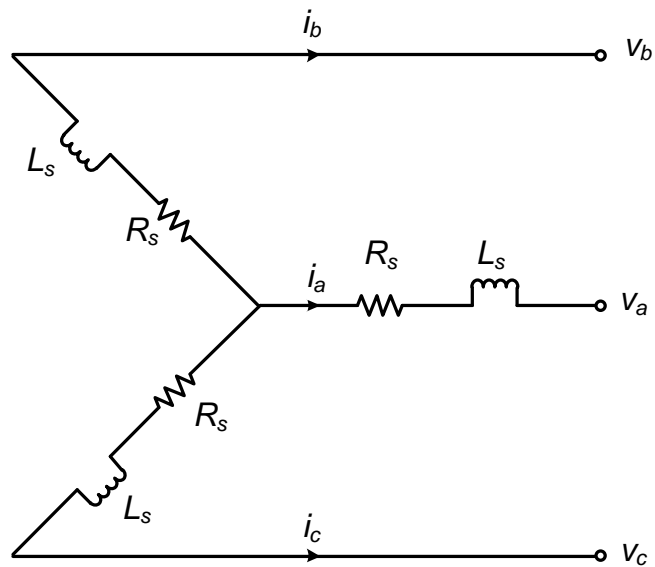
In Figure 4.4a, the cross-sectional area of a three-phase, two-pole PMSG is illustrated. The stator windings a_s , b_s , and c_s are distributed, sinusoidally identical, star connected with a 120-degree displacement between the three phases. Damper windings are neglected in this representation, due to the very little amount of current flowing through the permanent magnet rotor.

The PMSG stator equivalent circuit is shown in Figure 4.4b. N_s and R_s represent respectively the equivalent number of turns and resistance on each stator winding, while v_a , v_b and v_c are

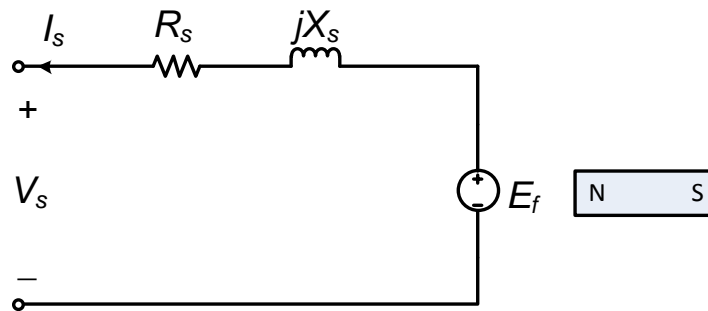
the stator phase terminal voltages. Figure 4.4c shows the per phase equivalent circuit of the PMSG.



(a) Cross sectional view of a two-pole PMSG



(b) Three-phase equivalent circuit of a PMSG



(c) Per phase equivalent circuit of a PMSG

Figure 4.4: Representation of a 2-pole, 3-phase, star connected PMSG

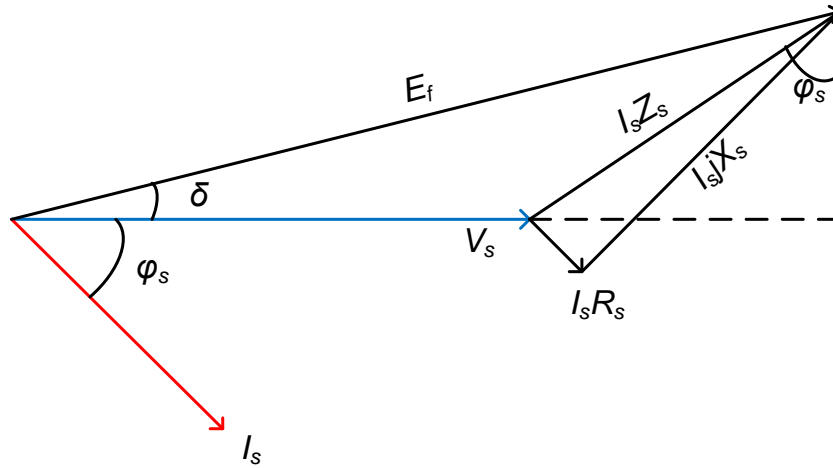


Figure 4.5: Phasor diagram of a PMSG

From Figure 4.4c, the phasor diagram of the PMSG is derived as illustrated in Figure 4.5 above, with the assumption that the current lags the voltage by a certain angle φ_s . This angle serves to determine the generator active and reactive powers P_s and Q_s expressed as:

$$\begin{aligned} P_s &= 3V_s I_s \cos\varphi_s \\ Q_s &= 3V_s I_s \sin\varphi_s \end{aligned} \quad \text{Equation 4.4}$$

The following relation can be derived from Figure 4.5:

$$E_f \sin\delta = Z_s I_s \cos\varphi_s \Rightarrow I_s \cos\varphi_s = \frac{|E_f|}{|Z_s|} \sin\delta \quad \text{Equation 4.5}$$

where δ , known as power angle, is the angle between E_f and V_s . Therefore, the generator active power can be rewritten as:

$$P_s = 3 \frac{|V_s| |E_f|}{|Z_s|} \sin\delta \quad \text{Equation 4.6}$$

Also, from Figure 4.5, the following relation can be obtained:

$$E_f \cos\delta = V_s + Z_s I_s \sin\varphi_s \Rightarrow I_s \sin\varphi_s = \frac{|E_f| \cos\delta - |V_s|}{|Z_s|} \quad \text{Equation 4.7}$$

In the same manner as the active power, the reactive power can be rewritten as:

$$Q_s = 3 \frac{|E_f| \cos\delta - |V_s|}{|Z_s|} \quad \text{Equation 4.8}$$

Since $R_s \ll X_s$, Equation 4.6 and Equation 4.8 can be rewritten neglecting R_s as:

$$P_s = 3 \frac{|V_s| |E_f|}{|X_s|} \sin \delta$$

$$Q_s = 3 \frac{|E_f| \cos \delta - |V_s|}{|X_s|}$$

Equation 4.9

When developing the model of a PMSG, it is assumed that (Kundur, 1994):

- The induced emf is sinusoidal
- The field current remains constant
- Magnetic hysteresis and eddy currents are negligible
- Magnetic saturation effects are negligible
- Permanent magnets have no conductivity

4.3.1 Reference frame theory

In order to simplify the analysis of synchronous and induction machines, as well as the implementation of different WECS based control techniques, reference frame transformations from natural three-phase abc to two-phase stationary $\alpha\beta$ and rotating dq synchronous frames and vice-versa, are often utilised. The abc to $\alpha\beta$ transformation also known as Clark's transformation is given as (Wu, et al., 2011):

$$\begin{pmatrix} x_\alpha \\ x_\beta \end{pmatrix} = \frac{2}{3} \begin{pmatrix} 1 & -1/2 & -1/2 \\ 0 & \sqrt{3}/2 & -\sqrt{3}/2 \end{pmatrix} \begin{pmatrix} x_a \\ x_b \\ x_c \end{pmatrix}$$

Equation 4.10

Similarly, the inverse Clark's from $\alpha\beta$ to abc is given by:

$$\begin{pmatrix} x_a \\ x_b \\ x_c \end{pmatrix} = \begin{pmatrix} 1 & 0 \\ -1/2 & \sqrt{3}/2 \\ -1/2 & -\sqrt{3}/2 \end{pmatrix} \begin{pmatrix} x_\alpha \\ x_\beta \end{pmatrix}$$

Equation 4.11

Park's transformation is used to switch from the natural abc frame to the dq frame. The Park's transformation and inverse Park are given by Equation 4.12 and Equation 4.13 respectively:

$$\begin{pmatrix} x_d \\ x_q \end{pmatrix} = \frac{2}{3} \begin{pmatrix} \cos \theta & \cos(\theta - 2\pi/3) & \cos(\theta - 4\pi/3) \\ -\sin \theta & -\sin(\theta - 2\pi/3) & -\sin(\theta - 4\pi/3) \end{pmatrix} \begin{pmatrix} x_a \\ x_b \\ x_c \end{pmatrix}$$

Equation 4.12

$$\begin{pmatrix} x_a \\ x_b \\ x_c \end{pmatrix} = \begin{pmatrix} \cos\theta & -\sin\theta \\ \cos(\theta - 2\pi/3) & -\sin(\theta - 2\pi/3) \\ \cos(\theta - 4\pi/3) & -\sin(\theta - 4\pi/3) \end{pmatrix} \begin{pmatrix} x_d \\ x_q \end{pmatrix} \quad \text{Equation 4.13}$$

4.3.2 Dynamic model

The voltage equations of the PMSG in the d - q axis rotor field synchronous reference frame can be expressed using the following equations (Wu, et al., 2011; Bunjongjit & Kumsuwan, 2013):

$$\begin{aligned} v_{ds} &= -R_s i_{ds} - \omega_r \lambda_{qs} + L_{ds} \frac{d}{dt} \lambda_{ds} \\ v_{qs} &= -R_s i_{qs} - \omega_r \lambda_{ds} + L_{qs} \frac{d}{dt} \lambda_{qs} \end{aligned} \quad \text{Equation 4.14}$$

where v_{ds} , v_{qs} , i_{ds} , i_{qs} , L_d , L_q , represent the d and q axis stator voltages, currents, and self-inductances respectively. The d and q -axis stator flux linkages are given as:

$$\begin{aligned} \lambda_{ds} &= -L_d i_{ds} + \lambda_r \\ \lambda_{qs} &= -L_q i_{qs} \end{aligned} \quad \text{Equation 4.15}$$

The rotor flux λ_r and the d and q -axis self-inductances L_d and L_q are in turn defined by:

$$\begin{aligned} \lambda_r &= L_{dm} I_f \\ L_d &= L_{ls} + L_{dm} \\ L_q &= L_{ls} + L_{qm} \end{aligned} \quad \text{Equation 4.16}$$

where L_{dm} and L_{qm} represent the d and q axis magnetising inductances respectively, L_{ls} represents the stator leakage inductance, and I_f is the field current.

Substituting Equation 4.15 into Equation 4.14, the voltage equations can be rewritten as:

$$\begin{aligned} v_{ds} &= -R_s i_{ds} + \omega_r L_{qs} i_{qs} - L_{ds} \frac{d}{dt} i_{ds} \\ v_{qs} &= -R_s i_{qs} - \omega_r L_{ds} i_{ds} + \omega_r \lambda_r - L_{qs} \frac{d}{dt} i_{qs} \end{aligned} \quad \text{Equation 4.17}$$

The electromagnetic torque is given by the formula:

$$T_e = \frac{3P}{2} (i_{qs} \lambda_{ds} - i_{ds} \lambda_{qs}) \quad \text{Equation 4.18}$$

where P represents the number of pole pairs.

Substituting Equation 4.15 into Equation 4.18, the expression for electromagnetic torque can be rewritten as:

$$T_e = \frac{3P}{2} [\lambda_r i_{qs} - (L_d - L_q) i_{ds} i_{qs}] \quad \text{Equation 4.19}$$

Finally, the rotor speed is expressed as:

$$\omega_r = \frac{P}{JS} (T_e - T_m) \quad \text{Equation 4.20}$$

with T_m representing the mechanical, J the rotor inertia, and S the Laplace operator.

4.3.3 Steady state model

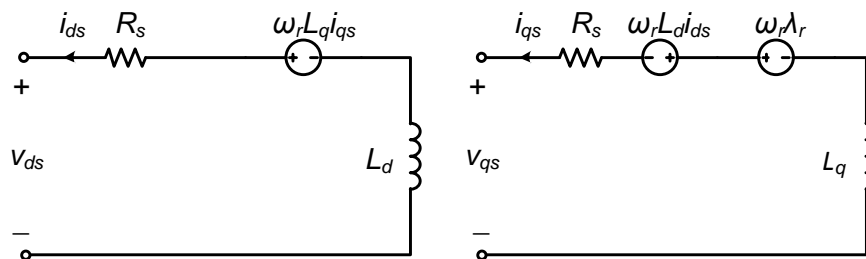
In the steady-state model, stator currents i_{ds} and i_{qs} are considered DC values, making their derivatives equal to zero. Equation 4.17 above becomes (Wu, et al., 2011):

$$v_{ds} = -R_s i_{ds} + \omega_r L_q i_{qs} \quad \text{Equation 4.21}$$

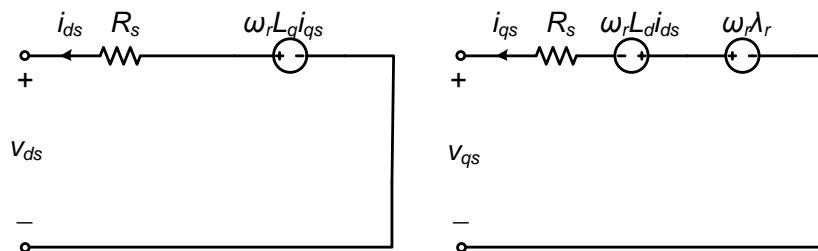
$$v_{qs} = -R_s i_{qs} - \omega_r L_d i_{ds} + \omega_r \lambda_r$$

4.3.4 Equivalent circuit of the PMSG

The simplified equivalent circuits of the PMSG are shown in Figure 4.6a and 4.6b for the dynamic and steady state models respectively. Note that the direction of the currents is out of the stator. This representation is according to the generator mode convention



(a) Dynamic model



(b) Steady state model

Figure 4.6: Simplified equivalent circuits of PMSG

4.4 Modelling of the back-to-back voltage source converter

The machine side rectifier and the grid side inverter are shown in Figure 4.7 and 4.8 respectively. Both converters use PWM signals to convert the three-phase electrical power from the generator to a stable DC value on the generator side, and DC power to three-phase AC from the DC-link to the electrical grid on the grid side inverter. The converters are two-level full bridge composed of three legs, each of them carrying one IGBT on the upper and lower levels. R_s and L_s are the stator phase resistance and inductance respectively, and v_{an} , v_{bn} , v_{cn} are the respective phase voltages. The DC link ensures proper power transfer from the generator to the grid. The power flow is illustrated in Figure 4.9 and can be expressed as (Anaya-Lara, et al., 2009):

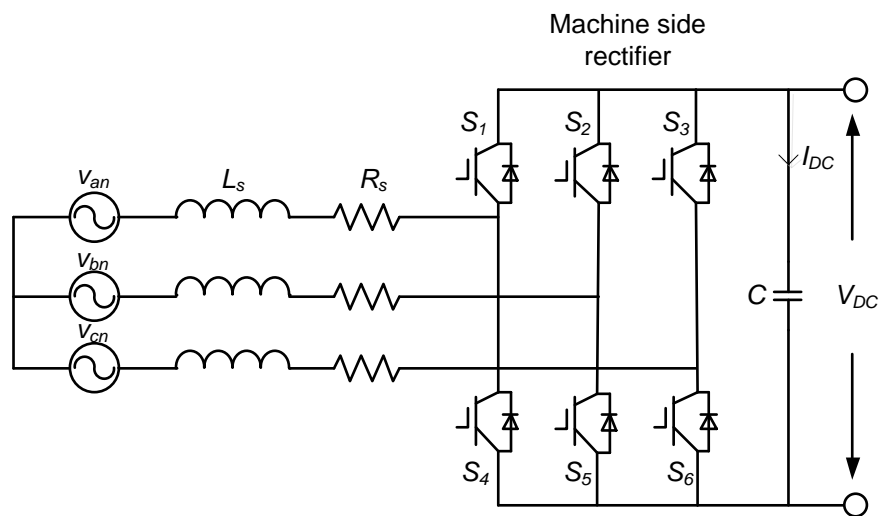


Figure 4.7: Machine side rectifier

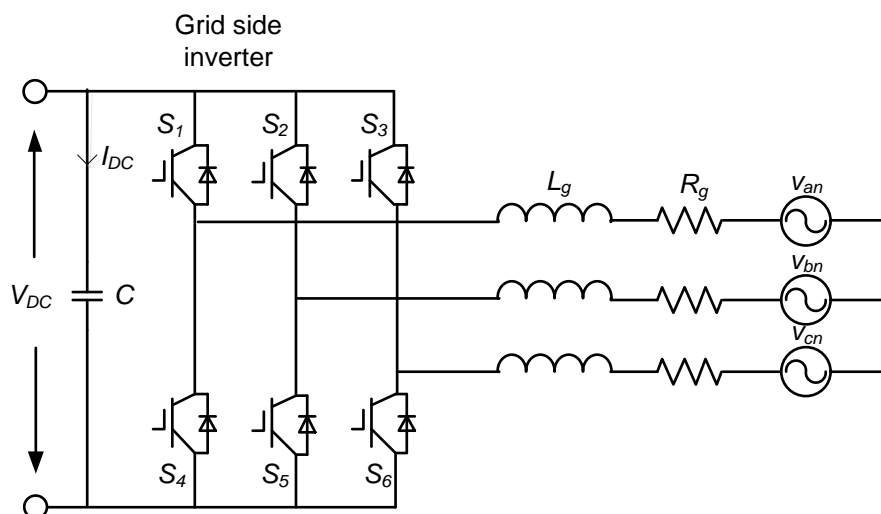


Figure 4.8: Grid side inverter

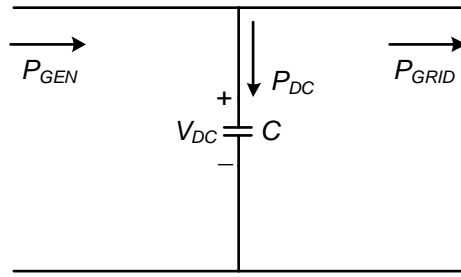


Figure 4.9: Power flow in the WTS

$$P_{DC} = P_{GEN} - P_{GRID} \quad \text{Equation 4.22}$$

P_{GEN} is the electrical output power of the generator, P_{GRID} the power transmitted to the grid, and P_{DC} the power absorbed by the DC link capacitor which can be given as:

$$P_{DC} = V_{DC} \cdot C \frac{dV_{DC}}{dt} \quad \text{Equation 4.23}$$

where V_{DC} is the voltage across the capacitor, C is the capacitance in Farads, and the term $C \frac{dV_{DC}}{dt}$ represents the current flowing through the DC link capacitor i_{DC} .

Equation 4.23 above can be rewritten as:

$$P_{DC} = \frac{C}{2} \frac{dV_{DC}^2}{dt} \quad \text{Equation 4.24}$$

Making V_{DC} the subject of the formula gives:

$$V_{DC} = \sqrt{\frac{2}{C} \int P_{DC} dt} \quad \text{Equation 4.25}$$

Equation 4.22 into Equation 4.25 gives:

$$V_{DC} = \sqrt{\frac{2}{C} \int (P_{GEN} - P_{GRID}) dt} \quad \text{Equation 4.26}$$

As mentioned earlier in chapter 2, the back-to-back configuration allows bidirectional power flow. This means that both converters can act as rectifiers and inverters, depending on which direction the power is supplied. To investigate the power flow on the converters, the grid side inverter circuit is used as a reference as shown in Figure 4.10 (Wu, et al., 2011). The grid power is calculated as:

$$P_{GRID} = 3v_g i_g \cos\delta_g \quad \text{Equation 4.27}$$

where v_g and i_g are the grid phase voltage and current respectively, and δ_g is the grid power angle which is angular difference between v_g and i_g . This angle can be positive (leading power factor), negative (lagging power factor), or equal to zero (unity power factor). The power angle can be used to determine the direction of power flowing through the converter as shown in Figure 4.10. If $P_{grid} < 0$, the power flow is towards the grid, if $P_{grid} > 0$, the power flows towards the converter, and if $P_{grid} = 0$ there is no power flow (Wu, et al., 2011).

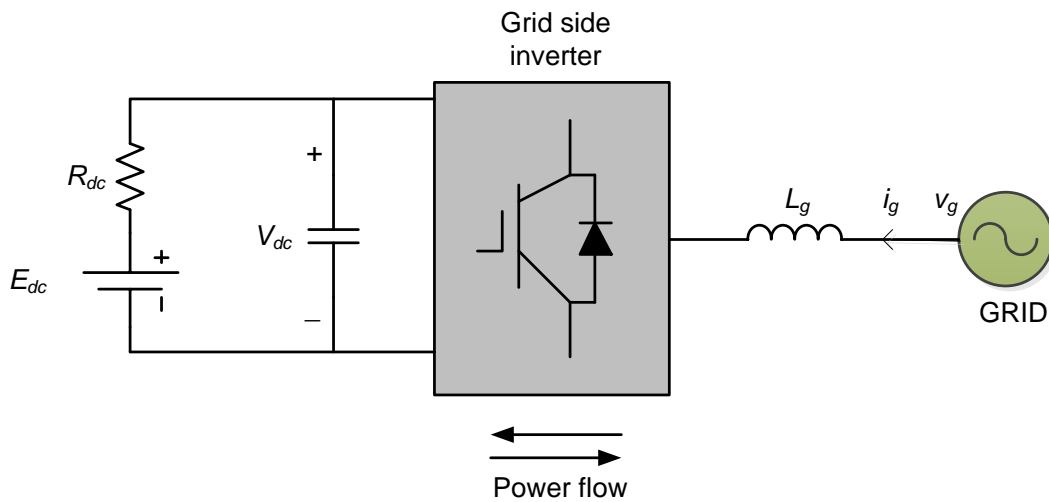


Figure 4.10: Direction of power flowing through the inverter

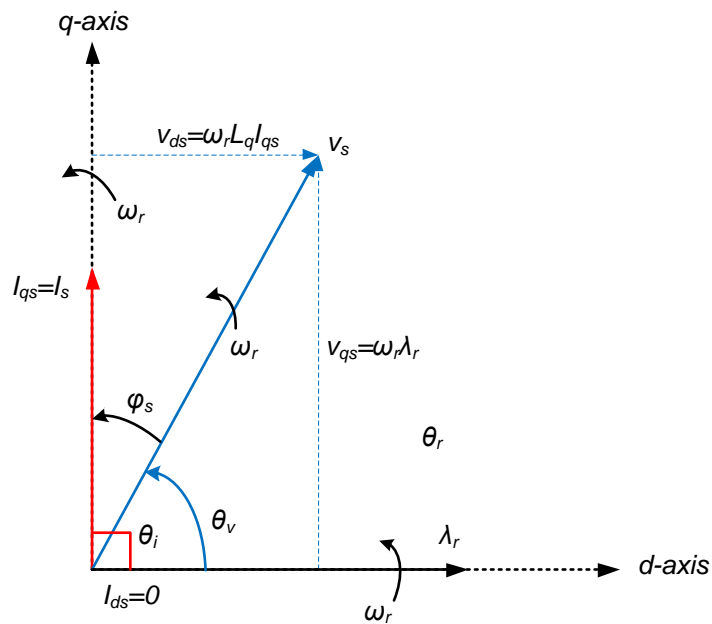


Figure 4.11: Phasor diagram of the field-oriented control

4.4.1 Generator side converter control

The generator side converter control is achieved using field-oriented control. Field oriented control of three-phase AC machines allows separate control of the torque and the rotor flux, emulating the principle of operation of DC machines. Figure 4.11 represents the phasor diagram of the field-oriented control, where α_r is the torque angle and θ_r the rotor angle. If the d -axis stator current i_{ds} is made zero, the stator current is equal to its q -axis component and is kept at 90 degrees with respect to the rotor flux, for maximum torque production (Wu, et al., 2011; Bunjongjit & Kumsuwan, 2013). Equation 4.19 can therefore be simplified to:

$$T_e = \frac{3P}{2} [\lambda_r i_{qs}] \quad \text{Equation 4.28}$$

From the above equation, it is clear that the electromagnetic torque can be easily controlled through the stator q -axis current component i_{qs} , since the flux is constant. Figure 4.12 shows the block diagram of the generator side controller used in this work. As illustrated, the three-phase stator currents i_a , i_b , and i_c are first acquired and combined into a space vector. The rotor flux angle is then obtained by finding the rotor angle of the PMSG, since the rotor and the flux rotate synchronously. In practice, this is achieved by placing an encoder on the rotor shaft. The three-phase currents are transformed and the equivalent d and q -axis currents i_{ds} and i_{qs} are obtained, such that they sit at zero degree and 90 degrees respectively with respect to the rotor flux angle. The d -axis current reference value i_{ds}^* is set to zero and the reference q -axis current component i_{qs}^* is derived from the reference torque using Equation 4.28 above. Torque reference is calculated using OTC as explained in chapter 2. Error d and q -axis stator currents are passed through proportional-integral (PI) regulators, then a decoupling controller derived from Equation 4.21 above is used. The resulting d and q -axis rectifier voltages v_{dr}^* and v_{qr}^* are acquired then transformed back from rotating dq to natural abc frame, and the three phase stator reference voltages v_{ar}^* , v_{br}^* , v_{cr}^* are obtained. The three voltages serve as input to the pulse width modulator (PWM) to generate the switching pattern of the rectifier controlling active power. θ_r is the measured rotor angle, and i_{as} , i_{bs} , i_{cs} are the measured three-phase stator currents (Wu, et al., 2011; Bunjongjit & Kumsuwan, 2013). The decoupling principle is explained in the next section.

4.4.2 Grid side converter control

Similarly to the FOC on the generator side, voltage oriented control (VOC) is employed on the grid side. In this case, the q -axis voltage component of the rotating frame is set to zero while the d -axis is aligned with the grid voltage vector. This way, the control of generated

active power is ensured by the d -axis, while the reactive power control depends on d and q -axis current components respectively as expressed in Equation 4.29 (Wu, et al., 2011).

$$P_g = \frac{3}{2}(v_{dg}i_{dg} + v_{qg}i_{qg})$$

$$Q_g = \frac{3}{2}(v_{qg}i_{dg} - v_{dg}i_{qg})$$

Equation 4.29

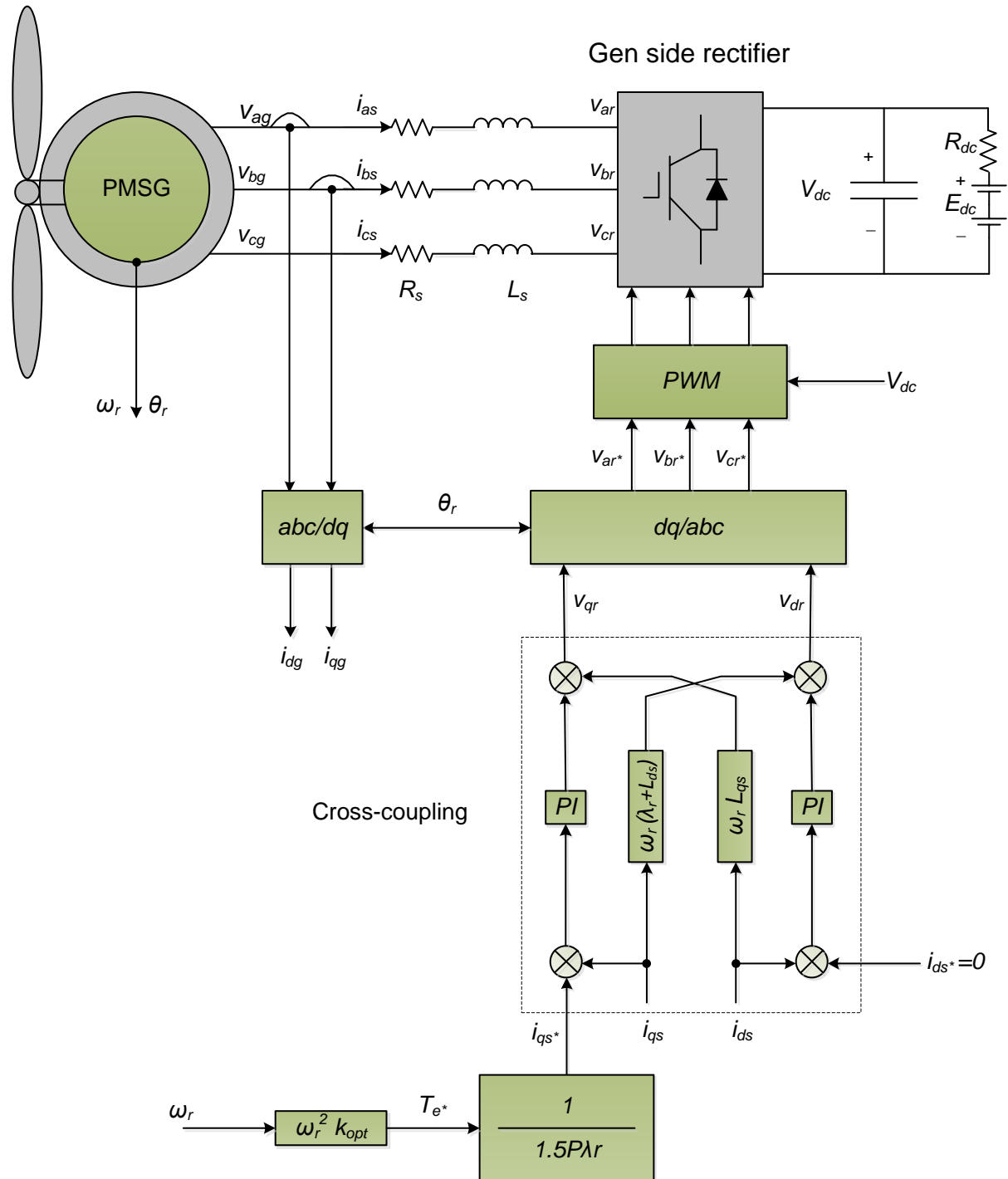


Figure 4.12: Generator side converter control

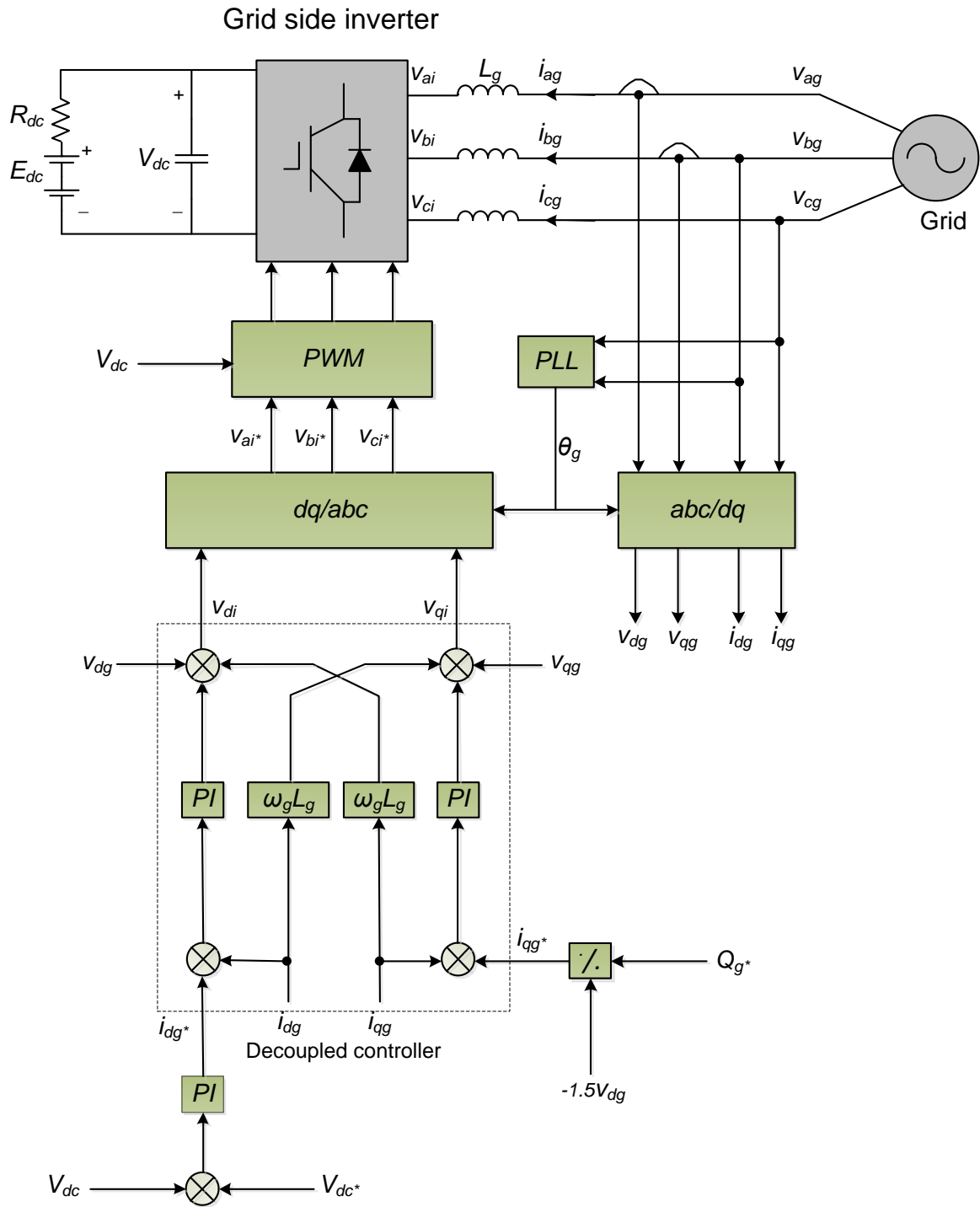


Figure 4.13: Grid side converter control

Since v_{qg} is set to zero, the grid active and reactive powers can be simplified as:

$$P_g = \frac{3}{2} v_{dg} i_{dg}$$

$$Q_g = -\frac{3}{2} v_{dg} i_{qg}$$

Equation 4.30

If the converter losses are neglected, it can be assumed that the active power is the same on both DC and AC sides of the inverter. Therefore, P_g in Equation 4.29 above can be rewritten as:

$$P_g = \frac{3}{2} v_{dc} i_{dc} \quad \text{Equation 4.31}$$

Equation 4.31 shows that the reference grid d -axis current can be used for the control of the DC-link voltage v_{dc} . On the other side, the q -axis current component can be derived from Q_g in Equation 4.32 as:

$$i_{qg} = -\frac{2Q_g}{3v_{dg}} \quad \text{Equation 4.32}$$

The block diagram of the grid side control is presented in Figure 4.13. As illustrated, the control uses two main external feedback loops, one for the control of the DC link voltage and the other for the control of reactive power. Two internal current control loops are also available for the control of d and q current components generated from the DC link voltage and the reactive power respectively (Wu, et al., 2011).

The three-phase grid voltages and currents, as well as the DC-link voltage measurements are first acquired. In order to realise reference frame transformations from abc to dq and vice versa, the grid voltage vector angle θ_g is needed. The phase locked loop (PLL) technique is therefore applied to track the grid voltage vector and extract its angle (Wu, et al., 2011). The dq equations of the grid voltages are expressed as:

$$\begin{aligned} v_{dg} &= R_g i_{dg} + L_g \frac{d}{dt} i_{dg} - \omega_g L_g i_{qg} + v_{di} \\ v_{qg} &= R_g i_{qg} + L_g \frac{d}{dt} i_{qg} + \omega_g L_g i_{dg} + v_{qi} \end{aligned} \quad \text{Equation 4.33}$$

where v_{di} and v_{qi} represent the d and q -axis inverter voltages respectively, ω_g the grid angular velocity, R_g and L_g the grid resistance and inductance respectively. The above equation shows the cross-coupling nature of the system control, since both d and q terms are present in each one of the expressions v_{gd} and v_{gq} . Consequently, a decoupling controller is used to ease calculations and improve the dynamic response of the controller (Wu, et al., 2011).

Rearranging the terms in Equation 4.33, Equation 4.34 is obtained as:

$$v_{di} = -(R_g i_{dg} + L_g \frac{d}{dt} i_{dg}) + \omega_g L_g i_{qg} + v_{dg}$$

$$v_{qi} = -(R_g i_{qg} + L_g \frac{d}{dt} i_{qg}) - \omega_g L_g i_{dg} + v_{qg}$$

Equation 4.34

Considering the PI nature of the controllers, Equation 4.34 can be rewritten as:

$$v_{di} = -(k_{ipd} + \frac{k_{iud}}{s})(i_{dg}^* - i_{dg}) + \omega_g L_g i_{qg} + v_{dg}$$

$$v_{qi} = -(k_{ipq} + \frac{k_{iiq}}{s})(i_{qg}^* - i_{qg}) - \omega_g L_g i_{dg} + v_{qg}$$

Equation 4.35

where i_{dg}^* and i_{qg}^* are the d and q -axis reference currents, k_{ipd} and k_{iud} are the d -axis proportional and integral gains, k_{ipq} and k_{iiq} are the q -axis proportional and integral gains respectively. Rearranging Equation 4.34 and Equation 4.35, and substituting the first one into the second, the following expressions are obtained (Wu, et al., 2011):

$$R_g i_{dg} + L_g \frac{d}{dt} i_{dg} = (k_{ipd} + \frac{k_{iud}}{s})(i_{dg}^* - i_{dg})$$

$$R_g i_{qg} + L_g \frac{d}{dt} i_{qg} = (k_{ipq} + \frac{k_{iiq}}{s})(i_{qg}^* - i_{qg})$$

Equation 4.36

From the above equation, it can be noted that the d -axis and q -axis components are clearly separated from each other, showing the decoupled nature of the control system. In Figure 4.13, v_{ai}^* , v_{bi}^* , v_{ci}^* are the reference inverter three phase voltages, v_{ag} , v_{bg} , and v_{cg} are the measured grid three-phase voltages, i_{ag} , i_{bg} , and i_{cg} , the measured grid three-phase currents respectively (Wu, et al., 2011).

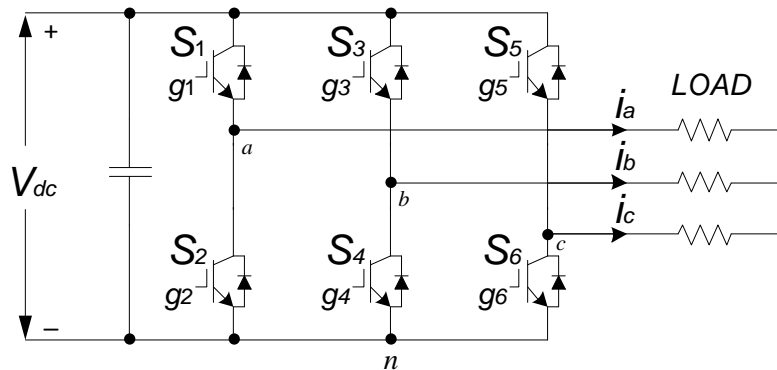


Figure 4.14: Two-level voltage source converter topology

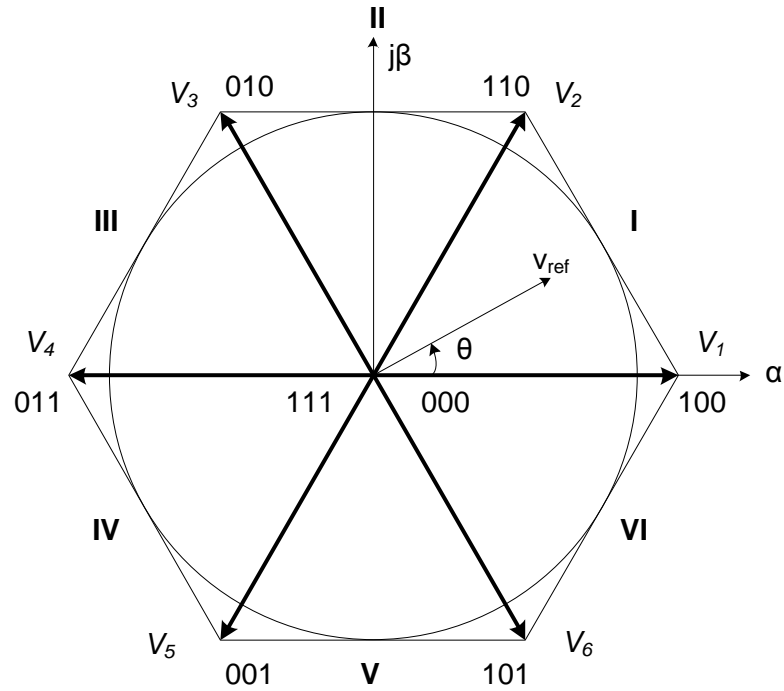


Figure 4.15: Space vector diagram of the two-level inverter

4.4.3 Space vector modulation (SVM)

4.4.3.1 Switching states

Figure 4.14 above represents the typical configuration of a two level VSC. The converter consists of three upper and lower switches of which each switch can be ON or OFF. It is also important to note that the upper switch and the lower switch on one leg of the converter can never be at the same state for the correct operation of this converter (Wu, et al., 2011). For simplification, only the states of the upper switches will be considered in this analysis.

Let's represent the ON state by 1 and the OFF state by 0. When one of the upper switches is ON (lower switch is OFF), the phase voltage is equal to the capacitor voltage V_{dc} . On the contrary, if the upper switch is OFF (lower switch is ON), then the phase voltage is 0. For instance, if S1 is ON, then v_{an} is equal to V_{dc} , otherwise, v_{an} is equal to 0. This gives the possibility for eight different switching combinations (2^3) instead of 64 (2^6) if all the switches were to be considered (Wu, et al., 2011). Table 4.1 can therefore be derived.

4.4.3.2 Relationship between space vectors and switching states

Assuming a balanced three phase load, the following equation can be written:

$$v_{an}(t) + v_{bn}(t) + v_{cn}(t) = 0 \quad \text{Equation 4.37}$$

Table 4.1: Switching states and output voltages of the inverter

Switching States			Line to neutral voltages		
<i>a</i>	<i>b</i>	<i>c</i>	V_{an}	V_{bn}	V_{cn}
S_1	S_3	S_5			
0	0	0	0	0	0
1	0	0	V_{dc}	0	0
1	1	0	V_{dc}	V_{dc}	0
0	1	0	0	V_{dc}	0
0	1	1	0	V_{dc}	V_{dc}
0	0	1	0	0	V_{dc}
1	0	1	V_{dc}	0	V_{dc}
1	1	1	V_{dc}	V_{dc}	V_{dc}

where v_{an} , v_{bn} , and v_{cn} represent the load three-phase voltages at an instant t . The three-phase variables can be transformed into two-phase by applying the abc to $\alpha\beta$ transformation discussed in section 4.3.1, to obtain a space vector $v(t)$ as expressed in Equation 4.39 (Wu, et al., 2011):

$$\begin{bmatrix} v_{\alpha}(t) \\ v_{\beta}(t) \end{bmatrix} = \frac{2}{3} \begin{bmatrix} 1 & -\frac{1}{2} & -\frac{1}{2} \\ 0 & \frac{\sqrt{3}}{2} & -\frac{\sqrt{3}}{2} \end{bmatrix} \begin{bmatrix} v_{an}(t) \\ v_{bn}(t) \\ v_{cn}(t) \end{bmatrix} \quad \text{Equation 4.38}$$

$$\vec{v}(t) = v_{\alpha}(t) + jv_{\beta}(t) \quad \text{Equation 4.39}$$

Further developing expression Equation 4.38 and substitution into Equation 4.39 leads to:

$$\vec{v}(t) = \frac{2}{3} v_{an}(t) - \left(\frac{1}{3} - j\frac{\sqrt{3}}{3} \right) v_{bn}(t) - \left(\frac{1}{3} + j\frac{\sqrt{3}}{3} \right) v_{cn}(t) \quad \text{Equation 4.40}$$

The above equation can also be written in exponential form as:

$$\vec{v}(t) = \frac{2}{3} \left[v_{an}(t)e^{j0} + v_{bn}(t)e^{j\frac{2\pi}{3}} + v_{cn}(t)e^{j\frac{4\pi}{3}} \right] \quad \text{Equation 4.41}$$

Table 4.2: Space vectors, switching states, and vectors definition

Vectors	Switching states	Vectors definition
V_0	000	0
V_1	100	$\frac{2}{3}V_{dc}$
V_2	110	$\frac{2}{3}V_{dc}e^{j\frac{\pi}{3}}$
V_3	010	$\frac{2}{3}V_{dc}e^{j\frac{2\pi}{3}}$
V_4	011	$\frac{2}{3}V_{dc}e^{j\pi}$
V_5	001	$\frac{2}{3}V_{dc}e^{j\frac{4\pi}{3}}$
V_6	101	$\frac{2}{3}V_{dc}e^{j\frac{5\pi}{3}}$
V_7	111	0

Considering the first active switching state in Table 4.1, $v_{an}=V_{dc}$, and $v_{bn}=v_{cn}=0$. Replacing those values into Equation 4.41, the corresponding space vector V_1 is obtained as:

$$\vec{V}_1 = \frac{2}{3}V_{dc} \quad \text{Equation 4.42}$$

Following the switching arrangement given in Table 4.1 above, the other space vector expressions can be obtained as shown in Table 4.2 above. From this table, the space vector diagram shown in Figure 4.16 can be generated. It is important to note the 60 degrees ($\pi/3$) phase difference between the stationary active space vectors. Figure 4.16 also shows that a reference vector v_{ref} can be produced from the two active space vectors and the zero space vectors that constitute a section. For instance, v_{ref} in section I of the space vector diagram is made of the active space vectors V_1 and V_2 , and the zero space vector V_0 . The reference vector v_{ref} is expressed as (Wu, et al., 2011):

$$v_{ref} = |v_{ref}|e^{j\theta} \quad \text{Equation 4.43}$$

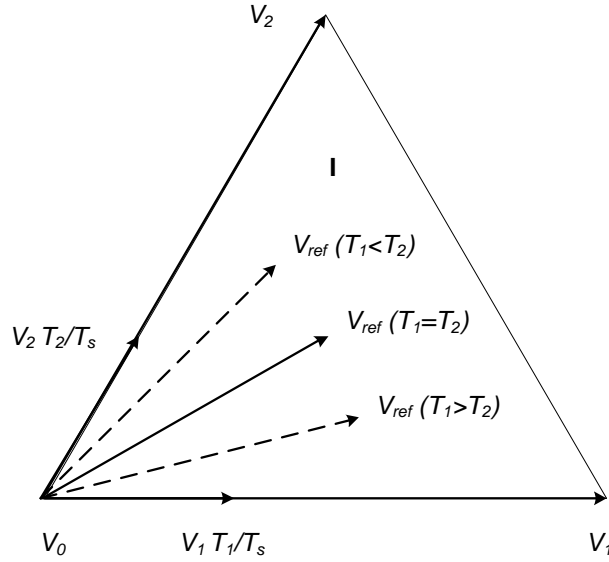


Figure 4.16: Space vector diagram of the grid side inverter

where $|v_{ref}|$ is the magnitude of the reference vector v_{ref} , and θ is the phase angle. These two quantities can be defined as:

$$\begin{cases} v_{ref} = \sqrt{(v_{\alpha})^2 + (v_{\beta})^2} \\ \theta = \tan^{-1} \frac{v_{\beta}}{v_{\alpha}} \end{cases} \quad \text{Equation 4.44}$$

4.4.3.3 Dwell time

In order to generate the reference space vector v_{ref} , selected switches need to be at a particular state (ON or OFF) and for a certain duration. The duration for which the selected switches are ON or OFF for a given sampling period T_s is called dwell time and can be calculated according to the volt-second balancing principle (Wu, et al., 2011). Assuming that v_{ref} is located in section I, then the volt-balancing equation can be written as:

$$v_{ref} T_s = V_1 T_1 + V_2 T_2 + V_0 T_0 \quad \text{Equation 4.45}$$

where T_1 , T_2 , and T_0 are the dwell times of V_1 , V_2 , and V_0 respectively and $T_s = T_1 + T_2 + T_0$.

Taking Equation 4.45 and making v_{ref} the subject of the formula, Equation 4.46 is obtained as:

$$v_{ref} = V_1 \frac{T_1}{T_s} + V_2 \frac{T_2}{T_s} + V_0 \frac{T_0}{T_s} \quad \text{Equation 4.46}$$

The above equation is illustrated in figure 4.16, where v_{ref} lies in sector I.

Substituting Equation 4.43 and the vectors definitions of vectors V_1 , V_2 , and V_0 from Table 4.2 into Equation 4.45, Equation 4.47 is obtained as (Wu, et al., 2011):

$$v_{ref} \cdot e^{j\theta} T_s = \frac{2}{3} V_{dc} T_1 + \frac{2}{3} V_{dc} T_2 e^{j\frac{\pi}{3}} \quad \text{Equation 4.47}$$

The real and imaginary components of the above equation can be derived as:

$$\begin{cases} v_{ref} \cos\theta T_s = \frac{2}{3} V_{dc} T_1 + \frac{1}{3} V_{dc} T_2 \\ v_{ref} \sin\theta T_s = \frac{\sqrt{3}}{3} V_{dc} T_2 \end{cases} \quad \text{Equation 4.48}$$

The dwell times can therefore be calculated using from Equation 4.49 below:

$$\begin{cases} T_1 = \frac{\sqrt{3} T_s v_{ref}}{V_{dc}} \sin\left(\frac{\pi}{3} - \theta\right) \\ T_2 = \frac{\sqrt{3} T_s v_{ref}}{V_{dc}} \sin\theta \\ T_0 = T_s - T_1 - T_2 \end{cases} \quad \text{Equation 4.49}$$

It is shown in Figure 4.16 that there is a relationship between v_{ref} and the magnitudes of the dwell times. As such, the relationship between the location of v_{ref} and the dwell times can be summarised as shown in

Table 4.4.

Table 4.3: Relationship between reference vector location and dwell times

v_{ref} location	$\theta = 0$	$0 < \theta < \pi/6$	$\theta = \pi/6$	$\pi/6 < \theta < \pi/3$	$\theta = \pi/3$
Dwell times	$T_a > 0; T_b = 0$	$T_a > T_b$	$T_a = T_b$	$T_a < T_b$	$T_b > 0; T_a = 0$

Equation 4.49 above can be rewritten in terms of the modulation index m_a as:

$$\begin{cases} T_1 = T_s m_a \sin\left(\frac{\pi}{3} - \theta\right) \\ T_2 = T_s m_a \sin\theta \\ T_0 = T_s - T_1 - T_2 \end{cases} \quad \text{Equation 4.50}$$

where

$$m_a = \frac{\sqrt{3} \times v_{ref}}{V_{dc}} \quad \text{Equation 4.51}$$

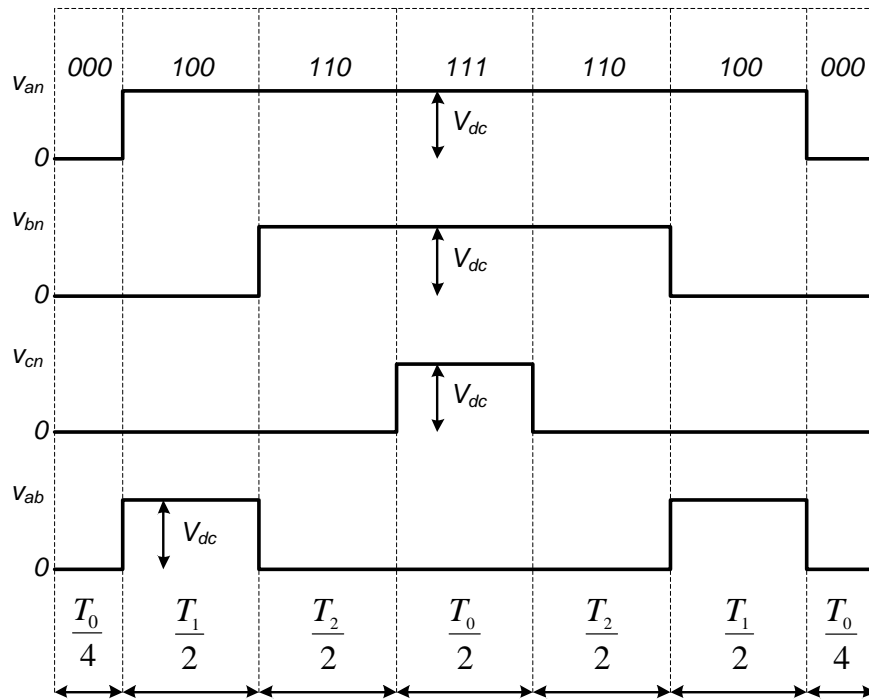


Figure 4.17: Seven-segment switching sequence for reference vector located in sector I

Table 4.4: Seven segment switching sequence

Sector	Switching sequence						
	1	2	3	4	5	6	7
I	V_0 000	V_1 100	V_2 110	V_0 111	V_2 110	V_1 100	V_0 000
II	V_0 000	V_3 010	V_2 110	V_0 111	V_2 110	V_3 010	V_0 000
III	V_0 000	V_3 010	V_4 011	V_0 111	V_4 011	V_3 010	V_0 000
IV	V_0 000	V_5 001	V_4 011	V_0 111	V_4 011	V_5 001	V_0 000
V	V_0 000	V_5 001	V_6 101	V_0 111	V_6 101	V_5 001	V_0 000
VI	V_0 000	V_1 100	V_6 101	V_0 111	V_6 101	V_1 100	V_0 000

4.4.3.4 Switching sequence

With the space vectors selected and the dwell times calculated, the switching sequence of the inverter can be obtained. Assuming that v_{ref} is located in sector I, the seven-segment switching sequence in Figure 4.17 is derived.

Table 4.4 summarises the switching sequence for all the seven sectors (Wu, et al., 2011).

Summary of the chapter

This chapter presented the mathematical modelling of the PMSG based WECS used in this work. Each section of the WECS was modelled separately from the mechanical turbine rotor and drive train, to the electrical generator and power converters. On the mechanical side, the turbine model equations were presented. The two-mass model implemented on the drive train was also discussed. On the electrical side both steady-state and dynamic models of the PMSG were discussed. Modelling equations and phasor diagram were derived and used for FOC of the generator side rectifier. The grid side inverter was also modelled using VOC and modelling equations were discussed. Finally, the space vector modulation used for the control of converters was presented and explained.

CHAPTER FIVE

SIMULATION RESULTS AND DISCUSSIONS

Introduction

In this chapter, simulation results for the proposed fault ride-through methods employed are presented and discussed. Different scenarios are implemented to gauge the capacity of the system in achieving LVVRT or not. A description of the complete power system is first given. The system modelling presented in the previous chapter is then validated through simulations under normal operating conditions (without grid disturbance), before simulations during grid faults are carried through. Finally, the results are analysed and compared, and small conclusions are drawn.

5.1 Power system configuration

The simulation model was developed using Simpowersystem, the power systems simulation tool of Matlab/Simulink. The complete power system and wind turbine models are presented in appendix B. Figure 5.1 is the single line diagram of the complete power system used for the simulation studies. The system consists of 6 x 1.5 MW wind turbines each connected to a 25 kV feeder through a 2 MVA transformer and 10 km transmission line. The 25 kV feeder supplies power to the 120kV grid using a 20 km transmission line and a 47 MVA step-up transformer. The grid is represented by a three-phase voltage source. The system parameters are presented in appendix A.

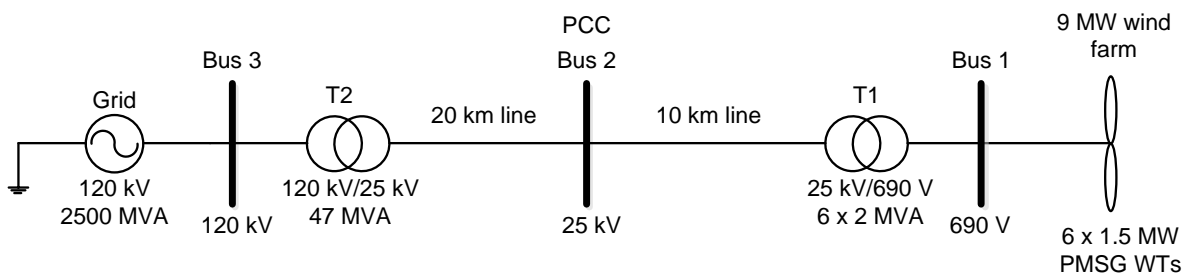


Figure 5.1: Single line diagram of the electric power system under study

5.2 Wind farm model aggregation

The wind farm model used in this work is an aggregated model consisting of a representation of many individual wind turbines lumped into one unit, as opposed to a detailed model in which every single turbine is represented and modelled separately. In fact, with the detailed model, simulations become more complex due to the increased overall system's complexity and simulation time, while the model aggregated technique is simpler and faster, still without compromising the accuracy of the results (Qiao, et al., 2007; Sanchez, et al., 2012).

As explained in literature (Koc, 2010), only electrical components are affected during model aggregation. Mechanical and aerodynamic parameters are not considered for aggregation. As a result, generator parameters such as rotor inertia, friction coefficient, pole pairs, turbine mechanical parameters and the pitch control system remain unchanged.

To achieve proper model aggregation, generator and converter power ratings are multiplied by the number of turbines in the wind farm, while resistive parameters are divided by this number to supply new rated current. It is also assumed, for more simplicity that the wind direction of the wind and the rotational speed are the same for all the individual wind turbines (Koc, 2010).

5.3 Simulation results under normal operating conditions

At first, the wind turbine system is tested under normal operating conditions to validate the effectiveness of the generator and grid side converter controllers in achieving MPPT and DC-link and reactive power control respectively. As such, the varying step wind speed profile shown in Figure 5.2 is used as input to the turbine model. The wind speed increases from 9 to 11 m/s with a 1 m/s increment rate then decreases back from 11 m/s to 9 m/s at the same rate, every 2 seconds. The pitch angle is maintained at maximum value (zero degree).

The results displayed show that MPPT is successfully achieved by the generator side converter. As shown in Figure 5.3, the generator mechanical speed varies according to the change in wind speed. At 11 m/s, the generator speed is equal to 1 p.u, then 0.91 p.u and 0.82 p.u respectively at 10 m/s and 9 m/s. These values correspond to the maximum per unit generator speed values for each wind speed. The mechanical torque is also displayed in Figure 5.4. Since torque control is used for MPPT, the torque variation also follows the wind speed input. The negative values indicate that the PMSM operates in the generator mode. In figures 5.5 and 5.6, the responses of the power coefficient and tip speed ratio are shown. As expected, the power coefficient remains constant at its rated value of 0.48 despite changes in wind speed, ensuring maximum power production from the turbine at lower and rated wind speeds. The tip speed ratio also remains constant at 8.1.

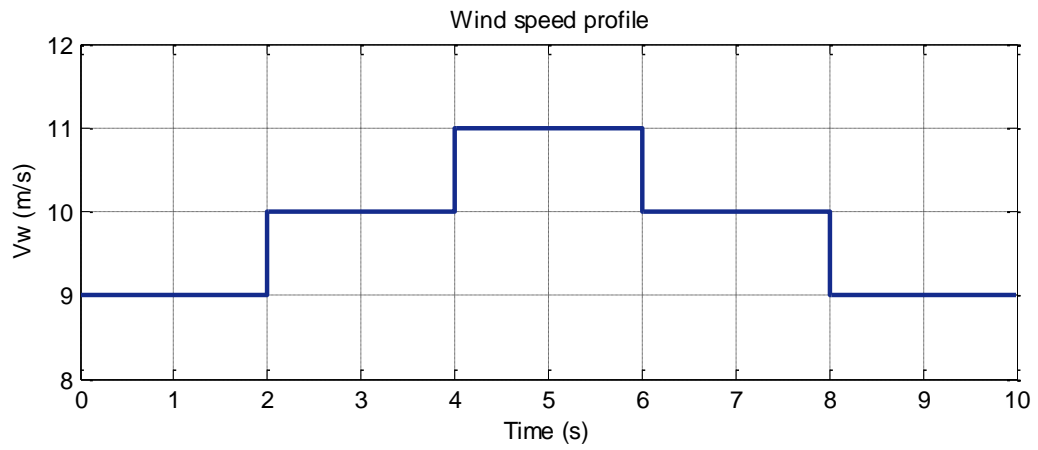


Figure 5.2: Wind speed profile

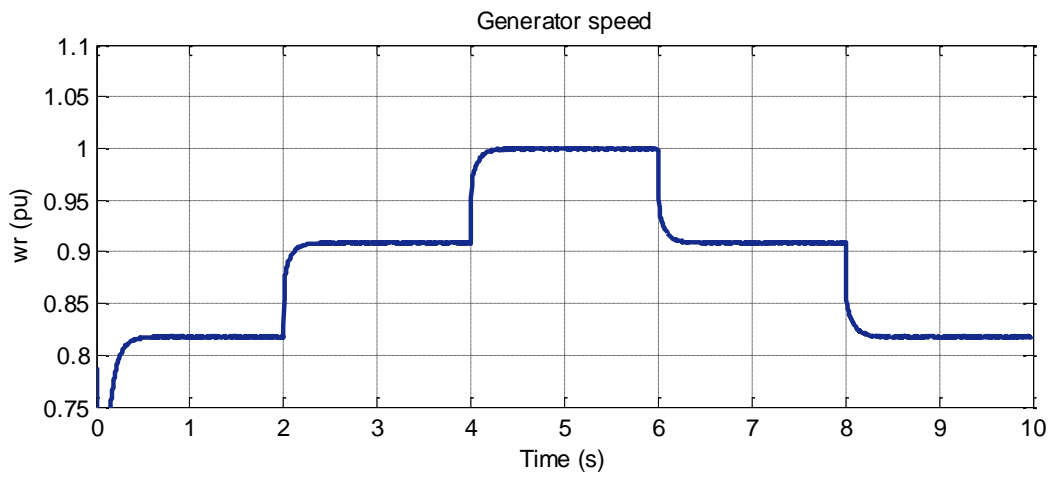


Figure 5.3: Generator speed

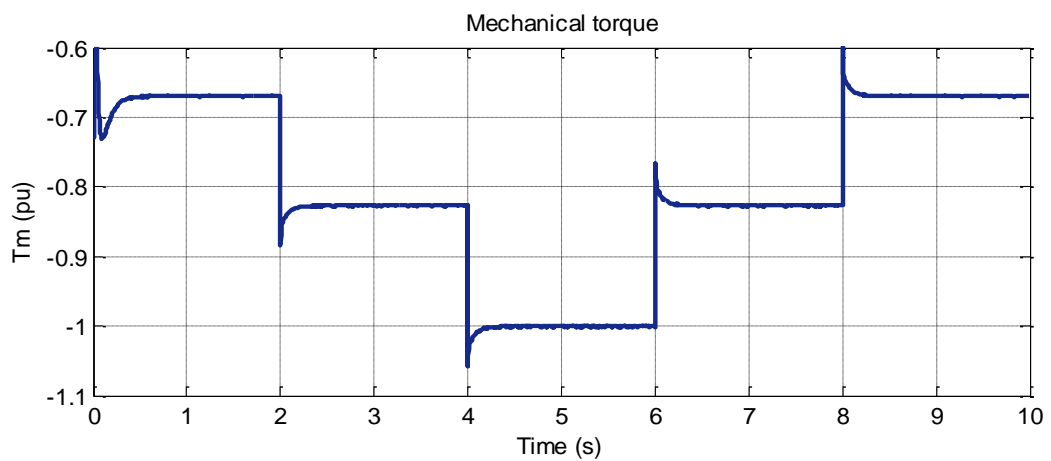


Figure 5.4: Turbine mechanical torque

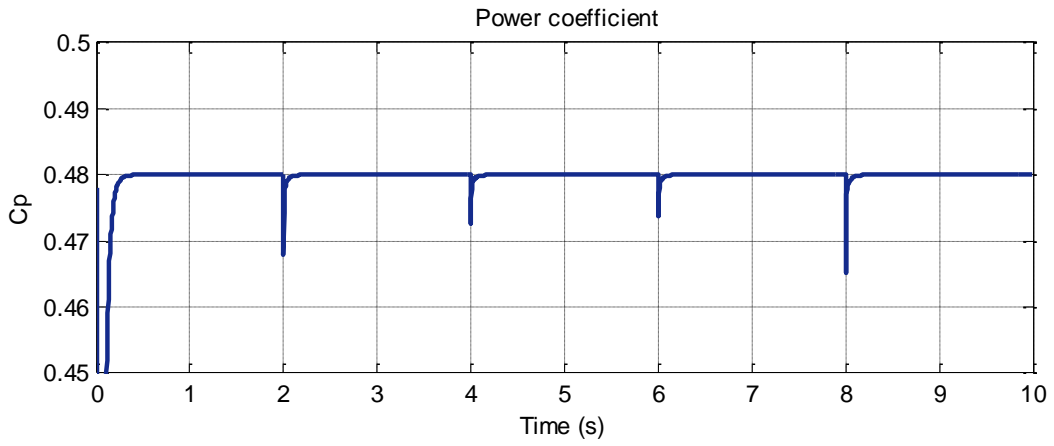


Figure 5.5: Wind turbine's power coefficient

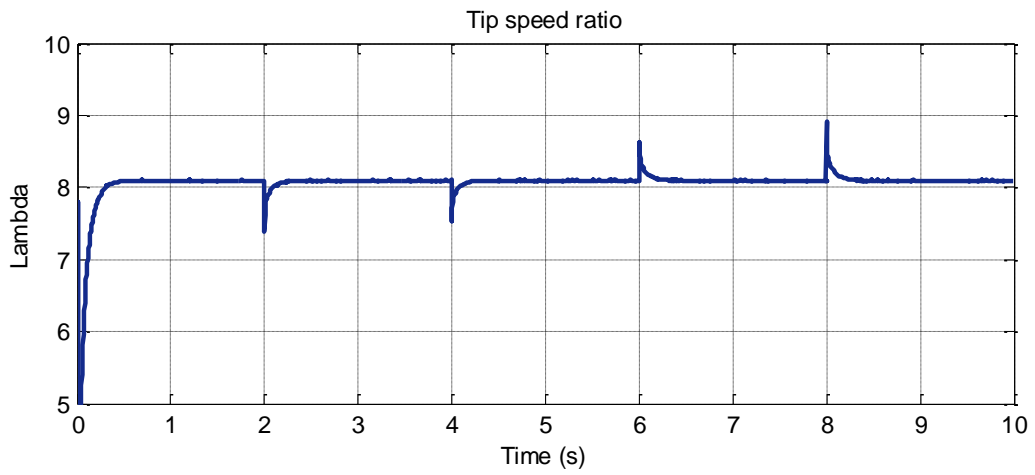


Figure 5.6: Wind turbine's tip speed ratio

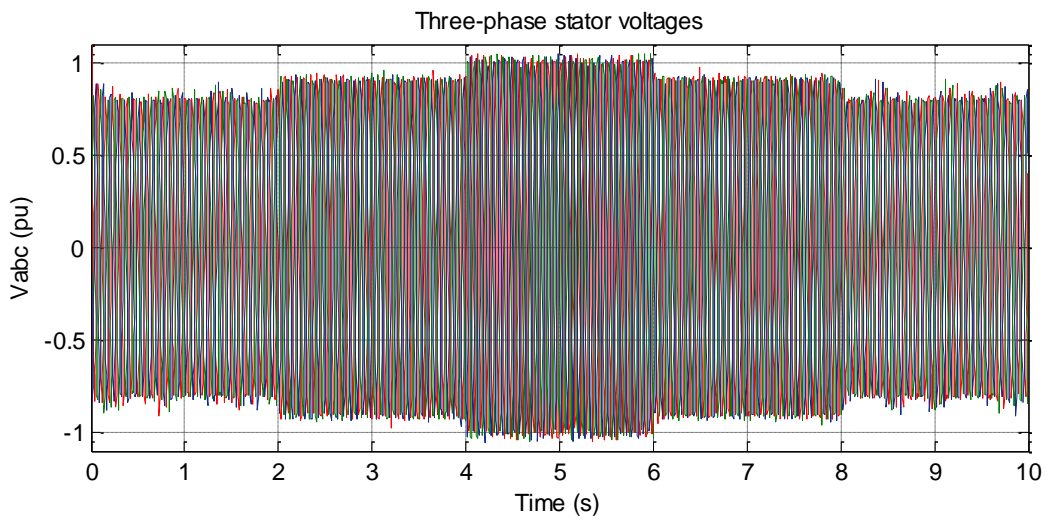


Figure 5.7: Three phase stator voltages

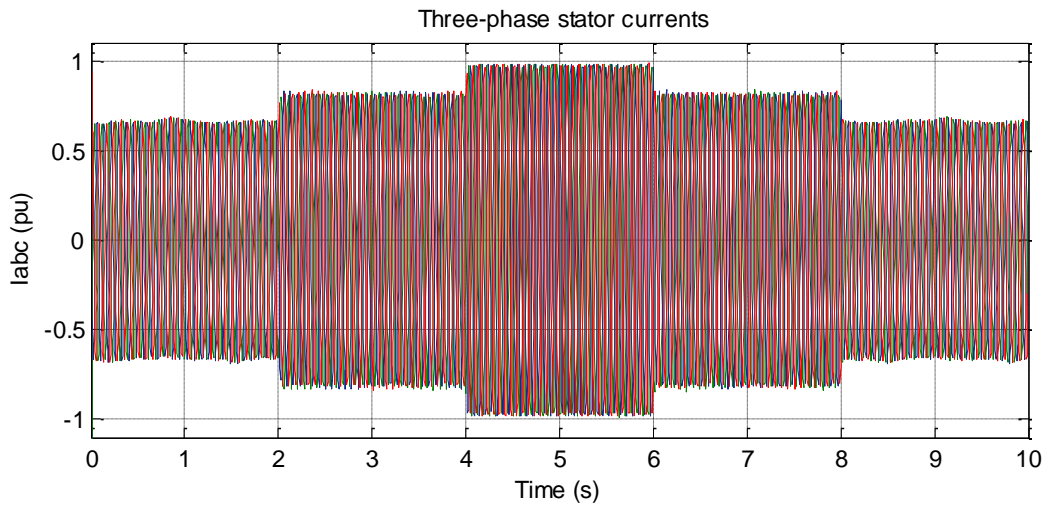


Figure 5.8: Three phase stator currents

As far as the electrical parameters are concerned, the three-phase stator voltages and currents are displayed on Figure 5.7 and 5.8 respectively. These results show that the voltages are proportional to the generator speed, while the currents are proportional to the mechanical torque, both in magnitude. The stator power is also shown in Figure 5.9. The d-axis and q-axis stator currents are shown with their references in Figure 5.10. The d-axis current is constant at 0 p.u., to achieve zero d-axis current control and magnitude of the q-axis current is equal to the stator current as expected.

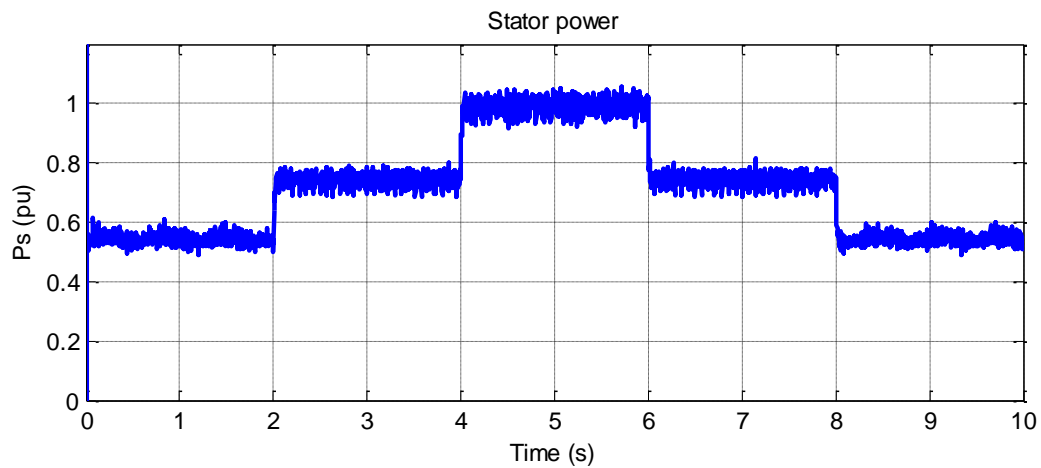


Figure 5.9: Stator active power

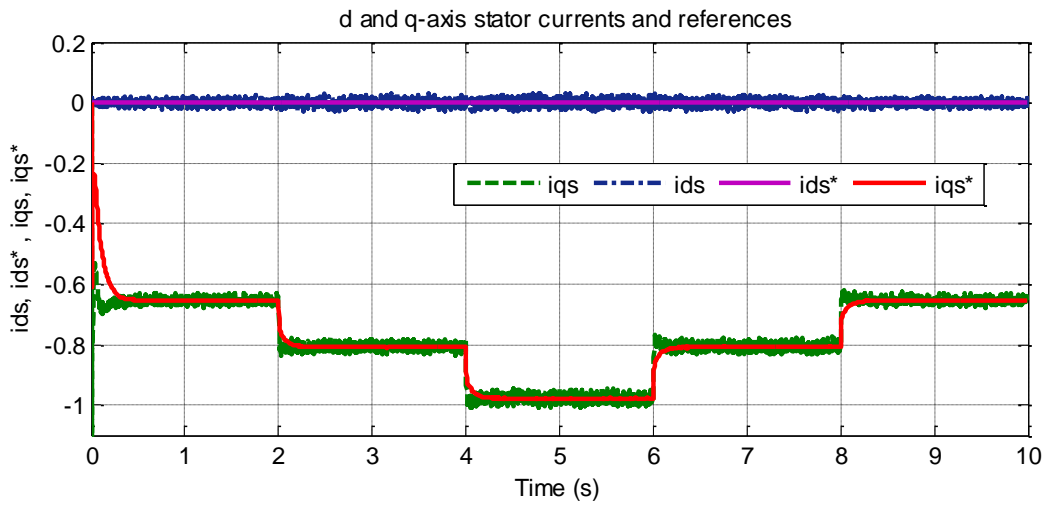


Figure 5.10: d and q-axis stator currents with references

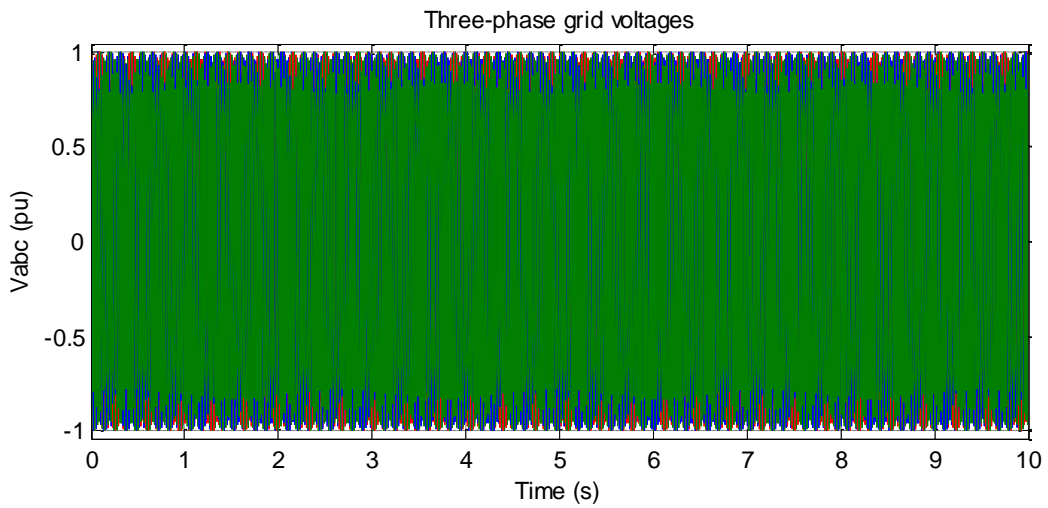


Figure 5.11: Three-phase grid voltages

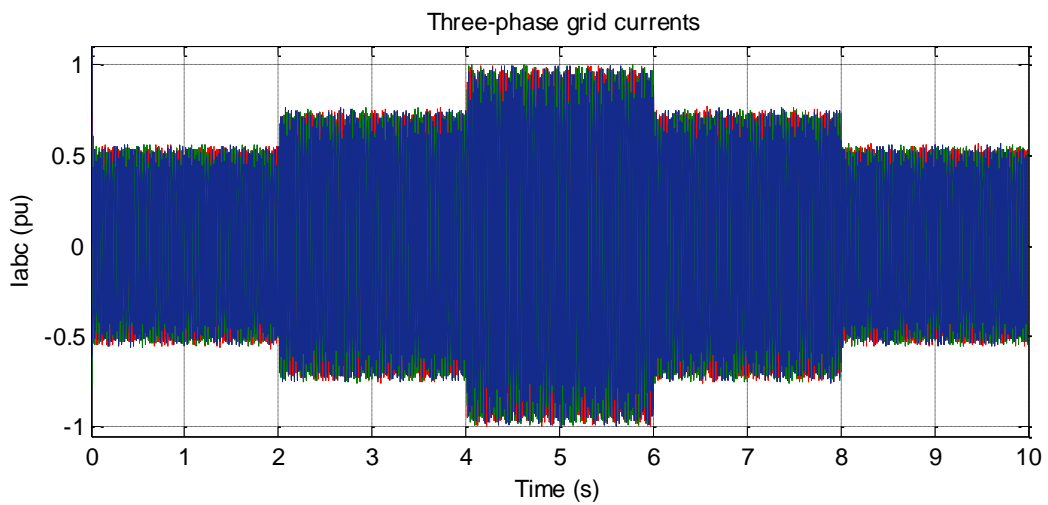


Figure 5.12: Three phase grid currents

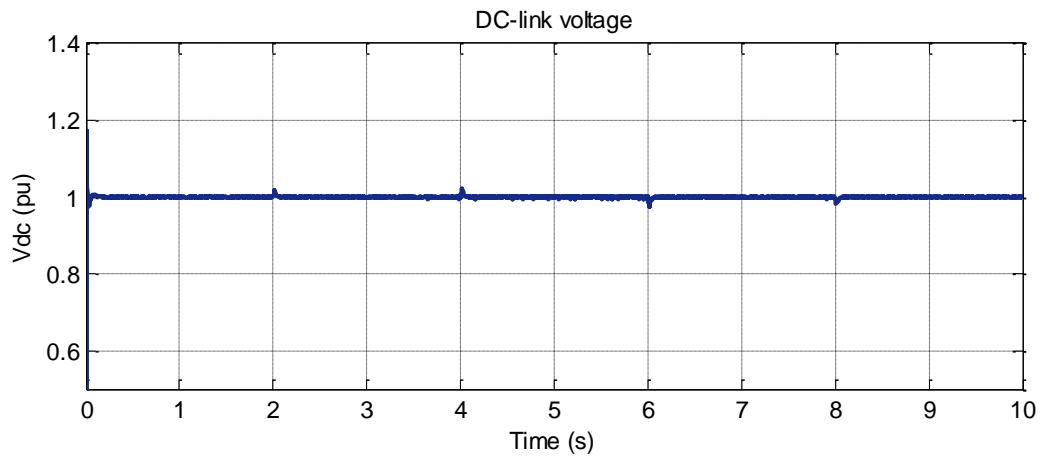


Figure 5.13: DC-link voltage

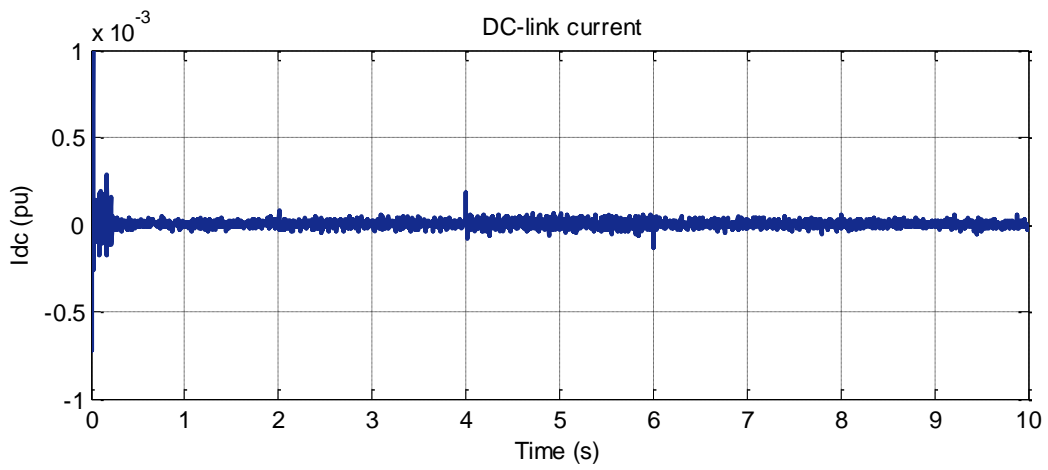


Figure 5.14: Current through DC-link

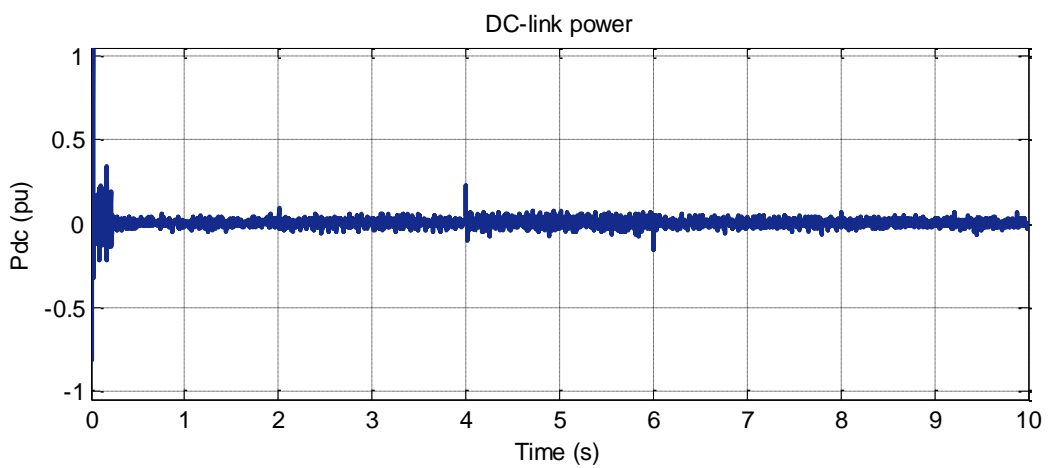


Figure 5.15: DC-link power

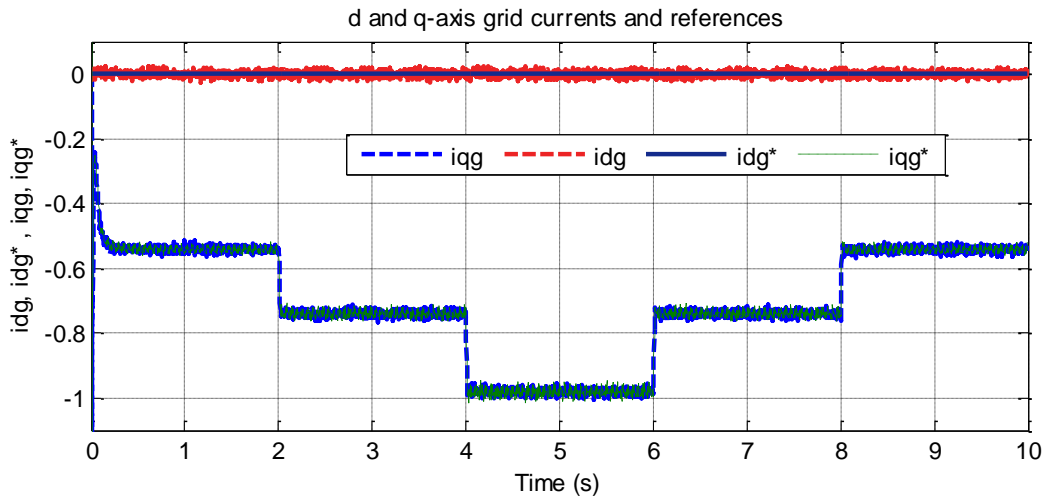


Figure 5.16: d and q-axis grid currents with references

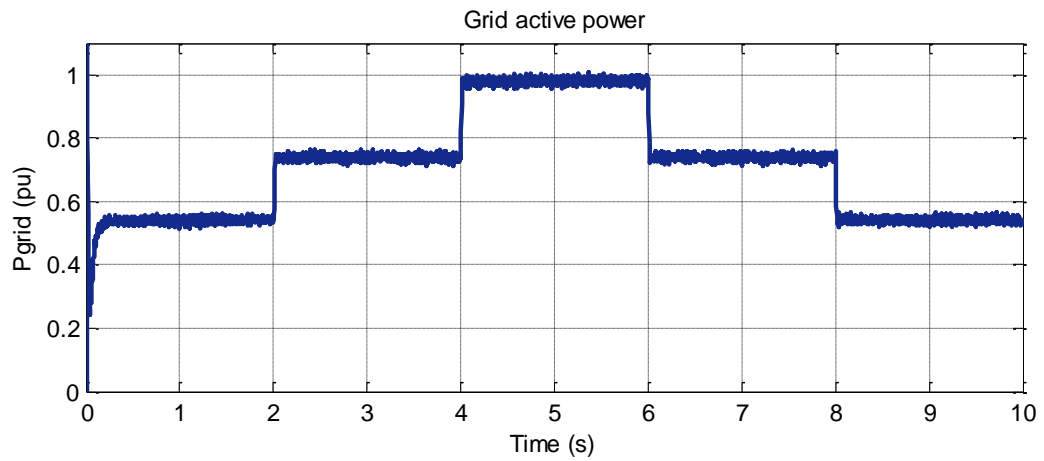


Figure 5.17: Grid active power

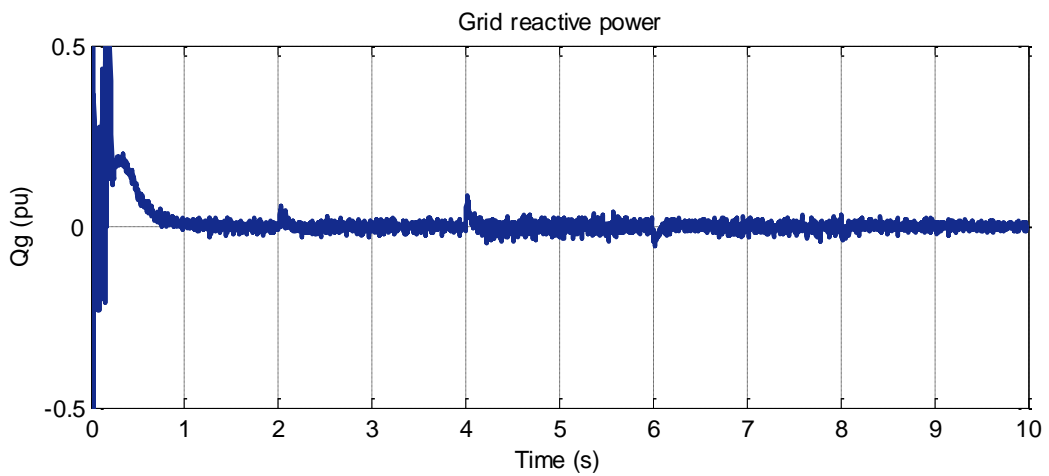


Figure 5.18: Reactive power to the grid

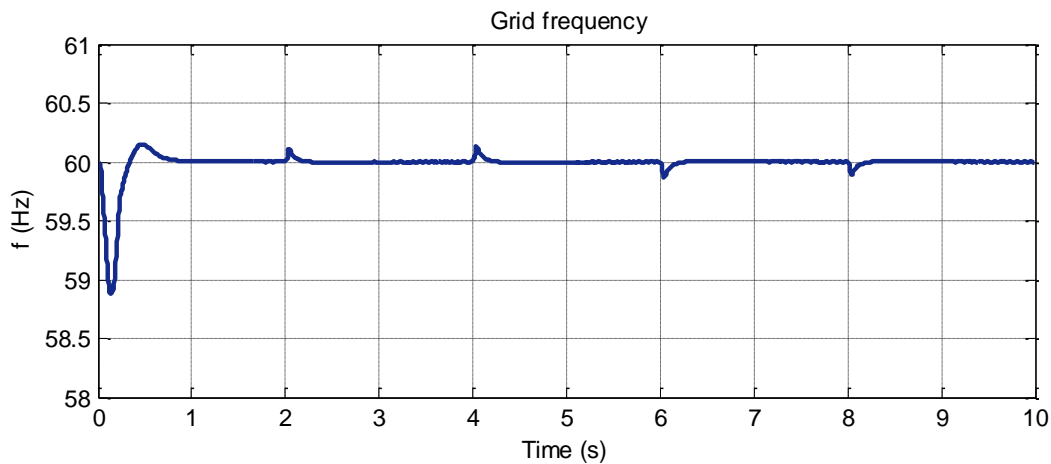


Figure 5.19: Grid frequency

On the grid side, magnitudes of the three-phase voltages are equal to 1 pu regardless of changes in wind speed, while the three-phase currents closely follow the grid active power depicted in Figure 5.17, as shown in Figures 5.11 and 5.12 respectively. This way, the DC-link voltage is directly proportional to the d-axis current as explained in section 4.4.2. Figure 5.13 shows the DC-link voltage response to the changes in wind speed.

Because the generator and the grid side converters are decoupled, and the DC-link is controlled from the grid side, the DC-link voltage is not expected to vary irrespective of changes in wind speed. Again, the controller does a great work in maintaining the DC-link value constant at its rated value. Figures 5.14 and 5.15 show that there is almost zero power flow into the DC-link capacitor, since the voltage is maintained nominal. The d and q-axis currents with their references are shown in Figure 5.16. As expected, these values closely follow their references. The q-axis is equal to zero, such that unity power factor is achieved. As a result, reactive power supplied to the grid is zero. The absolute values of the d-axis current are very close to the grid active power values as shown in Figure 5.18. Once more, this can be explained by Equation 4.31 in section 4.2.2. Finally, the grid frequency is also maintained constant as illustrated in Figure 5.19.

5.4 Simulation results under faulty conditions

5.4.1 Fault compensation

5.4.1.1 Pitch angle control

The aim of the pitch angle control is to minimize the extracted wind power when wind speeds are above rated value, but also to ensure maximum energy capture from the wind at lower and rated values. Normally, the pitch angle value is maintained at 0 degrees to satisfy the maximum energy capture but will increase as the rotational speed surpasses the nominal value.

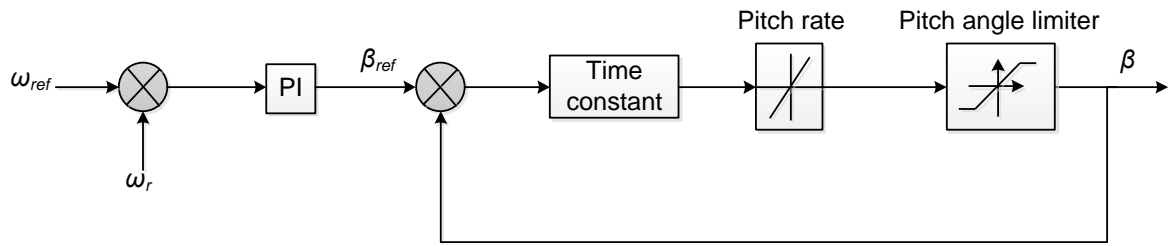


Figure 5.20: Block diagram of the pitch angle controller

Figure 5.20 represents a block diagram of the operation of the pitch angle control system. The reference rotor speed ω_{mref} is compared to the actual measured speed ω_m , and the error signal is sent to a PI controller to produce the reference pitch angle β_{ref} . This reference is in turn compared to the actual pitch angle value, and the error signal is used to correct the pitch angle to the desired value.

However, practically, the blade pitch angle rotation is limited in range and speed. The design therefore takes into consideration the actuators servo mechanism time constant, the pitch angle limits (0 to 30 deg) and rate of change (± 10 deg/s).

5.4.1.2 DC-link protection

During a grid fault, since the converters are decoupled, the DC-link capacitor will overcharge due to the continuous power supply from the generator. The braking resistor is used to dissipate this excess energy and thus keeping the DC-link and the converters safe. Normally, the DC-link voltage must be kept within the limits of the converters and the capacitor, which is around $\pm 25\%$ of its rated value, to avoid damage of the converters.

Assuming the converter operates at 100% of generator rated power, the braking resistor should be designed to dissipate rated power of the turbine and in this case its value would be equal to 0.96Ω . For the braking resistor's controller, in order to obtain worst case scenario results, the maximum allowable DC-link voltage is fixed to 1500V (1.25 pu) which corresponds to 25% of the rated DC-link voltage.

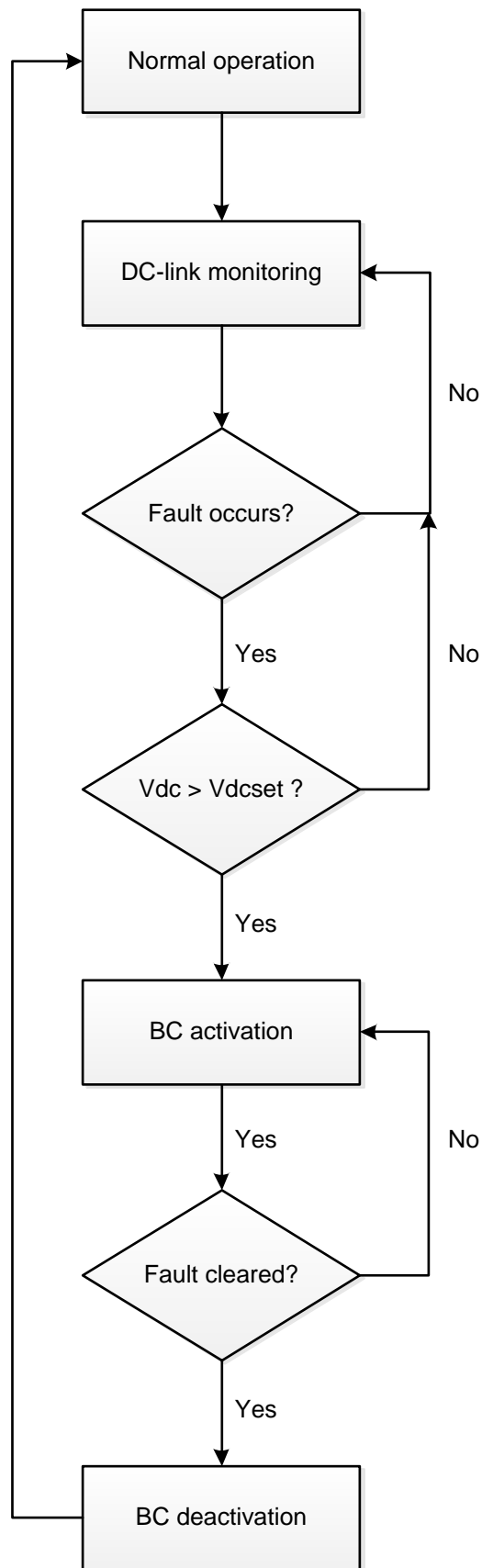


Figure 5.21: DC-link protection scheme

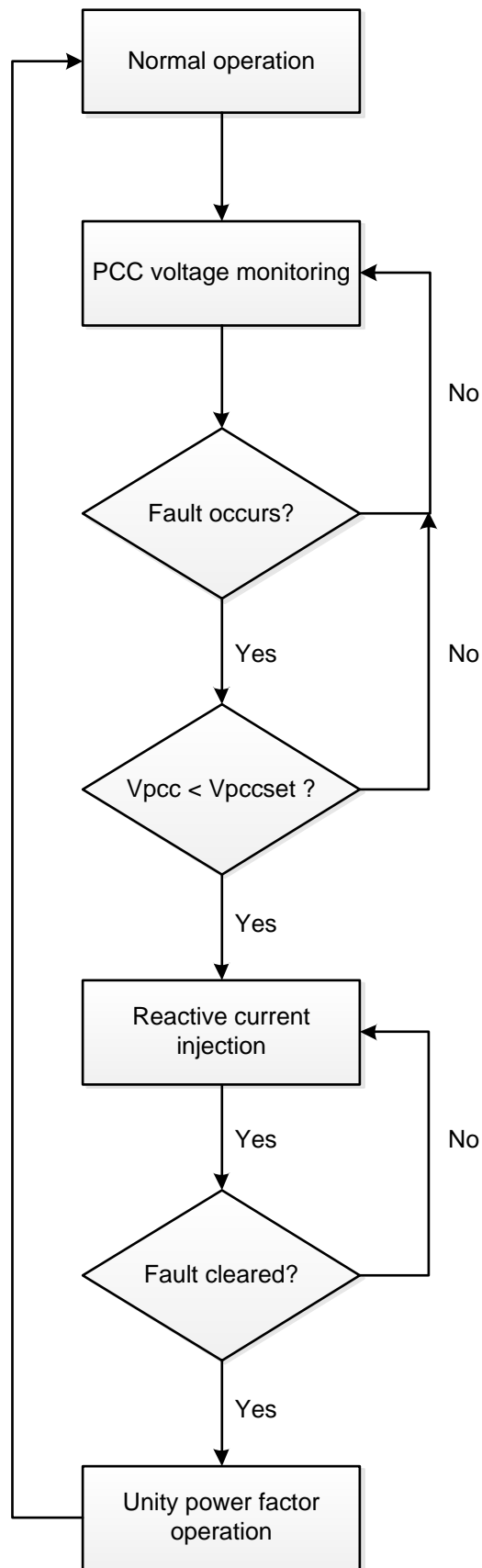


Figure 5.22: Grid reactive power support scheme

To control the switching of the resistor, the DC-link voltage value is measured and compared to a predefined value set not exceeding 1.2 pu. As long as the V_{dc} remains within the normal range, the controller sends a “0” signal and the braking resistor stays inactivated. Otherwise, a trip signal “1” is immediately sent to the resistor’s switch and the excess stator current starts flowing through the braking resistor instead of overcharging the capacitor. This control is illustrated in Figure 5.21 above.

5.4.1.3 Reactive power compensation

The reactive current support requirement during grid fault is presented in Figure 3.9 of section 3.1.5. As illustrated, when the grid voltage is comprised between 0.9 p.u and 1.1 p.u, no reactive power compensation is necessary. That portion corresponds to area A. For grid voltages below 0.9 p.u down to 0.5 p.u, reactive current injection is required to increase as a function of the dip level, constituting area B. Finally in area C (for grid voltages below 0.5 p.u) 100 percent reactive current contribution expected. Figure 5.22 above shows the flow diagram of how LVRT compensation is achieved.

5.4.2 Case studies for simulations under grid faults

To assess the effectiveness and robustness of the wind farm system to comply with the LVRT requirements presented earlier in section 3.1, different case scenarios are considered. These different scenarios are classified according to the location, the type, the dip level and duration, and eventually the wind speed conditions. The results are also compared depending on whether reactive current is injected according to Figure 3.9 to support grid recovery or not, for the different LVRT methods tested.

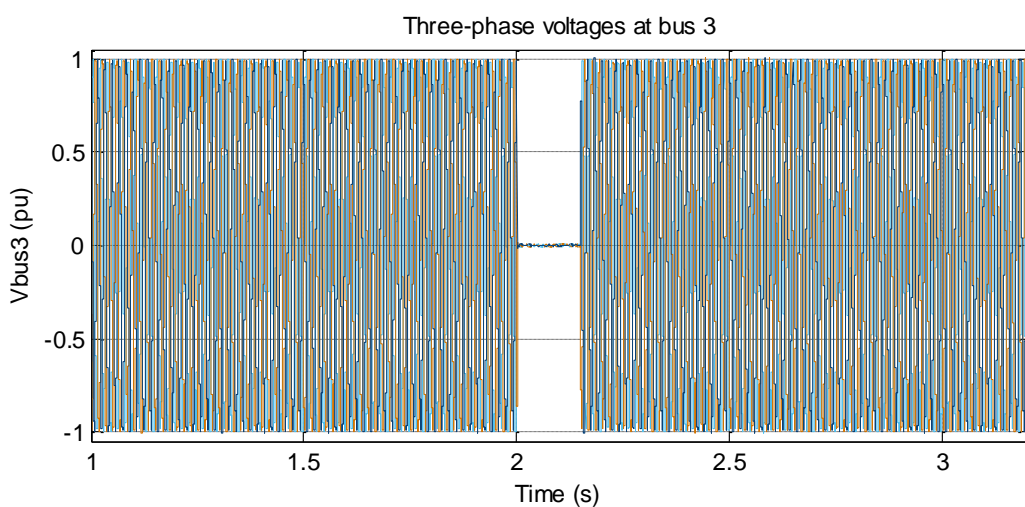


Figure 5.23: Voltage profile during fault at bus 3 for case 1

5.4.2.1 Case 1: Full power, 100% three-phase voltage dip at bus 3, fault duration 150 ms.

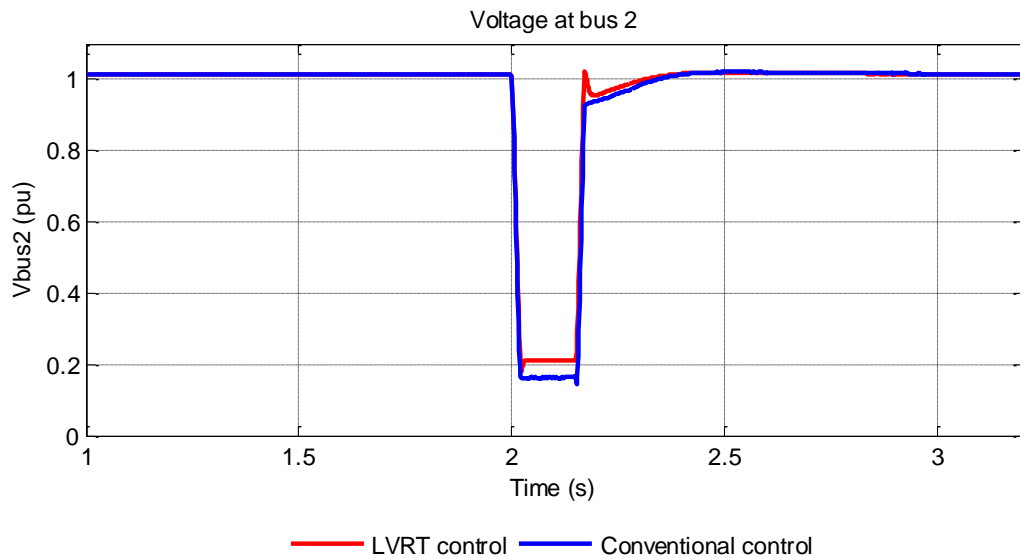


Figure 5.24: Voltage profile at PCC during grid fault for case 1

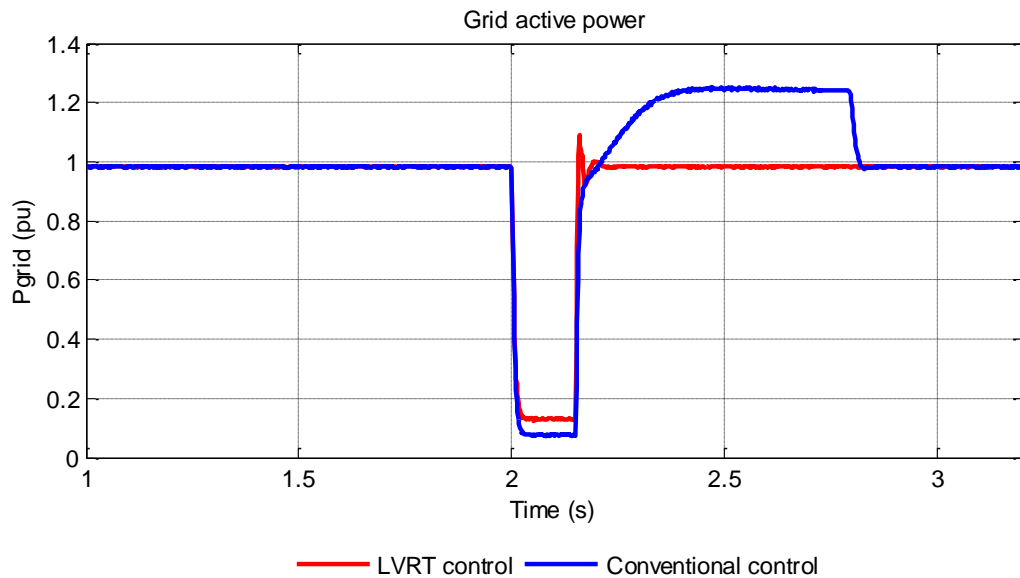


Figure 5.25: Grid active power output during grid fault for case 1

The results for the first case scenario are displayed in Figure 5.23, Figure 5.24, Figure 5.25 and Figure 5.26. A three-phase fault at bus 3 is introduced at time $t = 2$ s, for a duration of 150 ms. Figure 5.23 shows the voltage drop at bus 2 (PCC). With the conventional control, the voltage drops to about 0.16 p.u. This value is improved to 0.21 p.u. when the LVRT control is activated. The grid active power also experiences an improvement from 0.08 p.u. with the conventional control, up to 0.13 p.u. with the LVRT control, as depicted in figure 5.24.

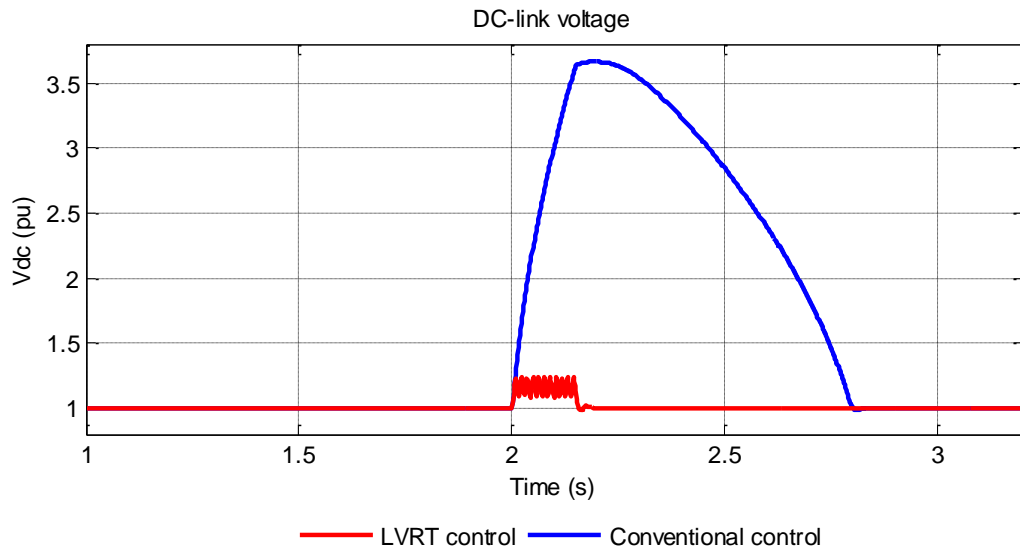


Figure 5.26: DC-link voltage during grid fault for case 1

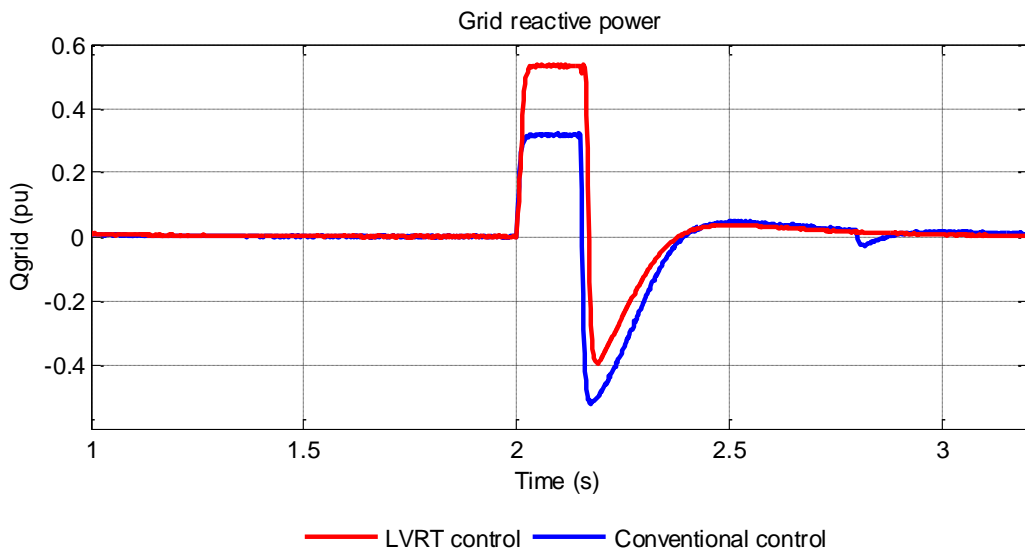


Figure 5.27: Grid reactive power output during grid fault for case 1

Moreover, after fault clearance and under conventional control, the active power to the grid reaches about 1.25 p.u and is maintained at that value until time $t = 2.8$ s, before dropping back to nominal value. This situation can be explained from the DC-link behaviour as illustrated in Figure 5.26. During the fault duration, the generator's speed is not affected by the low voltage condition on the grid side due to the decoupled nature of the controllers, causing the DC-link to rise uncontrollably when no additional action is applied as explained in section 3.2. As a result, the DC-link voltage rises up to a value of about 3.81 p.u. After fault clearance, the DC-link voltage decreases progressively until it reaches back its nominal value of 1 p.u at time $t = 2.8$ s. During this recovery time, the surplus power stored in the DC-

link is injected to the grid in addition to the generated active power. Using the LVRT control during fault, the DC-link voltage oscillates between 1.1 p.u and 1.25 p.u which correspond to about 1320 and 1500 Volts respectively. Within these limits, the DC-link capacitor is safe from overcurrent and thus from eventual damage. The reactive power injected to the grid is illustrated in figure 5.27. To support the PCC voltage recovery, reactive power reaches 0.54 p.u when the LVRT control is applied, whereas this value only reaches 0.3 p.u under conventional control.

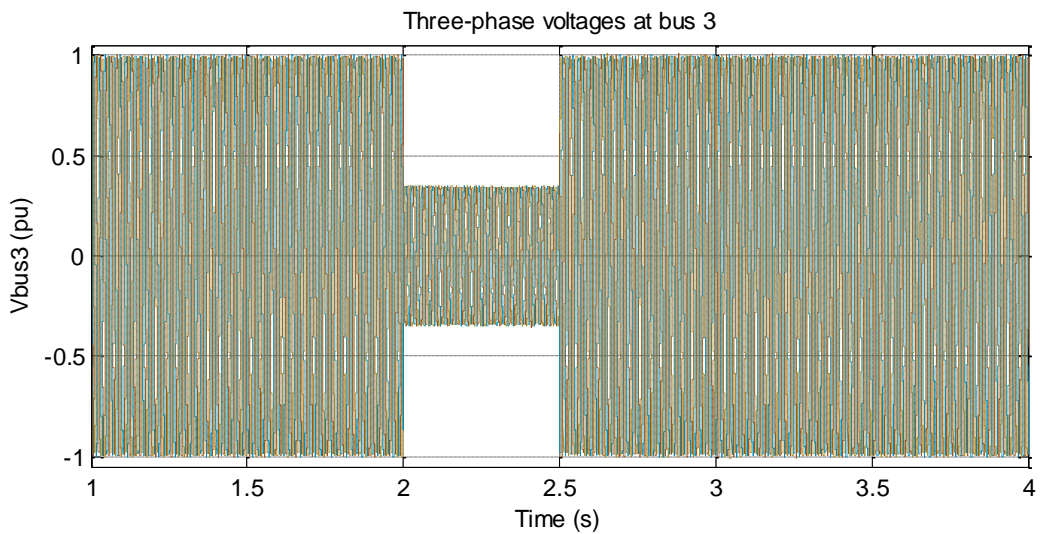


Figure 5.28: Voltage profile during fault at bus 3 for case 2

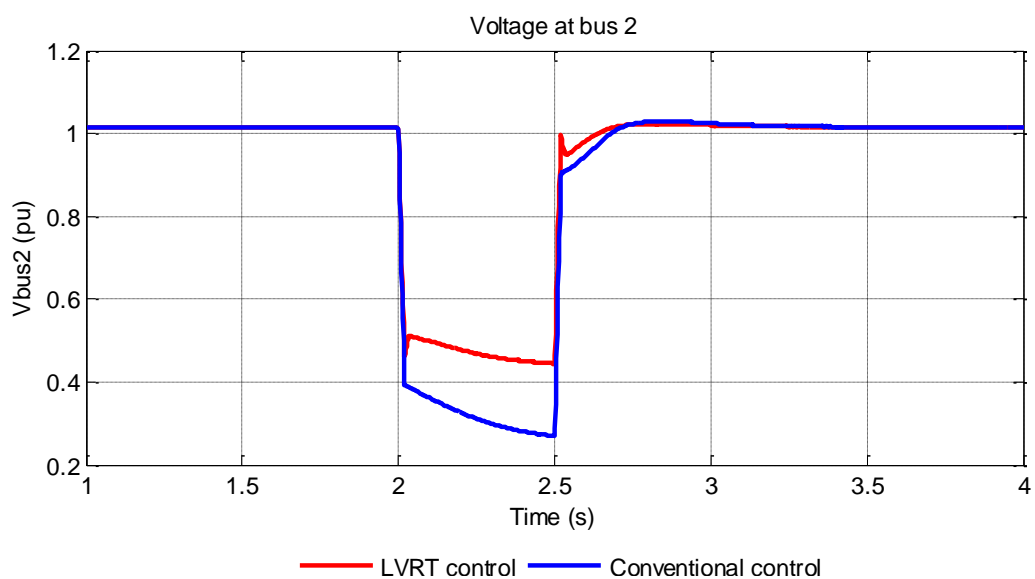


Figure 5.29: Voltage profile at PCC during grid fault for case 2

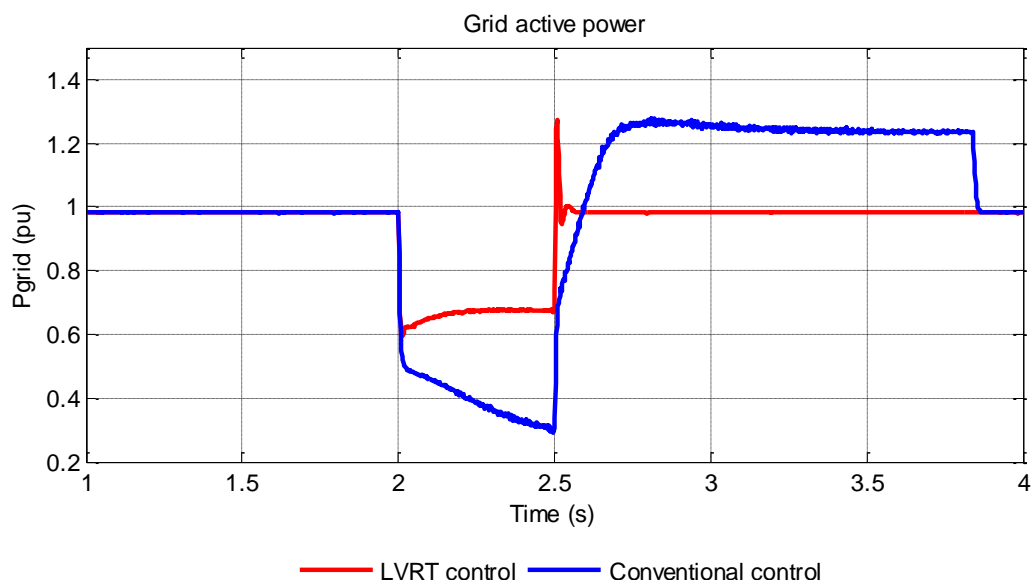


Figure 5.30: Grid active power output during grid fault for case 2

5.4.2.2 Case 2: Full power, 65 % three-phase voltage dip at bus 3, fault duration 500 ms.

In this case, a 500 ms three-phase fault, with an amplitude of 0.65 p.u is applied at bus 3 as illustrated in figure 5.28, at rated wind speed. Figure 5.29 depicts the behaviour of the voltage at bus 2 during grid fault under the conditions specified in case 2. With the conventional control, the PCC voltage drops directly to 0.4 p.u then continues to further decrease to 0.28 p.u until the fault is cleared. However, with the LVRT control, the PCC voltage curve shows a considerable improvement with values between 0.45 p.u and 0.5 p.u during the voltage drop. In Figure 5.30, the active power responses of both controls are presented. The active power to the grid shows a similar response to the PCC voltage. Under conventional control, this power suddenly drops to 0.5 p.u directly at fault occurrence, followed by a continuous decrease up to 0.28 p.u at fault clearance. Again, there is a limitation to about 1.25 p.u during the whole DC-link recovery time. However, the active power drop during the fault is improved to about 0.68 p.u when the LVRT control is activated, and recovery to rated value is almost instantaneous after the fault is removed. In Figure 5.31, the DC-link voltage is presented. Without LVRT compensation, the DC-link voltage rises even more than in case 1 (5.4 p.u against 3.81p.u), while the capacitor's discharge time at fault clearance is also increased from 650 ms in case 1 to 1200 ms in the current case, which is understandable because of the increased fault duration. On the other hand, DC-link protection is satisfactorily achieved under LVRT control and the values are maintained within acceptable limits as in the previous case. The reactive power shown in Figure 5.32 peaks to 0.2 p.u immediately when the fault occurs then ramps down to 0 pu with the conventional controller, due to the lower grid voltage dip. With the LVRT control, this value peaks at 0.76

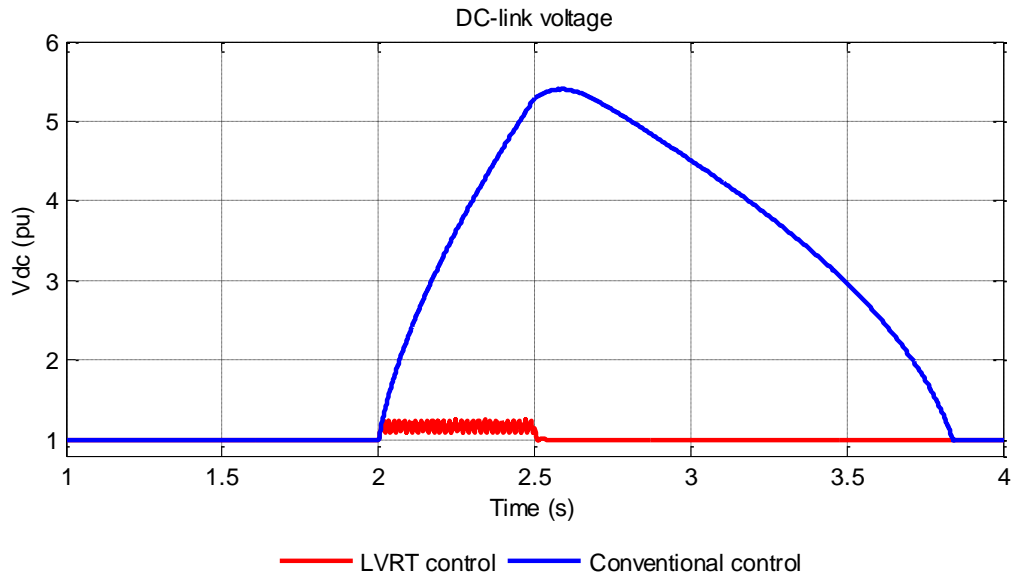


Figure 5.31: DC-link voltage during grid fault for case 2

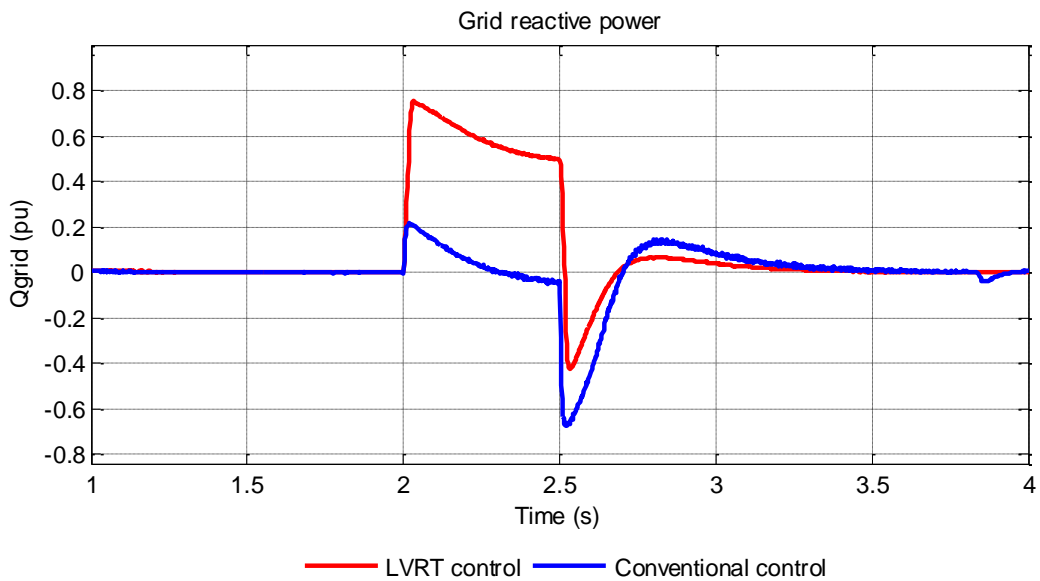


Figure 5.32: Grid reactive power output during grid fault for case 2

pu showing that more reactive power is injected for grid support in this case compared to the previous one, as expected from the reactive power requirement.

5.4.2.3 Case 3: Full power, 25 % three-phase voltage dip at bus 3, fault duration 1500 ms.

A 25 % three-phase grid voltage drop lasting 1.5 s is applied at bus 3 as shown in Figure 5.33. This time the fault level is reduced, however the duration is much prolonged. The PCC voltage depicted in Figure 5.34 dips down to 0.75 p.u under conventional control, and 0.81 p.u when the LVRT control is applied, showing a voltage contribution of about 0.06 p.u.

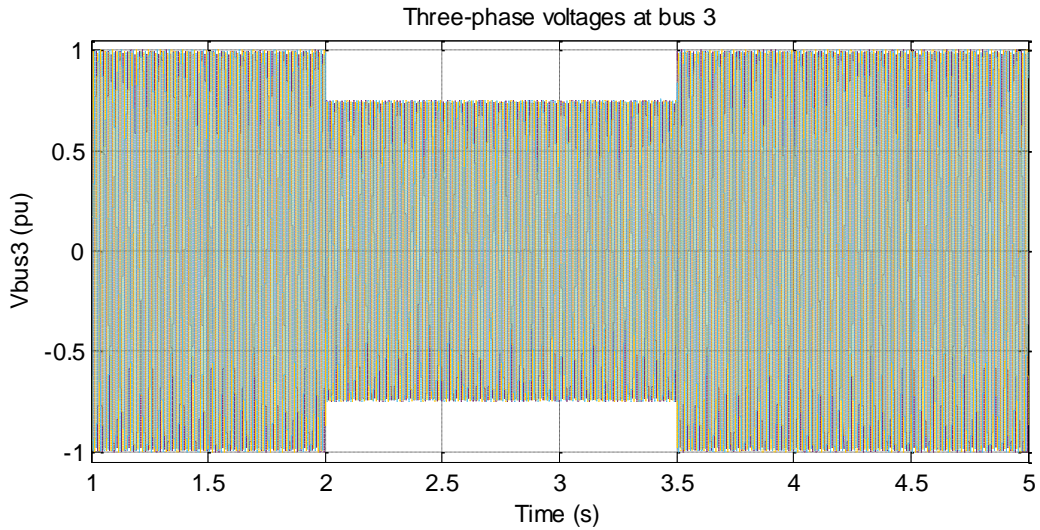


Figure 5.33: Voltage profile during fault at bus 3 for case 3

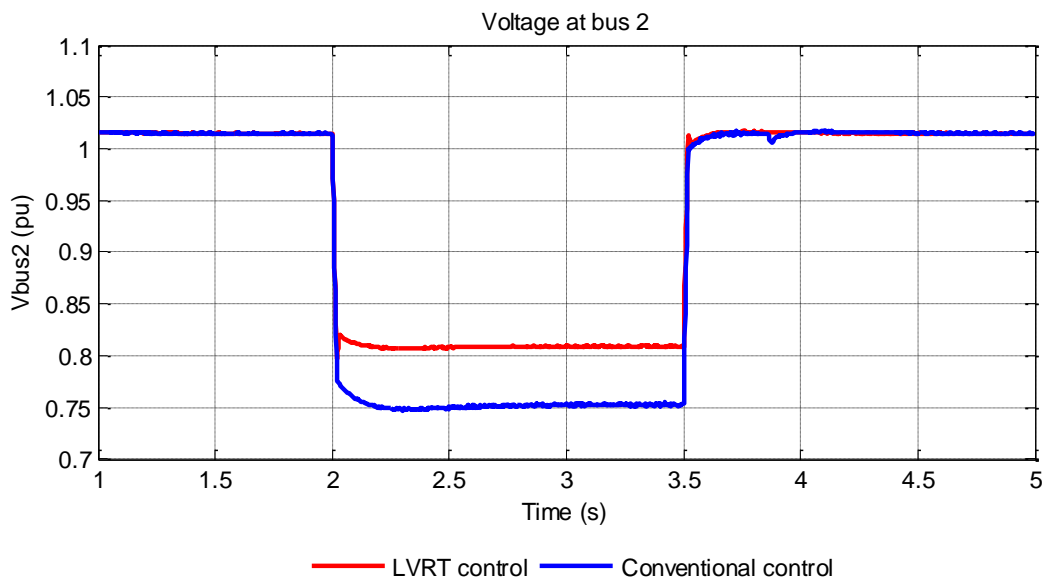


Figure 5.34: Voltage profile at PCC during grid fault for case 3

As shown in Figure 5.35, the grid active power only drops to 0.92 p.u during fault, but still overshoots at fault clearance to 1.25 p.u as in the previous cases, although in this case the power remains to that value for about 350 ms only. With the LVRT control, the active power does not deviate from the nominal value during fault, and the overshoot is also eliminated at fault clearance. The DC-link voltage rises up to 3 p.u during the fault, then takes about 350 ms dropping back to nominal value as shown in Figure 3.36. This recovery time is considerably short compared to the previous two cases certainly because of the much lower voltage dip and also the longer fault duration in this case. However under LVRT control, the DC-link voltage is maintained constant at 1 p.u during the grid voltage dip. As a result, the

protection switch is not triggered and no excess power is dissipated by the braking resistor. In Figure 5.37, the grid reactive power contribution during fault is presented. With no reactive current injection, the reactive power support to the grid is minimal (0 p.u) for the essential of the fault duration. When reactive current is injected, the reactive power contributes to about 0.33 p.u, resulting in an improvement in PCC voltage recovery.

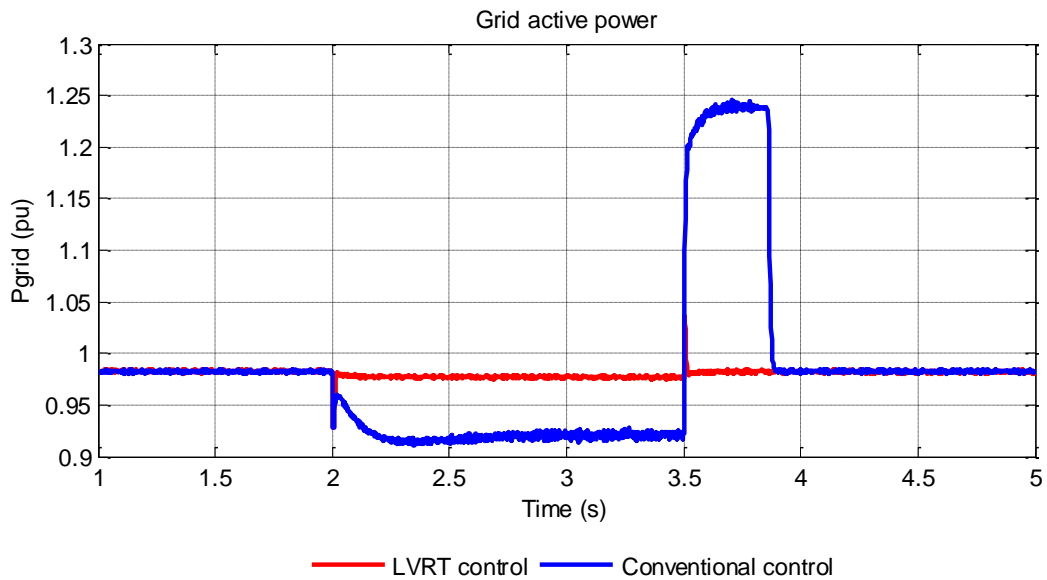


Figure 5.35: Grid active power output during grid fault for case 3

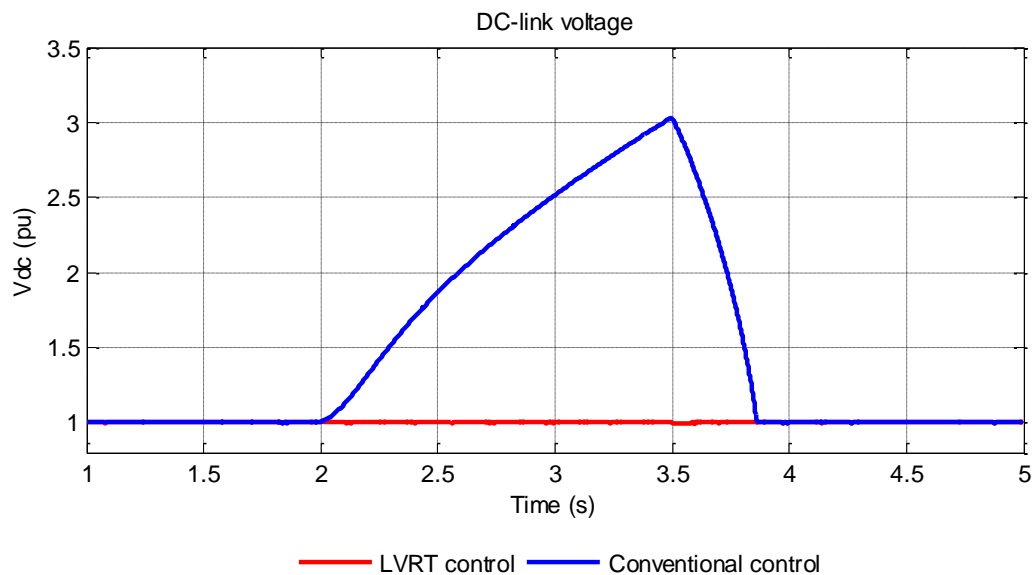


Figure 5.36: DC-link voltage during grid fault for case 3

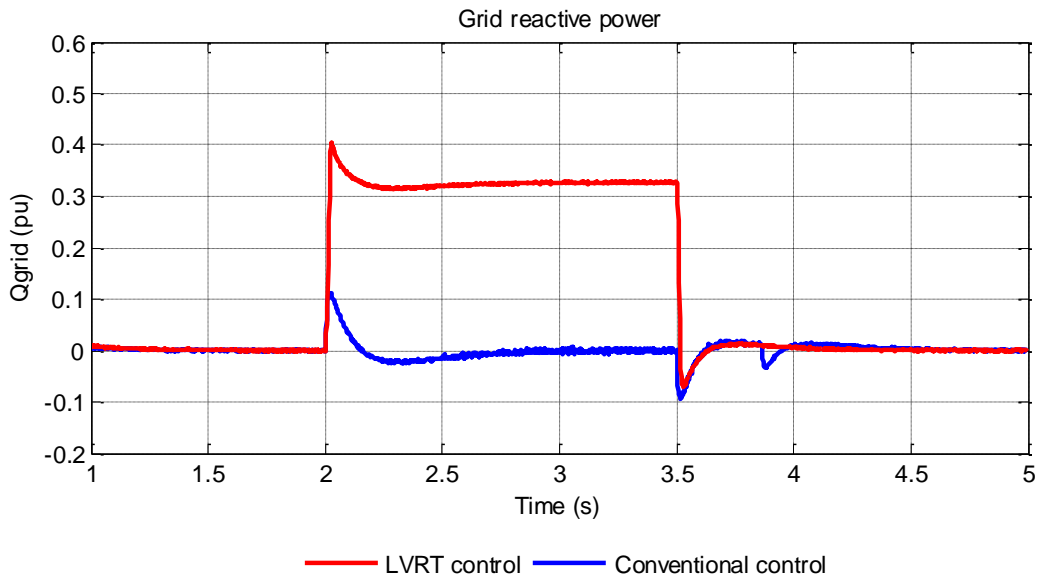


Figure 5.37: Grid reactive power output during grid fault for case 3

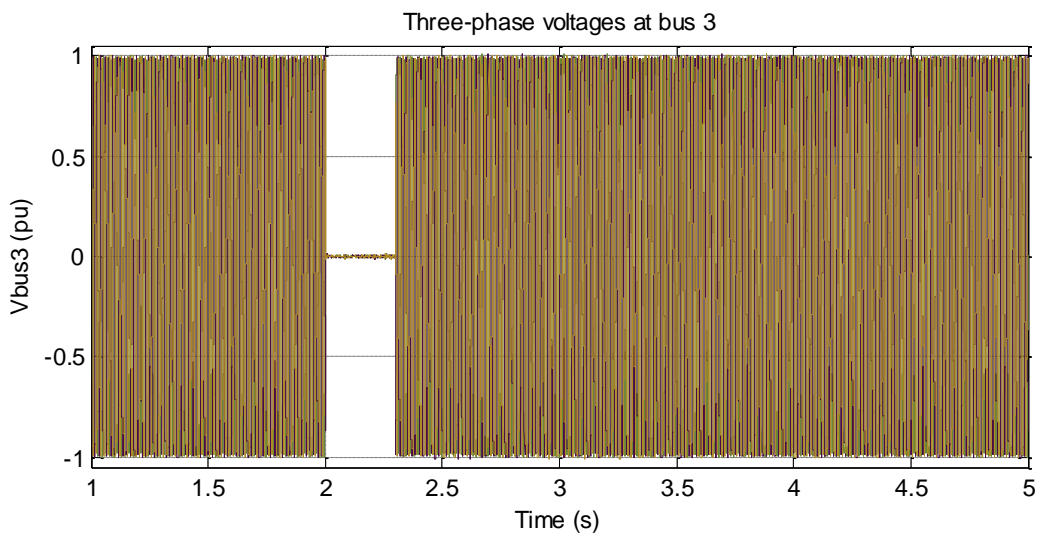


Figure 5.38: Voltage profile during fault at bus 3 for case 4

5.4.2.4 Case 4: Full power, 100% three-phase voltage dip at bus 3, fault duration 300 ms

For the fourth case scenario, the fault duration is extended to 300 ms for a voltage drop down to 0 p.u, to evaluate the response of the system during a more severe fault as illustrated in Figure 5.38. In Figure 5.39, when no reactive current is injected, the PCC voltage drops to 0.16 p.u. At fault clearance, the PCC voltage experiences a quick undershoot to about 0.05 p.u for less than 1 ms, before returning to normal operating region. Under these conditions, the PCC voltage would fall outside the limits of the LVRT curve presented in Figure 3.8 of section 3.1.5. With LVRT control, the PCC voltage improves to

0.21 p.u as in case 1. The undershoot is cleared, and the voltage profile falls back into the LVRT curve limits. The grid active power in case 4 is shown in Figure 5.40. As in case 1, the active power to the grid drops to 0.08 p.u under normal control. However at fault clearance, its value quickly drops to 0 p.u, then ramps up to 1.25 p.u where it remains for 2 s before reaching back nominal power. When LVRT control is employed, the drop is improved to 0.13 p.u and recovery after fault clearance is fast but not immediate, since there is a short transient before ramping back to the normal operating state.

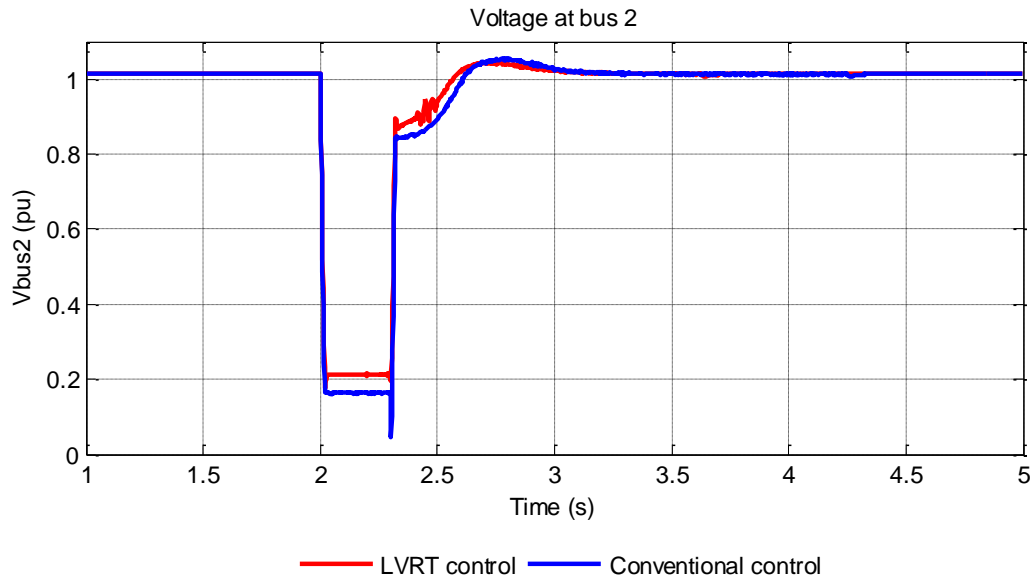


Figure 5.39: Voltage profile at PCC during grid fault for case 4

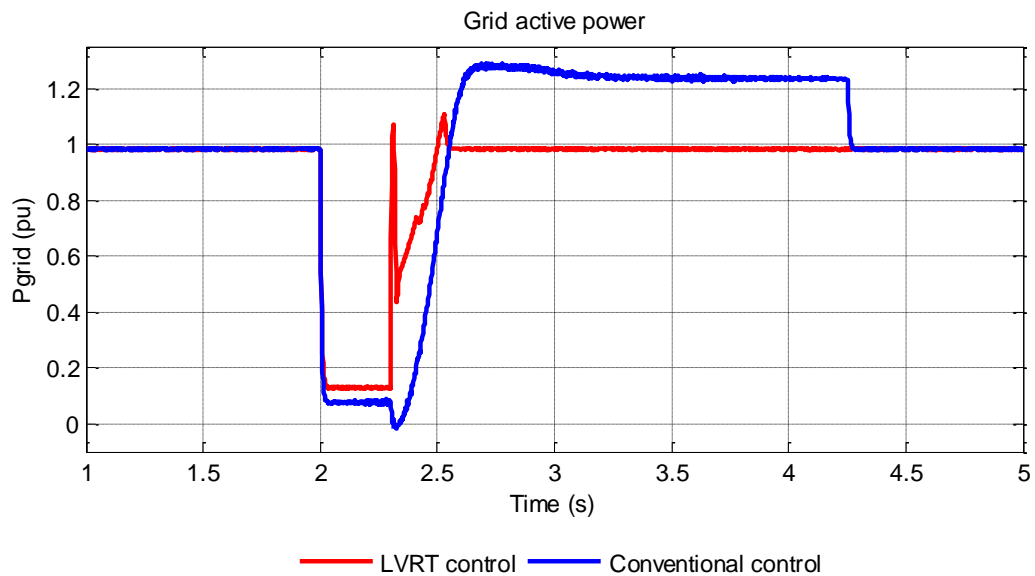


Figure 5.40: Grid active power output during grid fault for case 4

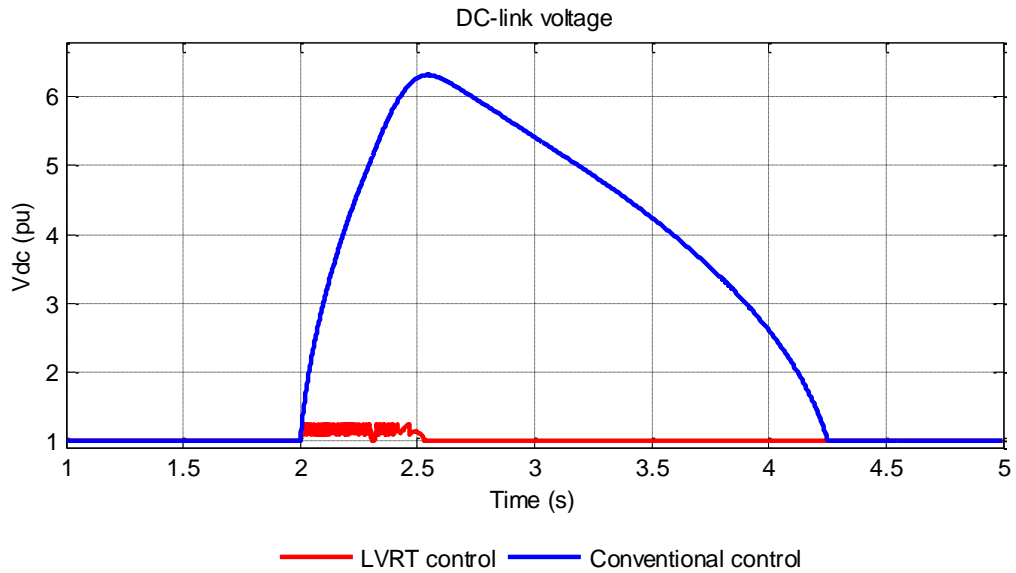


Figure 5.41: DC-link voltage during grid fault for case 4

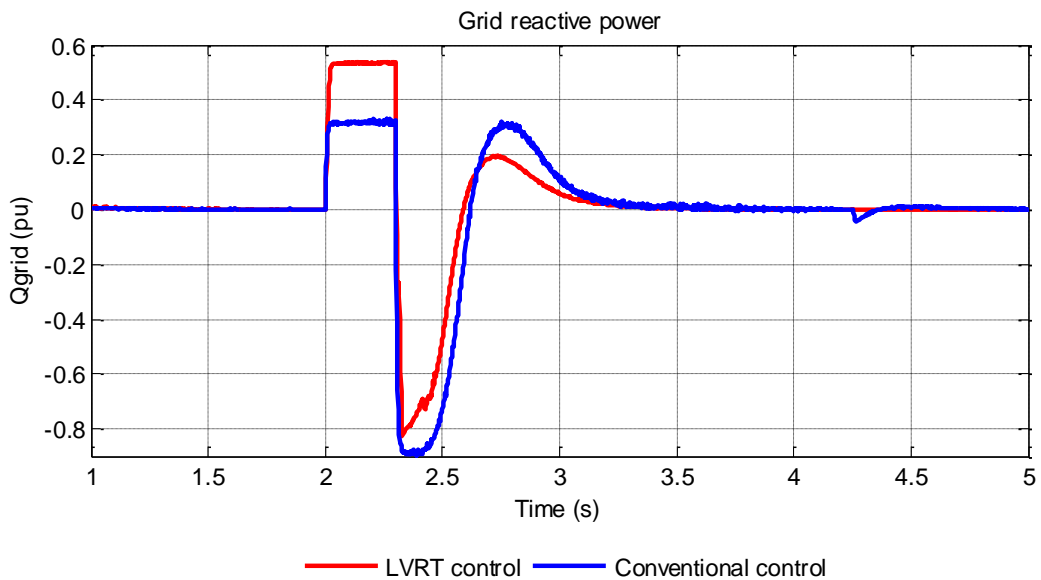


Figure 5.42: Grid reactive power output during grid fault for case 4

For the DC-link voltage depicted in Figure 5.41, its value peaks to about 6.4 p.u during fault and takes almost 2 s to recover after the fault is cleared, which is understandable looking at the depth and the duration of the fault. Under LVRT control, the DC-link voltage is controlled not to exceed 1.2 p.u successfully. The reactive power contribution is the same as case 1 for both conventional and LVRT controls as illustrated in Figure 5.42, meanwhile, it can be noted pronounced undershoots down to almost -1 p.u at fault disposal.

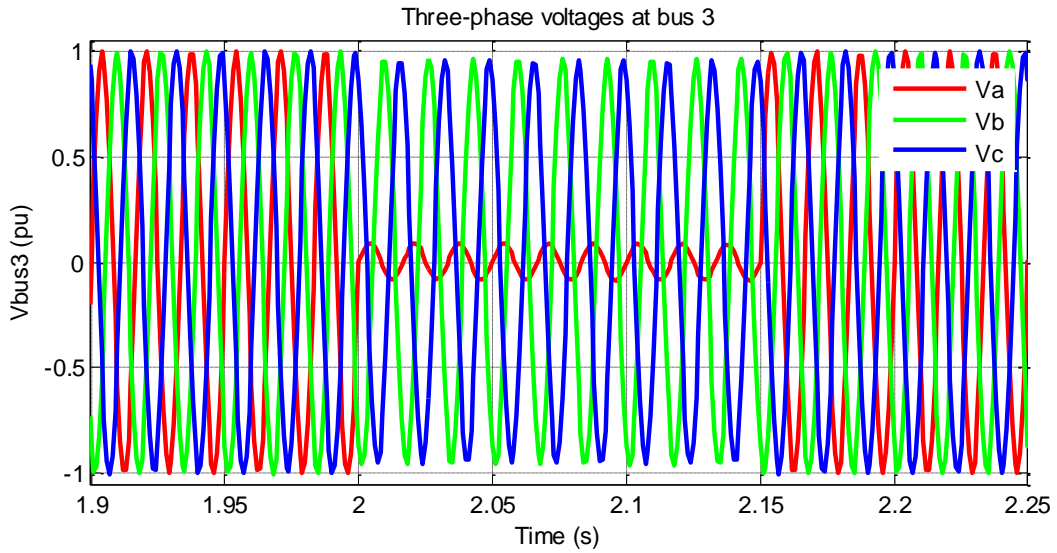


Figure 5.43: Voltage profile during fault at bus 3 for case 5

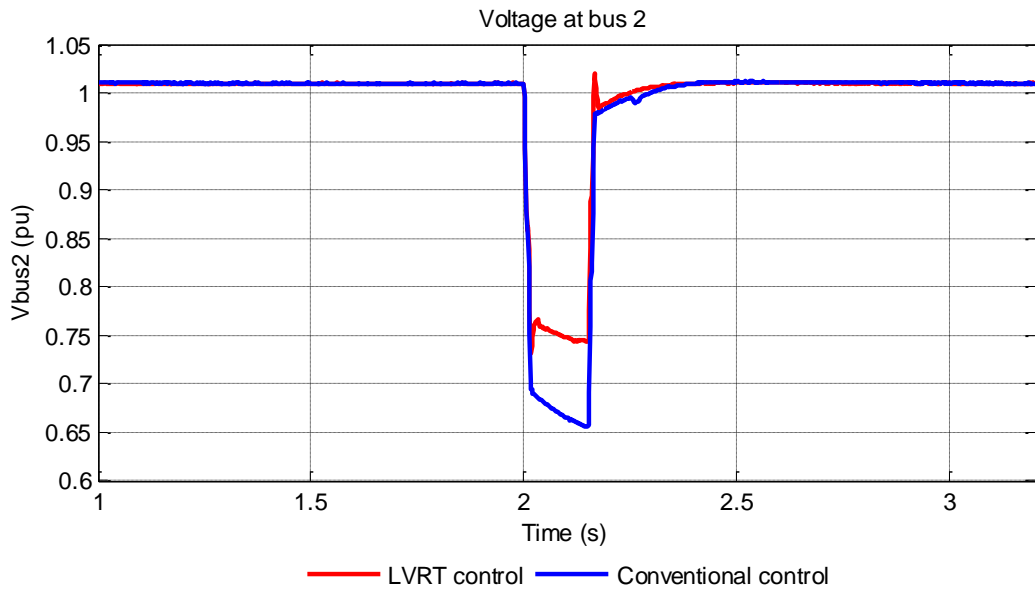


Figure 5.44: Voltage profile at PCC during grid fault for case 5

5.4.2.5 Case 5: Full power, 100% single line to ground voltage dip at bus 3, fault duration 150 ms

In the fifth case scenario, a single-phase to ground fault is applied at bus 3 for 150 ms. The single line fault is normally a less severe type because the other two phases can still compensate for the one phase loss and operate safely without causing major disturbances. Figure 5.43 shows how phase A drops down to about 0.1 p.u, while phases B and C remain close to 1 p.u during the fault time interval from 2s to 2.15s.

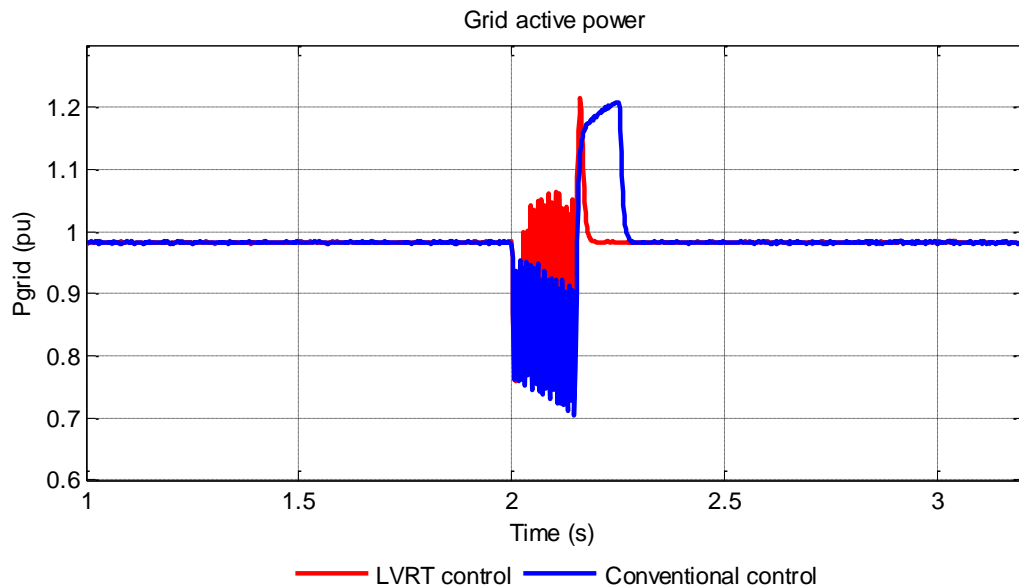


Figure 5.45: Grid active power output during grid fault for case 5

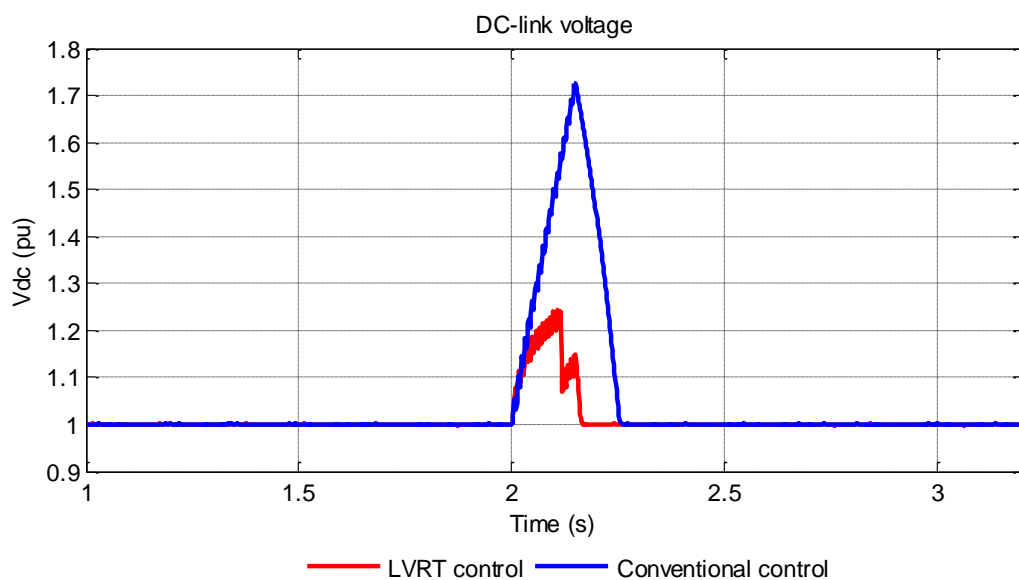


Figure 5.46: DC-link voltage during grid fault for case 5

The PCC voltage is presented in Figure 5.44 above. With the conventional control, the voltage drops to almost 0.65 p.u during fault. Note that the voltage does not drop to values close to 0 p.u since only one phase is affected as mentioned earlier. However, the voltage drop is improved by 0.1 p.u to reach around 0.75 p.u when reactive current is injected for grid recovery support. Without LVRT compensations, the active power drop during fault reaches 0.75 p.u, then rises up to 1.2 p.u as in the previous cases, but the discharge time is shorter this time around 0.1s. When LVRT control is employed, the active power remains around 1 p.u during the fault as illustrated in Figure 5.45. The DC-link voltage depicted in Figure 5.46 rises to only 1.7 p.u under conventional control which is considerably low compared to the

other previous cases. In fact, since the other two phases are still operating, the grid side converter is still capable of exporting most of the turbine's power to the grid during the fault. As a result, DC-link overcharge is reduced. Meanwhile, when reactive current is injected during fault, it can be observed that the DC-link voltage rise is below 1.25 p.u, and therefore there is no need to activate the braking resistor under LVRT control. The reactive power support is displayed in Figure 5.47, for both the conventional and LVRT controls.

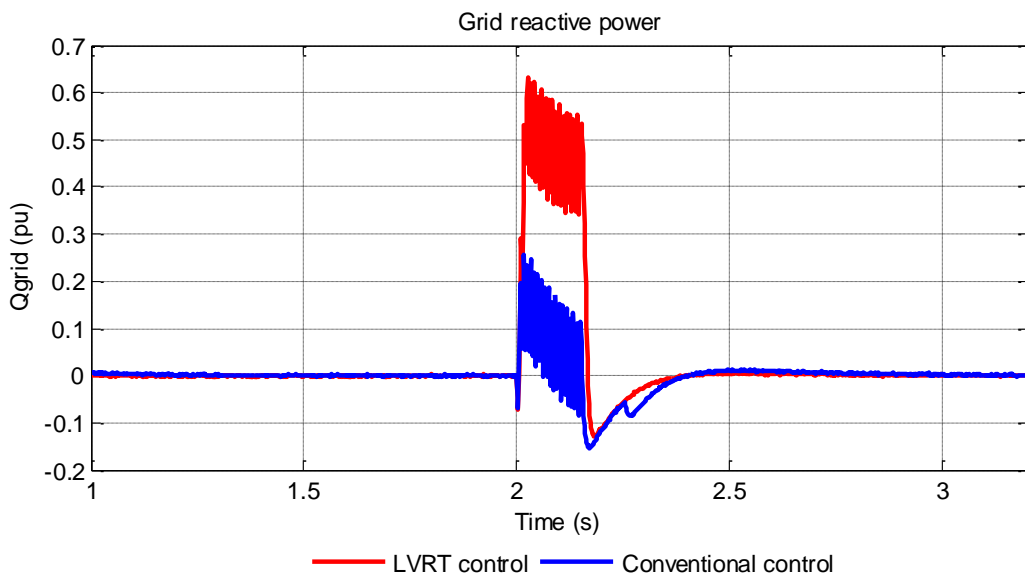


Figure 5.47: Grid reactive power output during grid fault for case 5

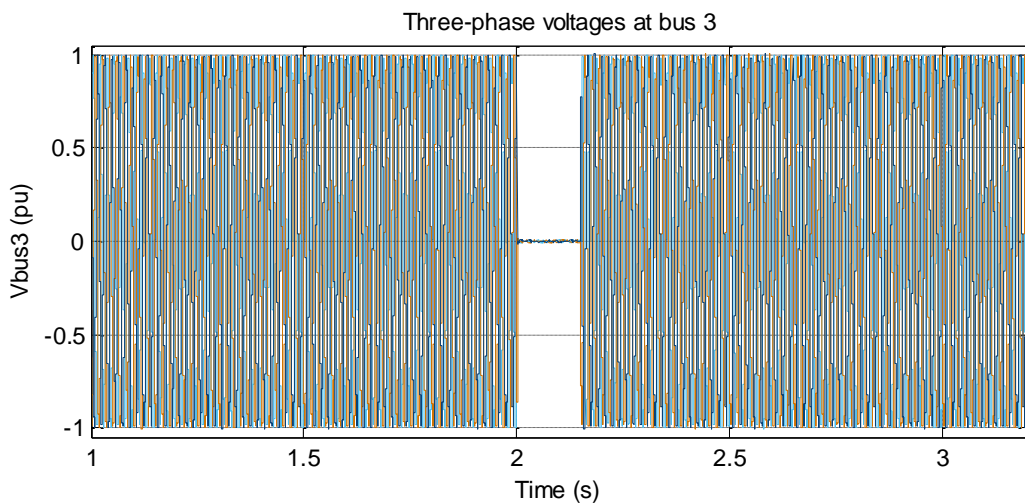


Figure 5.48: Voltage profile during fault at bus 3 for case 6

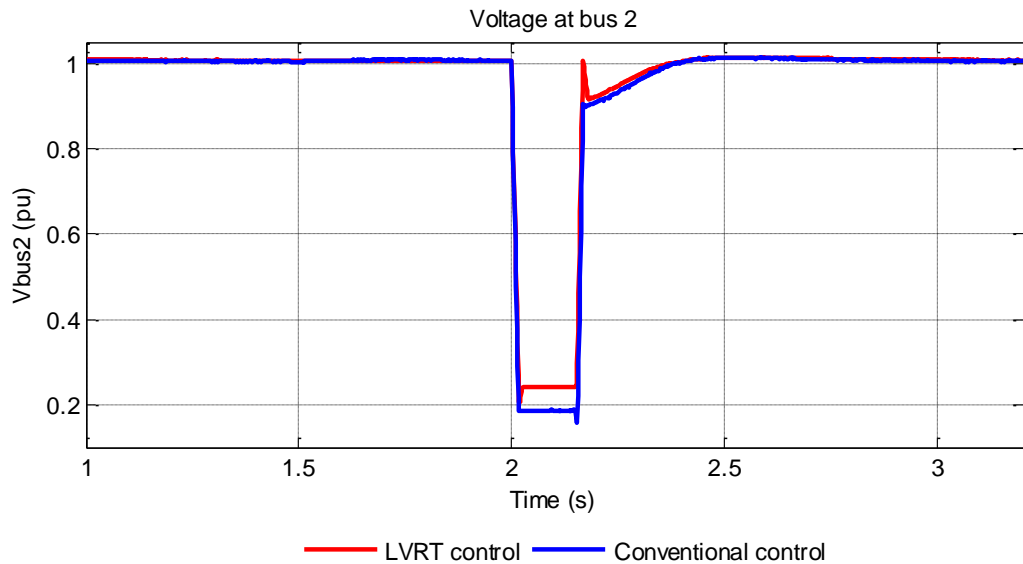


Figure 5.49: Voltage profile at PCC during grid fault for case 6

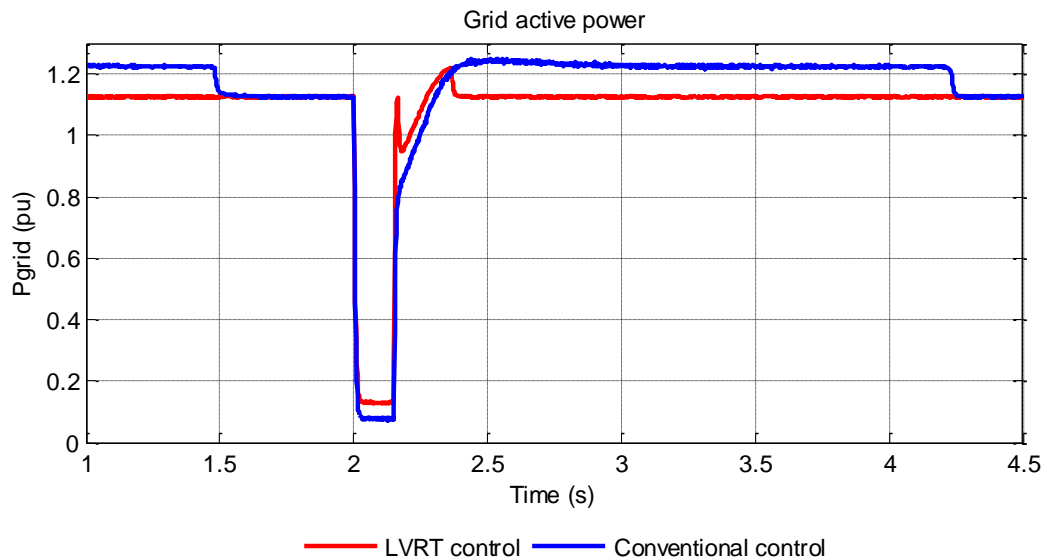


Figure 5.50: Grid active power output during grid fault for case 6

5.4.2.6 Case 6: 100% three-phase voltage dip at bus 3, fault duration 150 ms, at wind speed 14 m/s

Case 6 is similar to case 1, on the difference that this time around the wind farm operates at above rated wind speed (14 m/s). The results in Figure 5.49 for the voltage at PCC are the same as for the first case scenario. The active power to the grid is displayed in Figure 5.50. The pitch control contributes in keeping the turbine’s power under reasonable limits. Under normal control, the active power drops to 0.08 p.u during fault and stays at 1.2 p.u after the fault is cleared for about 2 s before restoration to nominal power. When the LVRT control is applied, the power drop is reduced to 1.2 p.u. The braking resistor absorbs all the excess

power, keeping the active power at rated value after the fault is cleared. The DC-link voltage is shown in Figure 5.51. When no protection measure is taken, the DC-link rises up to 4.2 p.u and the discharge time is about 2 s. However, the charge of the DC-link capacitor could be limited with the help of the pitch controller. With the use of the braking chopper, the DC-link is controlled to remain within the operating limits although there is a little struggle to return to rated value after fault clearance, compared to the previous cases. Reactive power contribution during fault has also improved compared to case 1, with 0.38 p.u in this case against 0.3 p.u in case 1 under conventional control mode, and 0.6 p.u against 0.54 p.u when the LVRT control is used. Figure 5.52 shows the reactive power to the grid for case 6.

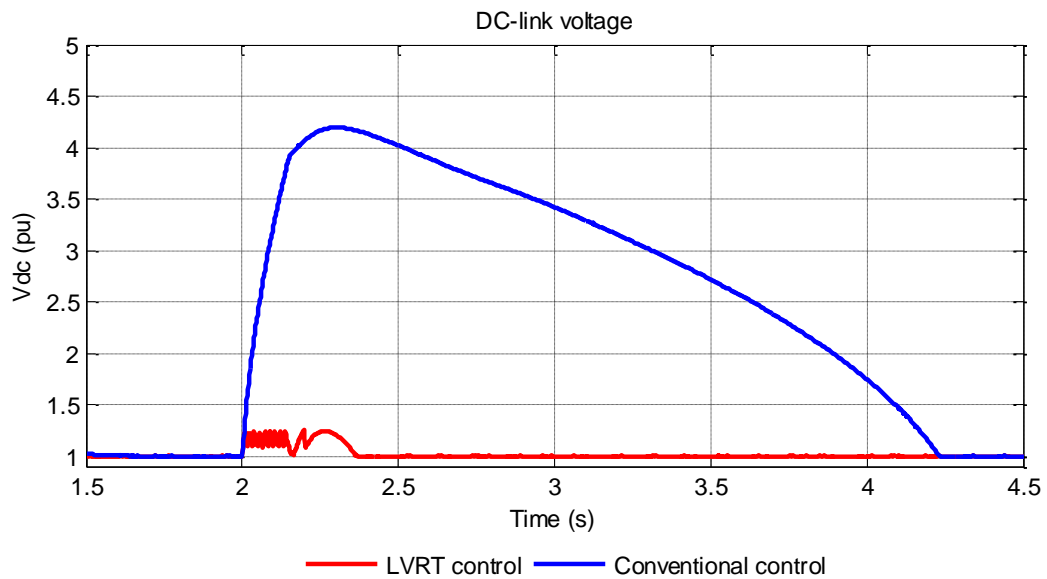


Figure 5.51: DC-link voltage during grid fault for case 6

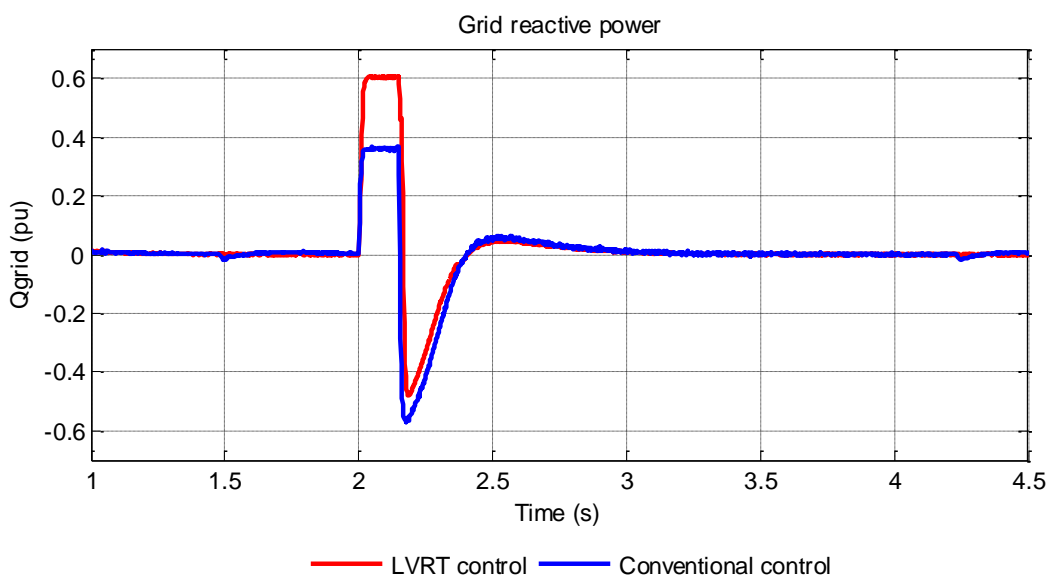


Figure 5.52: Grid reactive power output during grid fault for case 6

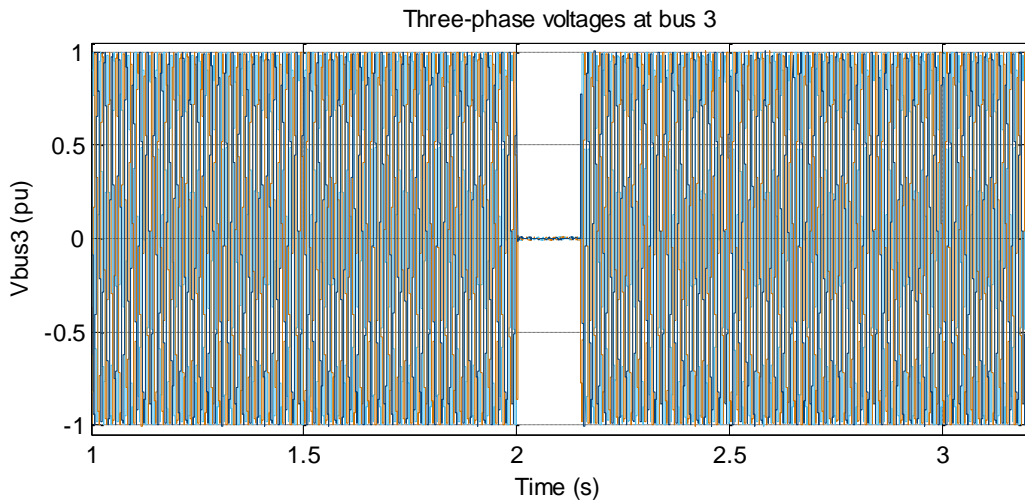


Figure 5.53: Voltage profile during fault at bus 3 for case 7

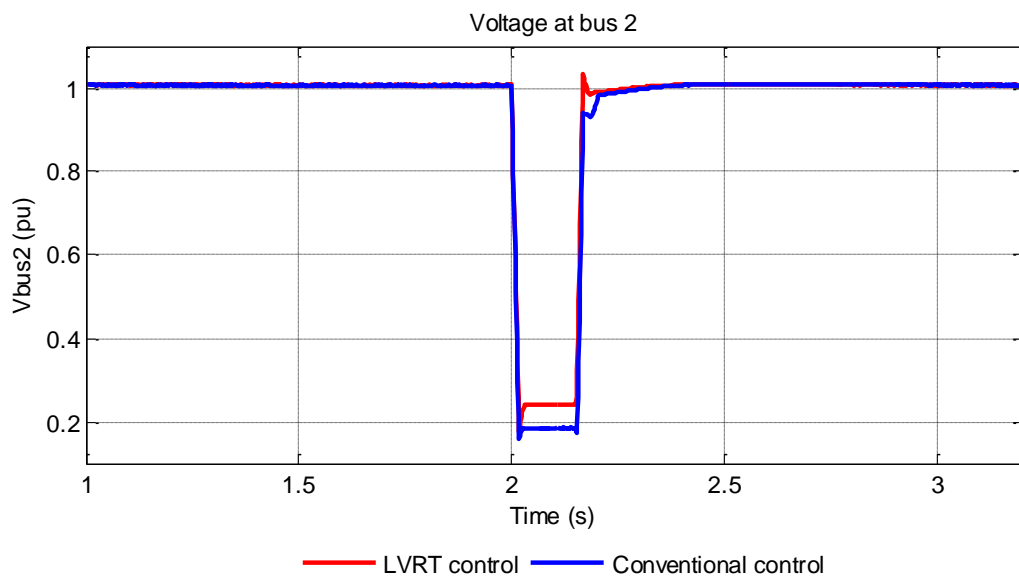


Figure 5.54: Voltage profile at PCC during grid fault for case 7

5.4.2.7 Case 7: 100% three-phase voltage dip at bus 3, fault duration 150 ms, at wind speed 7 m/s

In this case, on the contrary to case 6, the LVRT capability of the wind turbine system is tested with a grid fault occurring at low wind speed, here 7 m/s. The voltage profile at bus 3 showing the magnitude of the three phases is presented in Figure 5.53. As is in the previous case, the magnitudes of the voltages drop to values close to 0 p.u during the fault. The PCC voltage profiles for both the conventional and LVRT controls are also like in the previous case. The PCC voltage in this case however restores pre-fault value after fault clearance faster than in case 6. The grid active power is shown in Figure 5.55. the power supplied by the wind farm is equal to 0.25 p.u of the rated power. During the fault this value drops to 0.08

p.u and 0.22 p.u using the conventional control and the LVRT control respectively, as in case 6. However, the overshoots after fault dismissal reach 1 p.u and last 50 ms on normal mode against 0.84 p.u and 25 ms on LVRT control. For the DC-link voltage, its value reaches around 1.76 p.u during fault under conventional control, then drops back to nominal value almost immediately after the fault is cleared. The discharge time is almost inexistent in this case since only 0.25 p.u active power is transferred to the grid at 7 m/s. Reactive power contribution is the same as for case 6, however the negative peaks after fault removal are reduced due to the short DC-link recovery time.

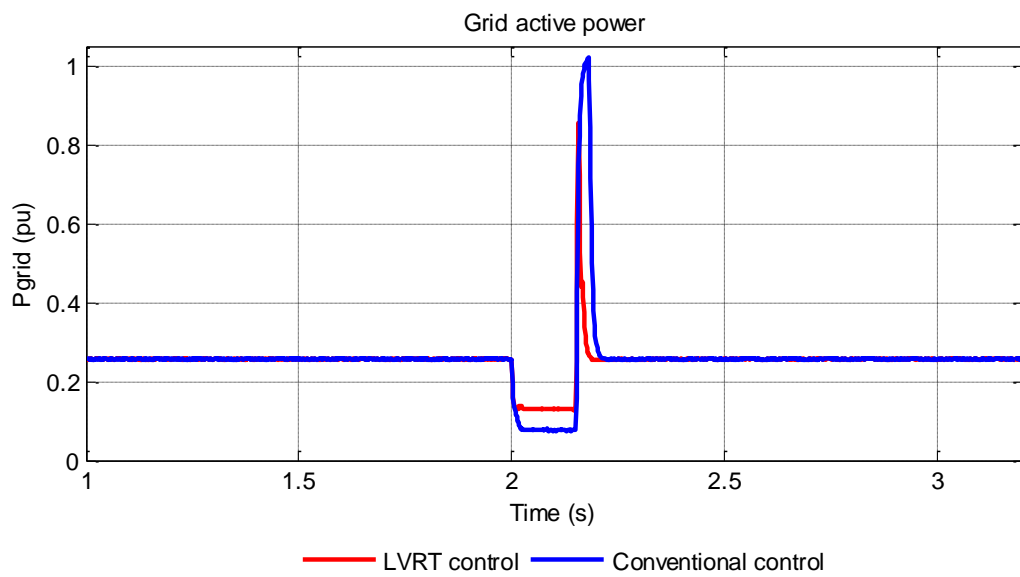


Figure 5.55: Grid active power output during grid fault for case 7

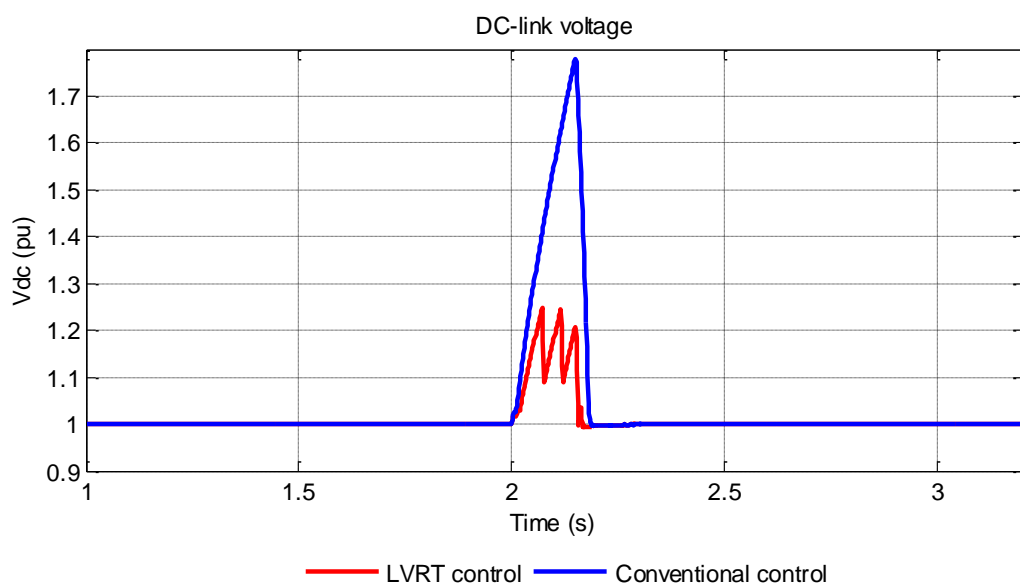


Figure 5.56: DC-link voltage during grid fault for case 7

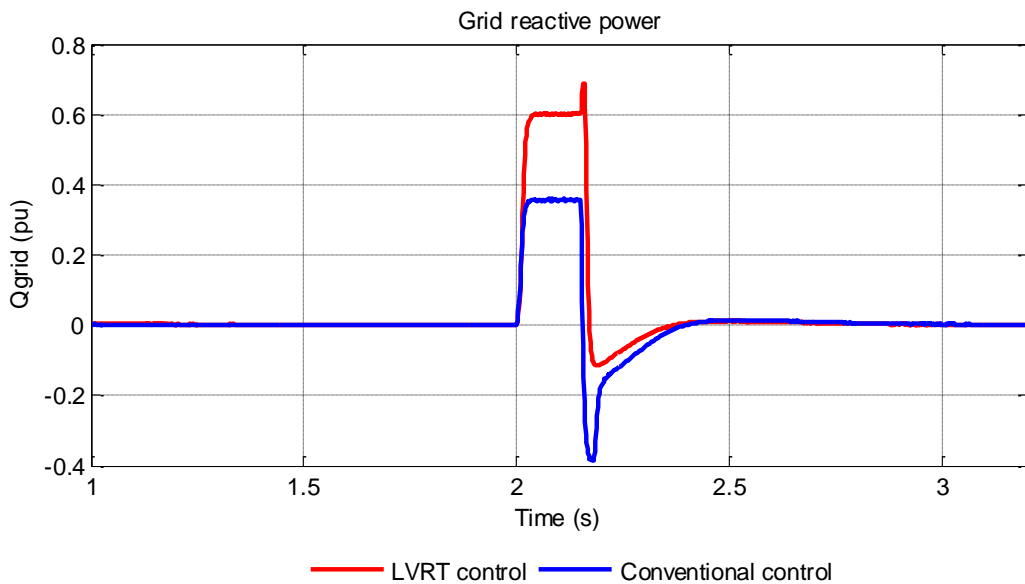


Figure 5.57: Grid reactive power output during grid fault for case 7

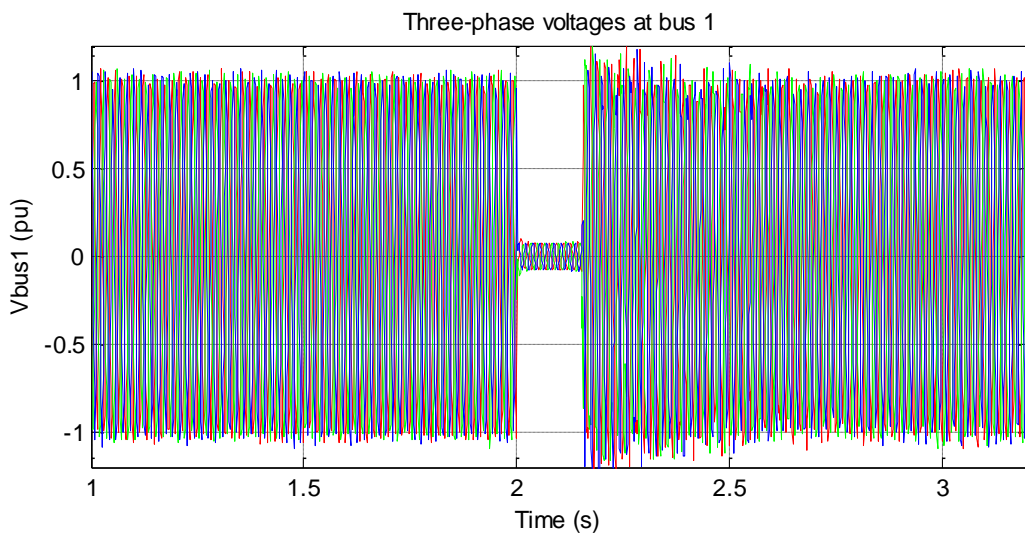


Figure 5.58: Voltage profile during fault at bus 1 for case 8

5.4.2.8 Case 8: Full power, 100% three-phase voltage dip at bus 1, fault duration 150 ms

For this case scenario, a three-phase fault is applied at the wind farm terminals (bus 1) for a duration of 150 ms, at rated wind speed. This case is similar to case 1, except that here the fault is located on bus 1. The voltage profile at bus 1 shows that the voltage does not completely drop to zero as in the previous case, as illustrated in Figure 5.58. The PCC voltage only dips down to about 0.41 p.u and recovers quite smoothly for both controls as depicted in Figure 5.59. The active power to the grid drops down to about 0.04 p.u under conventional control which is the lowest compared to all previous cases, certainly because of the fault proximity (bus 1 in this case and bus 3 in other cases). Without LVRT

compensation, the DC-link voltage peaks at 3.7 p.u with a discharge time of about 0.6 s, while the voltage is satisfactorily regulated with LVRT control. The active power and the DC-link voltage are presented in Figure 5.60 and Figure 5.61 respectively. Finally, in Figure 5.62, the reactive power is negative during the fault meaning that in this case, reactive power is rather absorbed from the grid.

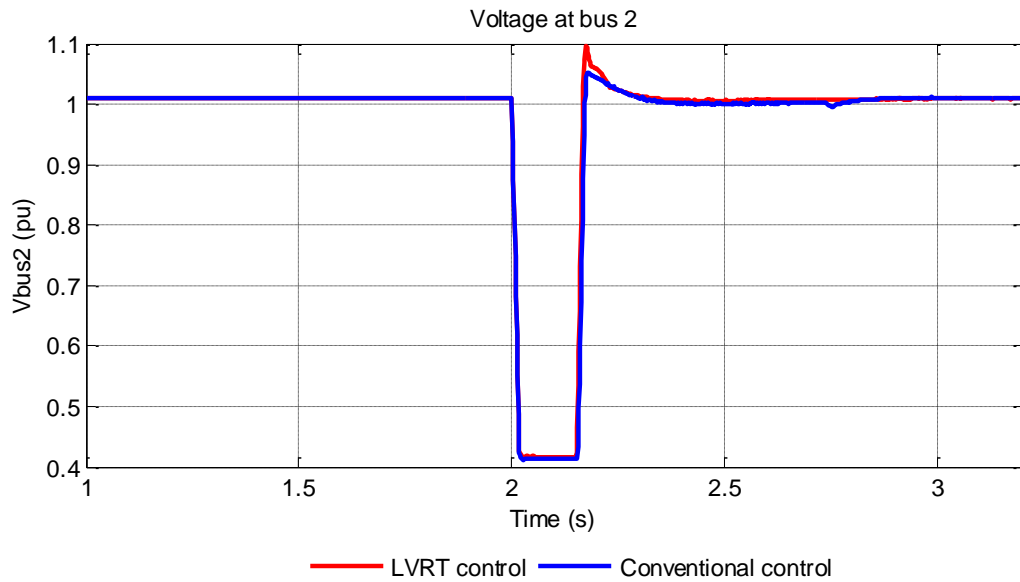


Figure 5.59: Voltage profile at PCC during grid fault for case 8

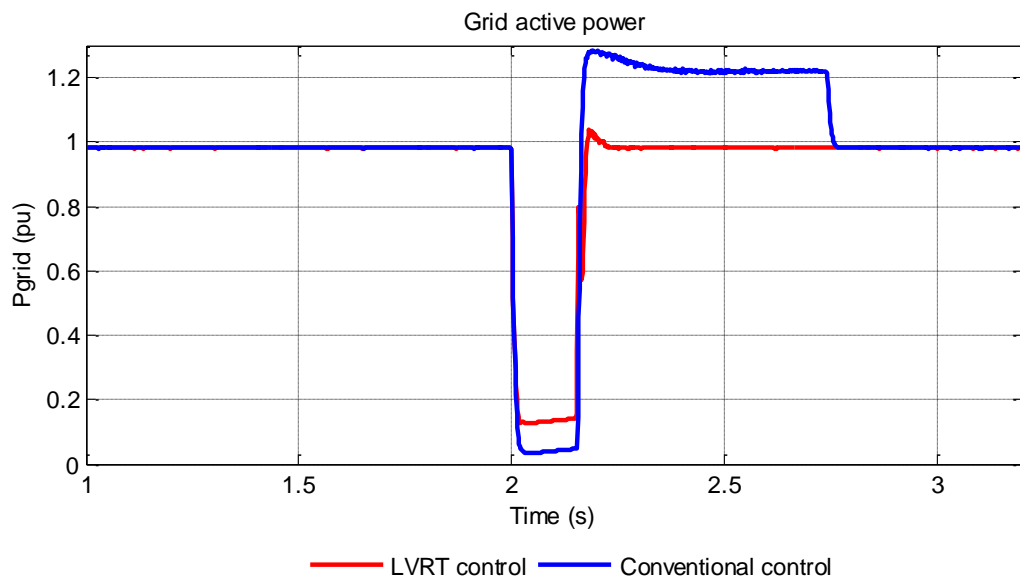


Figure 5.60: Grid active power output during grid fault for case 8

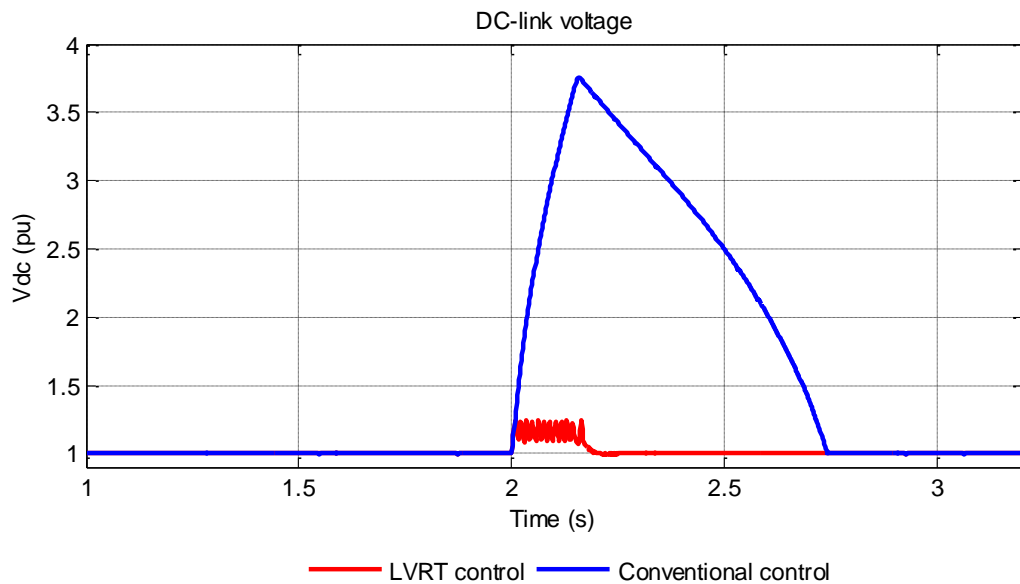


Figure 5.61: DC-link voltage during grid fault for case 8

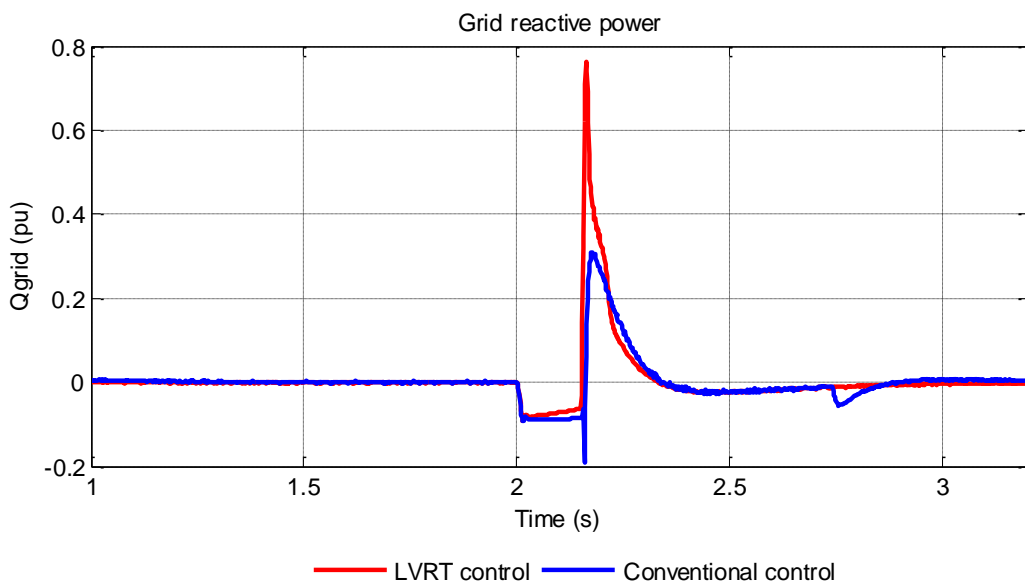


Figure 5.62: Grid reactive power output during grid fault for case 8

Summary of the chapter

This chapter presented and discussed the simulation results of a grid connected PMSG wind energy conversion system. The wind farm model aggregation techniques were used to convert an individual 1.5 MW wind turbine into the 9 MW wind farm used in the simulations studies. The electric power system used is a test platform developed on the MATLAB Sympowersystems simulation tool. The WECS's performance was first tested under normal operating conditions. A varying wind speed profile was applied to the turbine system and generator and grid side converter parameters were analyzed. The WPP was then tested under grid fault conditions, where different case scenarios were implemented with regards

to the fault type, the fault depth, the fault duration and the fault position. The results were compared on the basis that faults compensation methods were employed in addition to the conventional controller or not during grid different faults.

CHAPTER SIX

CONCLUSIONS AND RECOMMENDATIONS

This thesis investigated the capability of a wind energy conversion system in remaining connected to the electrical network during grid disturbances, in this case voltage drop, as per specified by the grid code FRT requirement presented in section 3.8 of this document. The installation of large capacity wind power plants as an attempt to reduce the global carbon emissions has emphasized the urge for system operators to ensure that wind farms connected to the transmission and distribution networks comply with certain requirements, for smooth, safe and reliable grid operation. In fact, a loss in generation capacity due to a large scale WPP disconnection as a result of a grid voltage sag may lead to a succession of production losses which could further cause a partial or sometimes complete power system shutdown. This situation is clearly undesirable and therefore should be absolutely avoided.

In this study, a grid connected PMSG WECS was tested with regards to its ability to ride through a low voltage inception at grid level. Different case scenarios were investigated.

From the simulation results it can be concluded that:

- The system shows great stability under varying wind speed conditions. MPPT is successfully achieved through OTC on the generator side, while DC-link regulation and unity power factor operation objectives are met on the grid side.
- The braking chopper circuit manages to keep the DC-link voltage at an acceptable level during different grid sag conditions, ensuring the safety of the power converters.
- The braking chopper only regulates the DC-link voltage and does not improve the PCC voltage drop during the fault. However, there is a faster and smoother recovery to pre-fault value after fault dismissal.
- Reactive current injection can considerably reduce the power through the DC-link by increasing the voltage at the connection point during a grid fault. In most cases, this is not sufficient in keeping the DC-link voltage below the maximum allowable limit. The braking chopper therefore overtakes the protection duty.
- The grid side converter successfully supplies reactive current to support the grid voltage during fault, according to the reactive power support requirement described in figure 3.9 of section 3.1.5.
- When the fault occurs at the wind farm's terminals, reactive power is rather absorbed from the grid and the PCC voltage is not supported.

The following suggestions are proposed for future investigations:

- The study could also be conducted on a larger scale using an IEEE 14-bus test system or even a portion of the South African network as test benchmark and other grid code requirements could be investigated.
- An experimental approach of the study could be implemented through real time simulations and laboratory scale work.
- Interaction between individual wind turbines in a WPP using a detailed wind farm model in the case of internal abnormalities.
- Reactive power supervisory control of grid connected renewable energy systems during grid faults.

REFERENCES

- Abdullah, M. A., Yatim, A. H. M., Tan, C. W. & Saidur, R., 2012. A review of maximum power point algorithms for wind energy systems. *Renewable and Sustainable Energy Reviews*, Volume 16, pp. 3220-3227.
- Ackermann, T., 2005. *Wind Power in Power Systems*. Chichester: Wiley.
- Ali, M. H., 2012. *Wind Energy Systems: Solutions for Power Quality and Stabilization*. 2nd ed. Nidwalden: CRC Press.
- Allagui, M., Hasnaoui, O. & Belhadj, J., 2014. A 2MW direct drive wind turbine; vector control and direct torque control techniques comparison. *Journal of Energy in Southern Africa*, 25(2), pp. 117-126.
- Anaya-Lara, O. et al., 2009. *Wind energy generation: modelling and control*. Chichester: Wiley.
- Bang, D., Polinder, H., Shrestha, G. & Ferreira, J. A., 2008. *Review of generator systems for direct-drive wind turbines*. Delft, European Wind Energy Conference.
- Baroudi, J. A., Dinavahi, V. & Knight, A. M., 2005. *A Review of Power Converter Topologies for Wind Generators*. San Antonio, IEEE, pp. 458-465.
- Basrur, R. & Koh, S. L. C., 2012. *Nuclear Power and Energy Security in Asia*. New York: Routledge.
- Ben Smida, M. & Sakly, A., 2015. Pitch angle control for variable speed wind turbines. *Journal of Renewable Energy and Sustainable Development (RESO)*, pp. 81-88.
- Bisoyi, S. K., Jarial, R. K. & Gupta, R. A., 2013. A Review of the State of the Art of Generators and Power Electronics Converter Topologies for Wind Energy Conversion System. *International Journal of Emerging Technology and Advanced Engineering*, 3(3), pp. 283-291.
- Blaabjerg, F., Iov, F., Chen, Z. & Ma, K., 2009. *Power Electronics and Control for Wind Turbine Systems*. Lincoln, IEEE, pp. 1-16.
- Breeze, P., 2005. *Power Generation Technologies*. Manchester: Newnes.
- Bunjongjit, K. & Kumsuwan, Y., 2013. Performance enhancement of PMSG systems with control of generator-side converter using d-axis stator current controller. *ECTI Transactions on Electrical Engineering, Electronics and Communications*, 11(2), pp. 51-57.
- Busca, C., Stan, A.-I., Stanciu, T. & Stroe, D. I., 2010. *Control of Permanent Magnet Synchronous Generator for large wind turbines*. Bari, IEEE, pp. 3871 - 3876.
- Camm, E. H. et al., 2009. *Characteristics of Wind Turbine Generators for Wind Power Plants*. Calgary, IEEE, pp. 1-5.
- Cao, W., Xie, Y. & Tan, Z., 2012. Wind Turbine Generator Technologies. *Intech*, pp. 177-204.
- Chen, Z., Guerrero, J. M. & Blaabjerg, F., 2009. A Review of the State of the Art of Power electronics for Wind Turbines. *IEEE Transactions on Power Electronics*, 24(8), pp. 1859-1875.

- Chowdhury, M. M. et al., 2012. *Enhanced control of a direct drive grid connected wind energy system with STATCOM*. Bali, IEEE, pp. 1-6.
- Conroy, J. F. & Watson, R., 2007. Low-voltage ride-through of a full converter wind turbine with permanent magnet generator. *Renewable Power Generation, IET*, 1(3), pp. 182-189.
- Craddock, D., 2008. *Renewable energy made easy: free energy from solar, wind, hydropower, and other alternative energy sources*. Ocala: Atlantic Publishing Group, Inc.
- de Alegria, I. M. et al., 2007. Connection requirements for wind farms: A survey on technical requirements and regulations. *Renewable and Sustainable Energies Reviews*, Issue 11, pp. 1858-1872.
- de Freitas, T. R. S., Menegaz, P. J. M. & Simonetti, D. S. L., 2011. *Converter Topologies for Permanent Magnetic Synchronous Generator on Wind Energy Conversion System*. Praiamar, IEEE, pp. 936-942.
- Debnath, S. & Saeedifard, M., 2013. A New hybrid modular multilevel converter for grid connection of large wind turbines. *IEEE Transactions on Sustainable Energy*, 4(4), pp. 1051-1064.
- Dong, S., Li, H. & Wang, Y., 2012. *Low voltage ride through capability enhancement of PMSG-based wind turbine*. Hangzhou, IET, pp. 1-5.
- Earnest, J., 2015. *Wind power technology*. 2nd ed. Delhi: PHI.
- Earnest, J. & Wizelius, T., 2011. *Wind power plants and project development*. New Delhi: PHI Learning Private Limited.
- Florescu, A. et al., 2010. *Advantages, limitations and disadvantages of z-source inverter*. Sinaia, IEEE, pp. 483-486.
- Freire, N. M. A., 2013. *Fault-tolerant permanent magnet synchronous generator drives for wind turbine applications*, Coimbra: s.n.
- Greencape, 2015. *Renewable energy, green cape intelligence report 2015*, s.l.: s.n.
- Gupta, A., Jain, D. K. & Dahiya, S., 2012. *Some Investigations on Recent Advances in Wind Energy Conversion Systems*. Coimbatore, IACSIT Press, pp. 47-52.
- GWEC, 2015. *Global wind report: annual market update 2014*. [Online] Available at: <https://gwec.net/publications/global-wind-report-2/global-wind-report-2014-annual-market-update/> [Accessed 27 April 2015].
- Hansen, A. D. & Michalke, G., 2007. Fault ride-through capability of DFIG wind turbines. *Renewable Energy*, 32(9), pp. 1594-1610.
- Hansen, A. D. & Michalke, G., 2009. Multi-pole permanent magnet synchronous generator wind turbines grid support capability in uninterrupted operation during grid faults. *IET Renewable Power Generation*, 3(3), pp. 333-348.
- Hansen, M. O. L., 2008. *Aerodynamics of wind turbines*. 2nd ed. London: Earthscan.
- Hau, E., 2013. *Wind Turbines: Fundamentals, Technologies, Applications, Economics*. 3rd ed. Berlin: Springer-Verlag.

- Heir, S., 2014. *Grid integration of wind energy conversion systems*. 3rd edition ed. Chichester: John Wiley & Sons.
- Heng, N., Jiao, L., Peng, Z. & Yikang, H., 2008. *Improved control strategy of an active crowbar for directly-driven PM wind generation system under grid voltage dips*. Wuhan, IEEE, pp. 2294-2298.
- Heydari, M. & Smedley, K., 2015. *Comparison of maximum power point tracking methods for medium to high power wind energy systems*. Zahedan, IEEE.
- Huang, N., 2013. *Simulation of power control of wind turbine permanent magnet synchronous generator system*, Milwaukee: epublications.
- Hu, J. et al., 2010. *A novel control strategy for Doubly Fed Induction Generator and Permanent Magnet Synchronous Generator during voltage dips*. Christchurch, IEEE, pp. 1-6.
- Ibrahim, R. A., Hamad, M. S., Dessouky, Y. G. & Williams, B. W., 2012. *A review on recent low voltage ride-through solutions for PMSG wind turbines*. Sorrento, IEEE, pp. 265-270.
- IEA, 2012. *World Energy Outlook 2012*. [Online]
Available at: http://www.iea.org/publications/freepublications/publication/WEO2012_free.pdf
[Accessed 30 April 2014].
- Jamil, M., Gupta, R. & Singh, M., 2012. *A review of power converter topology used with PMSG based wind power generation*. Murthal, IEEE, pp. 1-6.
- Jash, K., Saha, P. K. & Panda, G. K., 2013. Vector control of permanent magnet synchronous motor based on sinusoidal pulse width modulated inverter with proportional integral controller. *Journal of Engineering Research and Applications*, 3(5), pp. 913-917.
- Kasem Alaboudy, A. H., Daoud, A. A., Desouky, S. S. & Salem, A. A., 2013. Converter controls and flicker study of PMSG-based grid connected wind turbines. *Ain Shams Engineering Journal*, Volume 4, pp. 75-91.
- Kesraoui, M., Bencherouda, O. & Mesbahi, Z., 2010. *Power control of PMSG based wind turbine system above rated wind speed*. Sousse, IREC, pp. 133-140.
- Khater, F. & Omar, A., 2013. A Review of Direct Driven PMSG for Wind Energy Systems. *Journal of Energy and Power Engineering*, Volume 7, pp. 1592-1603.
- Kilk, A., 2007. Low-speed permanent-magnet synchronous generator for small-scale wind power applications. *Oilshale*, 24(2), pp. 318-331.
- Kim, H. S. & Lu, D. D.-C., 2010. *Review on wind turbine generators and power electronic converters with the grid-connection issues*. Christchurch, IEEE, pp. 1-6.
- Koc, E., 2010. *Modelling and Investigation of Fault Ride Through Capability of Variable Speed Wind Turbines*, Ankara: Middle East Technical University.
- Kundur, P. S., 1994. *Power system stability and control*. New York: McGraw-Hill Professional.
- Leao, R. P. S. et al., 2010. *The Implementation of the Low Voltage Ride-Through Curve on the Protection System of a Wind Power Plant*. Las Palmas de Gran Canaria, European Association for the Development of Renewable Energies, Environment and Power Quality.
- Li, H. & Chen, Z., 2008. Overview of Different Wind Generator Systems and their Comparisons. *IET Renewable Power Generation*, 2(2), pp. 123-138.

- Madani, N., 2011. *Design of a permanent magnet synchronous generator for vertical axis wind turbine*, Stockholm: Royal Institute of Technology.
- Manwell, J., MCGowan, J. & Rogers, A., 2009. *Wind energy explained: theory, design and application*. 2nd ed. Chichester: Wiley.
- Marrone, C. A. Q., 2014. *Challenges for the integration of wind park clusters into power grids: Approach and methodology for the integration and dispatch of wind park clusters into the power grids*, s.l.: BoD.
- Mchunu, T. & Khoza, T., 2013. *Grid connection code for renewable power plants South Africa*. East London, AMEU.
- Melicio, R., Mendes, V. M. F. & Catalao, J. P. S., 2010. Modeling, control and simulation of full-power converter wind turbines equipped with permanent magnet synchronous generator. *International Review of Electrical Engineering*, 5(2), pp. 397-408.
- Mittal, R., Sandhu, K. & Jain, D., 2010. An Overview of Some Important Issues Related to Wind Energy Conversion System (WECS). *International Journal of Environmental Science and Development*, 1(4), pp. 351-363.
- Mittal, R., Sandhu, K. S. & Jain, D. K., 2009. Low Voltage Ride-Through (LVRT) of Grid Interfaced Wind Driven PMSG. *ARPN Journal of Engineering and Applied Sciences*, 4(5), pp. 73-83.
- Mohseni, M. & Islam, S. M., 2011. *Comparing technical connection requirements for large wind power plants*. San Diego, IEEE, pp. 1-8.
- Mohseni, M. & Islam, S. M., 2012. Review of international grid codes for wind power integration: Diversity, technology and a case for global standard. *Renewable and Sustainable Energies Reviews*, Issue 16, pp. 3876-3890.
- Munteanu, I., Bratcu, A. I., Cutululis, N.-A. & Ceanga, E., 2008. *Optimal control of wind energy systems: Towards a global approach*. London: Springer-Verlag.
- Nasiri, M., Milimonfared, J. & Fathi, S. H., 2015. A review of low-voltage ride-through methods for permanent magnet synchronous generator based wind turbines. *Renewable and Sustainable Energy Reviews*, Volume 47, pp. 399-415.
- Nguyen, T. H. & Lee, D.-C., 2010. Ride-through technique for PMSG wind turbines using energy storage systems. *Journal of Power Electronics*, 10(6), pp. 733-738.
- Nguyen, T. H. & Lee, D.-C., 2013. Advanced Fault Ride-Through Technique for PMSG Wind Turbine Systems Using Line-Side Converter as STATCOM. *IEEE Transactions on Industrial Electronics*, 60(7), pp. 2842 - 2850.
- Pandu Ranga, R. G. & Vijaya, K. M., 2013. *Implementation of matrix converter based PMSG for wind energy conversion system*. Coimbatore, IEEE, pp. 115-120.
- Patel, M. R., 2006. *Wind and solar power systems: design, analysis, and operation*. 2nd ed. Nidwalden: CRC Press.
- Peng, F. Z., 2002. *Z-source inverter*. Pittsburgh, IEEE, pp. 775-781.
- Perelmuter, V. M., 2013. *Electrotechnical Systems: simulation with simulink and simpowersystems*. Boca Raton: CRC Press.

- Polinder, H., Bang, D.-J., Li, H. & Chen, Z., 2007. *Concept Report on Generator Topologies, Mechanical & Electromagnetic Optimization*, s.l.: s.n.
- Prerna, B. & Jagdeesh Kumar, P. S., 2013. Study of Power Converter Topology used for Renewable Energy Resources using Wind. *International Journal of Emerging Research in Management & Technology*, 2(12), pp. 2278-9359.
- Qiao, W., Harley, R. G. & Venayagamoorthy, G. K., 2007. *Dynamic Modeling of Wind Farms with Fixed-Speed Wind Turbine Generators*. Tampa, IEEE.
- Qiu, Z., Zhou, K. & Li, Y., 2011. *Modeling and control of diode rectifier fed PMSG based wind turbine*. Weihai, IEEE, pp. 1384-1388.
- Quang, N. P. & Dittrich, J. A., 2008. *Vector control of three-phase AC machines*. Berlin: Springer.
- Raphael, S. & Massoud, A., 2011. *Unified power flow controller for low voltage ride through capability of wind-based renewable energy grid-connected systems*. Sousse, IEEE, pp. 1-6.
- Rekioua, D., 2014. *Wind power electric systems: modeling, simulation and control*. New York: Springer.
- Ren21, 2015. *Renewables 2015: global status report*. [Online] Available at: https://www.ren21.net/wp-content/uploads/2019/05/GSR2015_Full-Report_English.pdf [Accessed 27 April 2015].
- Rolan, A. et al., 2009. *Modeling of a variable speed wind turbine with a permanent magnet synchronous generator*. Seoul, IEEE, pp. 734-739.
- Rosyadi, M., Muyeen, S. M., Takahashi, R. & Tamura, J., 2011. *Low voltage ride-through capability improvement of wind farms using variable speed permanent magnet wind generator*. Beijing, IEEE, pp. 1-6.
- Sanchez, A. G., Molina, M. G. & Rizzato Ledesma, A. M., 2012. Dynamic model of wind energy conversion systems with PMSG-based variable-speed wind turbines for power system studies. *International journal of Hydrogen Energy*, Volume 37, pp. 10064-10069.
- Shuju, H., Jianlin, L. & Honghua, X., 2008. *Modeling on converter of direct-driven WECS and its characteristics during voltage sags*. Chengdu, IEEE, pp. 1-5.
- Soriano, L. A., Yu, W. & Rubio, J. d. J., 2013. Modeling and control of wind turbine. *Mathematical Problems in Engineering*, Volume 2013, pp. 1-13.
- Sourkounis, C. & Tourou, P., 2013. *Grid Code Requirements for Wind Power Integration in Europe*. Limasol, Hindawi Publishing Corporation, pp. 1-9.
- Tong, W., 2010. *Wind power generation and wind turbine design*. Southampton: WIT Press.
- Tsili, M., Patsiouras, C. & Papathanassiou, S., 2009. A review of grid code technical requirements for wind farms. *IET Renewable Power Generation*, 3(3), pp. 308-332.
- Vilathgamuwa, D. M., Wang, X., Tseng, K. J. & Gajanayake, C. J., 2008. *Z-source inverter based grid-interface for variable-speed wind turbine generators*. Rhodes, IEEE, pp. 4545-4550.
- Vittal, V. & Ayyanar, R., 2013. *Grid integration and dynamic impact of wind energy*. New York: Springer.

- Wagner, H.-J. & Mathur, J., 2009. *Introduction to wind energy systems: basics, technology and operation*. Berlin: Springer.
- Wenming, G., Yun, W., Shuju, H. & Honghua, X., 2011. *A survey on recent low voltage ride-through solutions of large scale wind farm*. Wuhan, IEEE, pp. 1-5.
- Wenske, J., 2011. *Wind Energy Report Germany 2011 Special Report: Direct Drives and drive-train development trends*, s.l.: Siemens Press Picture.
- Writer, S., 2015. *BusinessTech*. [Online]
Available at: <http://businesstech.co.za/news/energy/93743/south-africas-biggest-wind-farms-vs-the-world/>
[Accessed 10 December 2015].
- Wu, B., Lang, Y., Zargari, N. & Kouro, S., 2011. *Power conversion and control of wind energy systems*. New Jersey: Wiley.
- Yamarasu, V. et al., 2015. High-power wind energy conversion systems: state-of-the-art and emerging technologies. *Proceedings of the IEEE*, 103(5), pp. 740-788.
- Yang, G. & Li, H., 2009. *Application of a matrix converter for PMSG wind turbine generation system*. Capri, IEEE, pp. 619-623.
- Yang, X.-p., Duan, X.-f., Feng, F. & Tian, L.-l., 2009. *Low voltage ride-through of directly driven wind turbine with permanent magnet synchronous generator*. Wuhan, IEEE, pp. 1-5.
- Yan, L. et al., 2011. *Study on LVRT capability of D-PMSG based wind turbine*. s.l., s.n.
- Zeng, Q. & Chang, L., 2005. *Study of advanced control strategies for three-phase grid-connecter PWM inverters for distributed generation*. Toronto, IEEE, pp. 1311-1316.

APPENDICES

6.1 Appendix A: System parameters

Table A.1: Individual wind turbine parameters (Nasiri, et al., 2015)

Parameters	Values
Rated power	1.5 MW
Air density	1.225 kg/m ³
Blade radius	35.25 m
Maximum power coefficient	0.48
Optimal tip speed ratio	8.1
Rated wind speed	11 m/s
Total moment of inertia	4872000 kg/m ²
Damping coefficient	200 Nms/rad

Table A.2: Generator parameters (Nasiri, et al., 2015)

Parameter	Value
Rated power	1.5 MW
Rated voltage	690 V
Rated flux	7.0172 Wb
Stator resistance	3.17 mΩ
Stator inductance	3.07 mH
Number of pole pairs	40

Table A.3: DC-link parameters (Nasiri, et al., 2015)

Parameter	Value
DC-link voltage	1500 V
DC-link capacitance	0.023 F
Switching frequency	5000 Hz

6.2 Appendix B: System simulation model

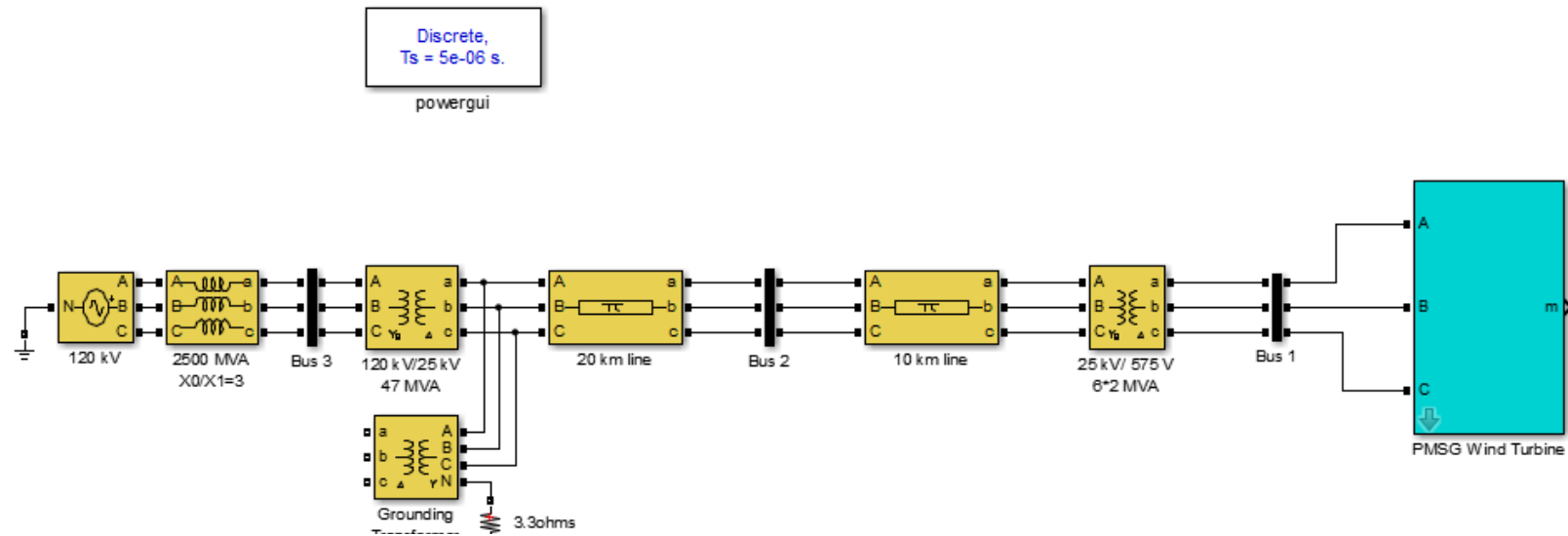


Figure B.6.1: Electric power system model

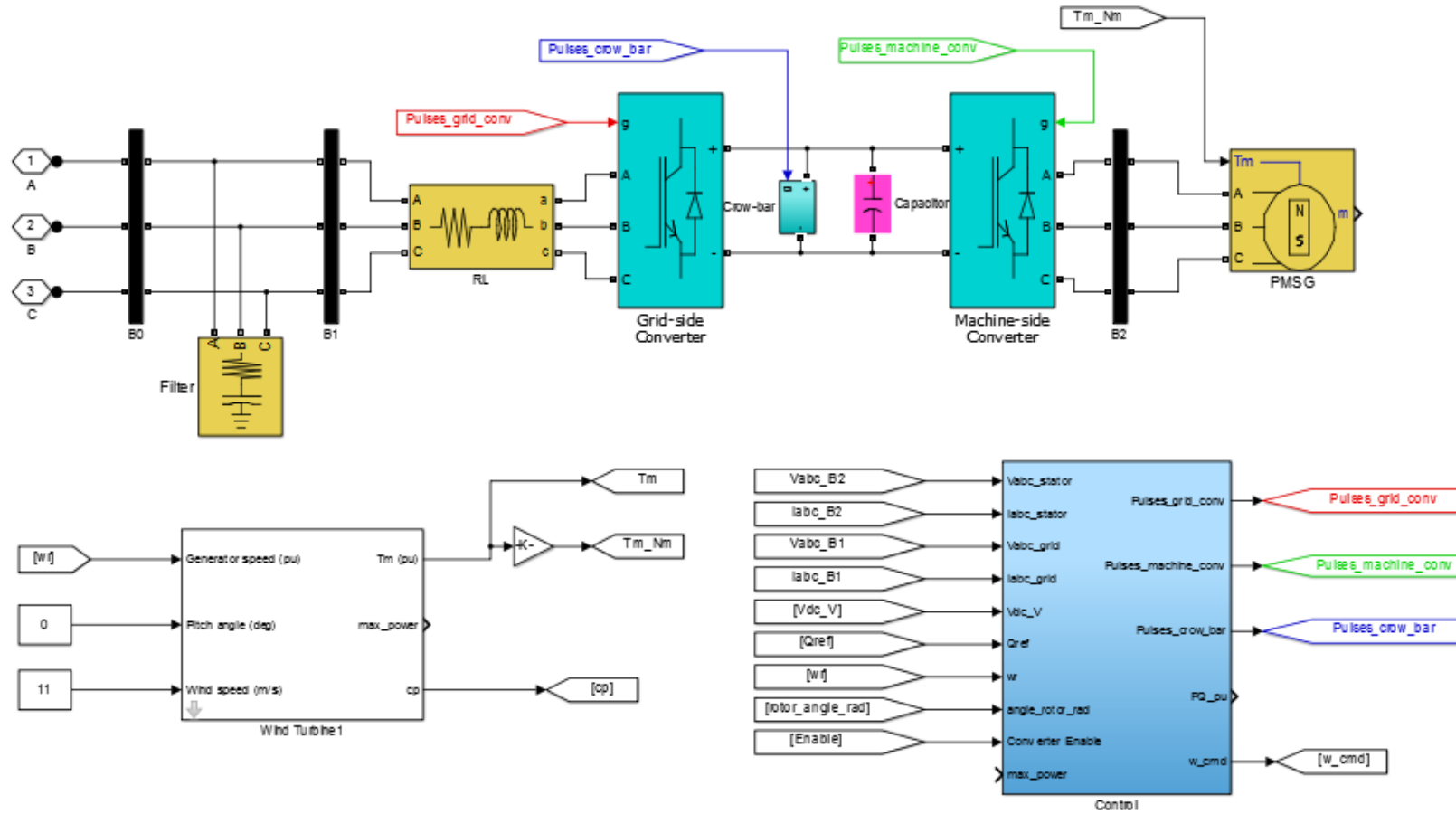


Figure B.6.2: Complete model of the PMSG wind energy conversion system

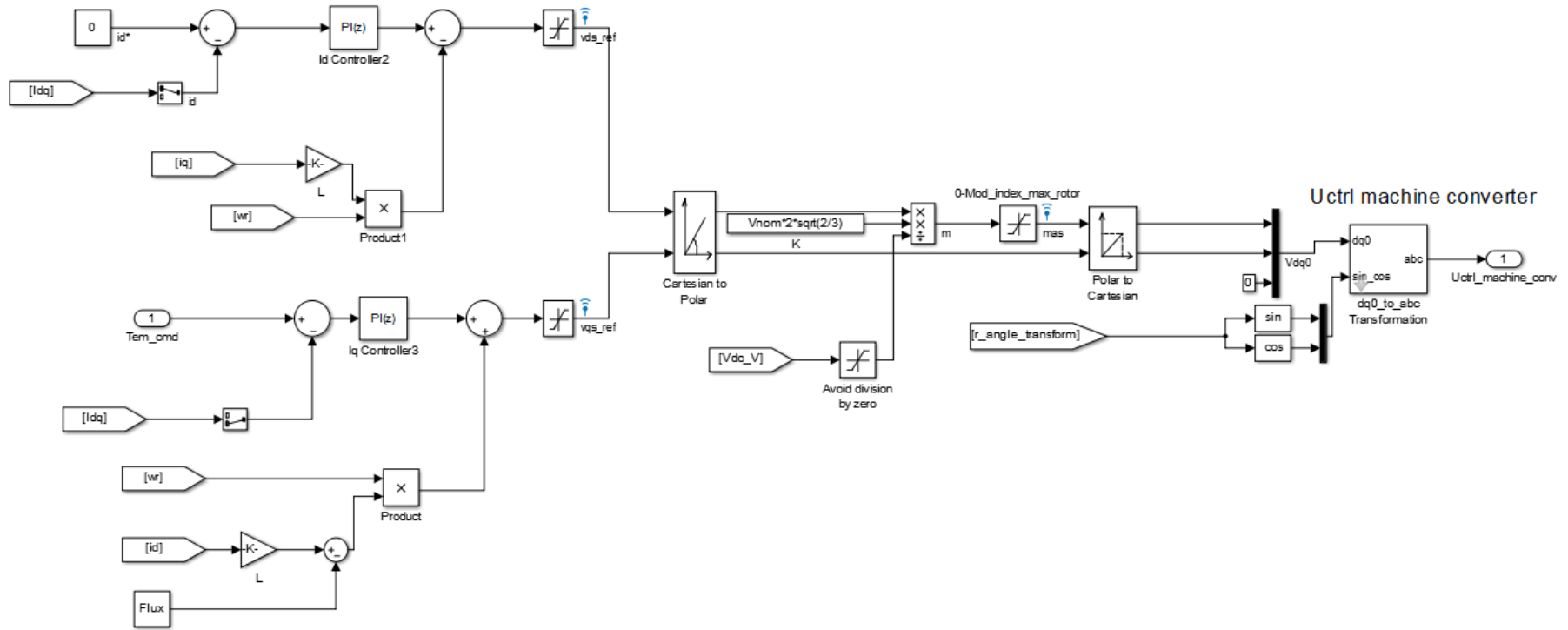


Figure B.6.3: Simulation model of the generator side converter

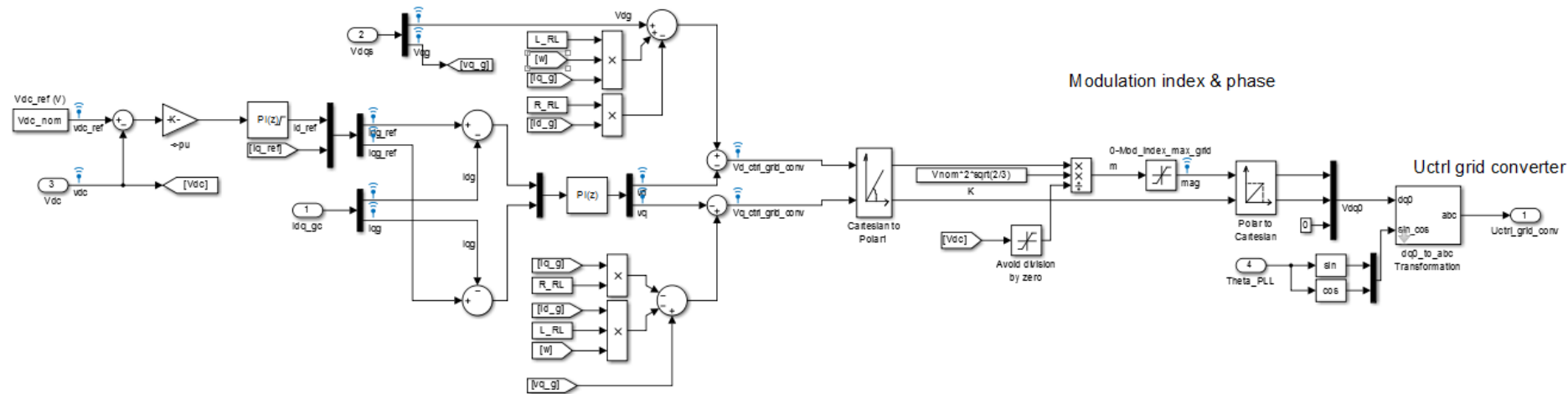


Figure B.6.4: Simulation model of the grid side converter